

CHAPTER 1

ANTENNA STRUCTURE FUNDAMENTALS

Much of the world around us is affected by wave phenomena, which are often characterized by frequency (number of waves per unit of time) and wave length. Frequency and wave length are related by the speed with which waves propagate through the various media. For example, the speed of electromagnetic wave propagation in free space is about 1.182×10^{10} inches per second. Therefore the wave length for the frequency of 1×10^9 cycles per second (1 GHz) is $1.182 \times 10^{10} / 1 \times 10^9$ or 11.8 inches (in metric units, the speed is about 3×10^{11} mm per second, so that the wavelength at 1 GHz is about 300 mm). The rule is that electromagnetic wavelengths are about 11.8 inches (300 mm) per GHz .

The frequencies relevant to large-diameter antennas are in the microwave band of from 2 to 100 GHz, thus the wavelengths are from about 6 inches to 1/8 of an inch (150 mm to 3 mm). Microwave frequencies are higher than radio and television frequencies and are lower than the infrared, optical, and gamma ray frequencies at the progressively higher electromagnetic bands. The microwave antennas that are considered here have diameters of from as small as 10 meters to as large as 100 meters, and are used for a multitude of communications and radio astronomy applications from ground and space communications to deep space exploration.

Microwave antennas require surface reflection accuracies of from one-twelfth to one-fiftieth of a wavelength. This means that the ratio of accuracy to structure size for microwave antennas greatly exceeds that of customary civil-engineered buildings or bridges. Although design and analysis of these antennas is a formidable engineering challenge, precise techniques are available for designing and analyzing antenna structures on both component and system levels.

This chapter provides an overview of the physical antenna system. Antenna structures for microwave energy transmission and collection have evolved from primitive pre-World War II era configurations to high-performance antennas of today. This evolution has led from polar mount hour-angle and declination (HA-dec) configurations to the more modern azimuth-elevation (az-el) antennas. The relatively newer beam-waveguide antennas use a modified az-el antenna optical system. Another variation is an offset "clear-aperture" antenna. Offset antennas avoid a blocking "shadow effect" of subreflector and subreflector supports, but their construction is more complex. Therefore, non-offset, symmetrical antennas predominate. Dual-reflector systems, either offset or symmetrical, have subreflectors in

addition to main reflectors, and feedhorns that transmit or receive energy to or from the subreflector. An advantage of dual-reflector systems is an associated magnification factor that effectively amplifies the physical focal length. "Cassegrain" and "Gregorian" systems are the two arrangements that use dual reflectors. Both of these exploit specific useful properties of conic section curves.

1.1 BACKGROUND "

Heinrich Hertz discovered radio waves in 1888. Six years later, the field of radio astronomy originated with Oliver Lodge's speculation of the existence of radiation from the sun (Ref. 1.1). In 1932, Karl Jansky first detected electromagnetic radio waves of extraterrestrial origin (Ref. 1.2). Jansky's antenna was an array of aerials arranged on a rotating wooden platform about 30 meters long. In 1937, Grote Reber was motivated by Jansky's work to build a single-axis rotatable 30-foot-diameter parabolic antenna (Ref. 1.3). Reber's backyard antenna was built primarily from wooden 2 x 4s; the reflecting surface was galvanized iron sheet metal. Figure 1-1 is a reconstruction of the antenna that is located at the entrance to the National Radio Astronomy Observatory in Greenbank, West Virginia.

Reber was able to confirm Jansky's detection and also to construct a sky map of the strength of radio emissions (Ref. 1.4). As Sir Bernard Lovell commented, "When one remembers that Reber was a lone hand working in his spare time his achievement stands out as altogether remarkable." Lovell himself was responsible for developing the 250-foot-diameter steerable azimuth and elevation axes antenna at Jodrell Bank in England. This antenna, shown in Figure 1-2, was completed in 1957 under the sponsorship of the University of Manchester. The structural configuration has accordingly been called a "Manchester Mount." At that time this design seemed a reasonable way to provide azimuth and elevation axis motions, although it has rarely been adopted in later antennas. The Jodrell Bank antenna secured its place in history when it tracked the Russian Sputnik satellite in 1957, and was the world's largest steerable antenna until the completion of the 100-meter antenna at Effelsburg, Germany, in 1973.

The world's largest antenna is currently the 1000-foot-diameter aperture spherical bowl at Arecibo, Puerto Rico. This antenna was built in the early 1970s and features a fixed reflecting surface with a movable feed which is suspended above the surface by cables to provide microwave beam steering. It is unlikely that antennas as large or larger than those already in service will be built in the future. The now-established trend is to operate arrayed groups of smaller diameter antennas (say,

30 to 34-meter diameters). One exception to this is an innovative 100-meter-diameter antenna that is scheduled for completion in the 1990s at the National Radio Observatory site at Greenbank, West Virginia.

The understanding, technology, and interest in parabolic antennas grew rapidly, and in the decade following the completion of the Jodrell Banks antenna there were 64-meter-diameter antennas at Parks, Australia, and Goldstone, California. Other operating installations included a 300-foot-diameter antenna at Greenbank, West Virginia, a 150-foot-diameter antenna at Wallops Island, Virginia, and several 85-foot- to 90-foot-diameter antennas throughout the world. Although never completed, a 600-foot-diameter steerable antenna was conceptualized and partly designed. Although these ultra-large antennas do not necessarily meet the precision surface accuracy desired for the more recent shorter wavelength missions, many of these antennas have had an operational lifespan of more than 30 years and are continuing to provide useful service.

1.2 CURRENT ANTENNA CONFIGURATIONS

Figure 1-3 shows a 34-meter antenna configuration typical of many operating antennas: an "az-el, Cassegrain, wheel and track." The term "wheel and track" refers to the azimuth bearing. This consists of sets of wheels at the base of the structure that roll on a steel plate track that is supported by a circular concrete foundation ring. "Az-el" denotes an azimuth axis of rotation below an (orthogonal) elevation axis of rotation. The astronomer's "alt-az" mount implies essentially only a substitution of "altitude" for "elevation". The term "Cassegrain" refers to a microwave optical system that contains a subreflector between the antenna surface and the focal point. In contrast, a Gregorian antenna places the subreflector on the far side of the focal point. This entails a disadvantage in requiring a longer structure to support the subreflector in addition to some optical restrictions. Consequently the prevalent microwave antenna system by far is the Cassegrain; thus it receives the most attention in this book.

Cassegrain (and Gregorian) systems use microwave feeds that are located above the reflecting surfaces and are usually held in place by feedcone structures. Both are "dual reflector" systems because of the use of a subreflector in addition to the main reflector. An alternative optical system dispenses with subreflectors and places the feed at the focal point ("focal feed"). The subreflector in the first two cases, and the feed in the third case, is held in place by structural leg assemblies that usually are either tripods (three legs) or quadripods (four legs). Quadripods are the most common.

1.3 GROUND ANTENNA COMPONENTS

Figure 1-4 is a sideview sketch that shows the main components of a 34-meter az-el antenna. This is a dual-reflector system that includes a Cassegrain subreflector in conjunction with a parabolic main reflector. The structure is essentially symmetrical with respect to the plane of the sketch.

103.1 Tippina Structure (refer to Figure 1-4)

The dish surface panels, backup structure, subreflector, feedcone, quadripod, and elevation wheel constitute the tipping structure, which is subject to the tipping motions associated with rotations of the antenna's elevation axis.

Panels. The microwave reflecting surface for the antenna shown in the figure is made up of about 500 high-precision surface panels. These are "parasitic" elements that are designed to support only the local loads of their surfaces and are not intended to participate in the main structural action. The panels are held in place by individual adjustable jacks so that they can be precisely positioned at installation time.

Backup Structure. The backup structure is a three-dimensional trusswork that provides the foundation for the panel jacks and is the key element in supporting the external environmental and internal self-weight loads that act on the system. Analysis and design of this structure will be the subject of most of the attention in subsequent chapters. The backup structure also supports the feedcone and the bases of the quadripod legs

Subreflector. The subreflector is supported from the apex of the quadripod by a positioning mechanism. This mechanism adjusts the location of the subreflector to compensate for the structural deflections of backup structure and subreflector support legs under loading conditions.

Feedcone. The feedcone contains the feed, which is a microwave device that directs the energy towards the subreflector during microwave transmission or collects the energy from the subreflector during reception. The two major additional paths in the microwave system are between the subreflector and main reflector and from the main reflector out to space. The microwave energy paths during transmission or during receive modes are essentially the same and differ only in direction.

Quadripod. The quadripod in the figure is attached directly to the backup structure at the reflector surface. Each leg has a trapezoidal cross-section, with plane trusses (which are seen in the figure) forming the two long sides and solid

plates forming the two shorter sides. The legs are joined at their apex by a 3-dimensional truss structure.

Elevation wheel. The elevation wheel is attached to the backup structure. The wheel establishes the elevation position under command of the elevation drive and control system. The wheel contains gear teeth at its rim that engage with an elevation drive pinion(s). The elevation drive pinion is at the output end of a gear box assembly that is powered by the elevation motor(s). The elevation drive for this antenna is supported at the upper end of a long tangent link. The tangent link is supported at its base by a pivot on the alidade. The interior portion of the elevation wheel in the vicinity of the rim contains the counterweights, which can be of concrete, steel, or lead, depending upon the availability of the space for packaging and the leverage in balancing the weight of the rotating structures with respect to the elevation axis.

1.3.2 Alidade and Azimuth Drive

The alidade supports the elevation bearings and the elevation drive and pinion. Two elevation bearings at opposite ends of an elevation axis and the elevation wheel pinion provide the entire support for the tipping structure.

The alidade shown in Figure 1-4 has a wheel and track azimuth bearing system that provides the rotation about a vertical axis. The alidade corners are supported on wheeled carriage (truck) assemblies that roll upon a precisely aligned steel track. The steel track rests on a massive circular concrete foundation. The azimuth drive consists of one or more assemblies of a motor, brake, gear reducer assembly, and output pinion, all located at one or more carriages. The wheel and track assembly is ordinarily incapable of resisting the lateral environmental forces on the system, thus it is customary to provide a central pintle bearing to stabilize the base of the alidade for lateral forces. The antenna shown here has a pintle bearing on top of a concrete foundation pit. The pit contains a cable wrap-up device to accommodate the motions of the many electrical and microwave cables and conduits during azimuth rotation.

An alternative and frequently employed type of azimuth drive system uses a large-diameter azimuth bearing located at the top of a pedestal. The pedestal, typically constructed of reinforced concrete, is high enough to allow the antenna rim to clear the ground at low elevation attitudes. The alidade for this type of drive is lower than the for the wheel and track arrangement because some of the height requirement is shared by the pedestal. Figure 1-5 shows the arrangement; the antenna is NASA's 70-meter antenna at Goldstone, California. The azimuth

bearing for a moderate sized antenna, say up to 25 meters in diameter, could be a type of "frictionless" steel roller bearing, depending upon maximum sizes that can be manufactured, shipped, and field-assembled. In the case of very large-diameter antennas, such as the 70-meter antenna, a hydrostatic azimuth bearing is employed. The alidade floats on pressurized steel pads over a pool of oil. A separate radial bearing counteracts lateral loads on the tipping structure. The elevation drive here consists of motors and gearboxes that are mounted on an alidade platform. The output pinion of each gearbox engages directly with the elevation wheel gear.

Precise shaft angle transducers, such as encoders, are frequently used to supply elevation and azimuth positioning. Alternative positioning devices that have been used or have been given serious consideration include gyros and various triangulation schemes.

1.4 ALTERNATIVE CONFIGURATIONS

1.4.1 Polar Axis Antennas

The hour-angle and declination (HA-dec) axis antenna is one alternative to the az-el axis antenna. The hour-angle axis is the outermost axis; it is a polar axis that points to the North or South Pole, depending upon the hemisphere. The azimuth or polar wheel is in the plane perpendicular to the polar axis and is thus parallel to the equatorial plane. The declination axis is the inner axis and is carried on the hour-angle wheel. The declination axis is orthogonal to but does not intersect the polar axis. The antenna tipping structure pivots on the declination axis and a second tipping motion that includes the declination wheel is imparted by rotations of the polar axis. In the centered position (at the mid position of the declination wheel), the antenna pointing axis is in a plane parallel to the equatorial plane. Figure 1-6 shows the features of a HA-dec antenna orientation. In this figure Φ is the local latitude, t is the hour angle, and δ is the declination angle (the antenna is shown at zero declination). The position of a celestial object is determined by the rotation t of the hour-angle wheel and the rotation δ of the declination wheel.

To convert from an HA-dec coordinate system to an az-el coordinate system the elevation angle α can be determined from:

$$\sin \alpha = \sin \delta \sin \Phi + \cos \delta \cos \Phi \cos t \quad [1.1]$$

and the azimuth angle A can be determined from

$$\cos A = (\sin \delta \cos \Phi - \cos \delta \sin \Phi \cos t) / \cos \alpha \quad [1.2]$$

These equations can be solved to provide the hour-angle and declination for known latitude and azimuth and elevation angles as follows:

$$\sin \delta = \sin \Phi \sin \alpha + \cos \Phi \cos \alpha \cos A \quad [1.3]$$

and

$$\cos t = (\sin \alpha - \sin \delta \sin \Phi) / (\sin \delta \cos \Phi) \quad [1.4]$$

Figure 1-7 is a photograph of a 34-meter HA-dec antenna. The hour-angle wheel is shown almost face-on in the photograph and the upper extremities of this wheel support the declination axis bearings. The declination wheel occupies the space cut out from the hour-angle wheel in the center and just above the polar axis.

An X-Y antenna is a variation of the HA-dec antenna that is equivalent to a HA-dec antenna for which the polar axis is depressed to the horizontal. The X-Y antenna is sometimes preferable to an az-el system when it becomes important to track an object that passes directly overhead--an operation that is not readily performed by an az-el system. There have been designs where a third, cross-elevation, axis was added to az-el antennas to overcome "zenith pass" difficulties.

In the early antenna days, astronomers preferred HA-dec antenna configurations because they eliminated the need to convert from az-el coordinates to astronomy coordinates. Nevertheless, complexities of the structure associated with the HA-dec arrangement resulted in significant disadvantages. The task of transforming to astronomical coordinates became trivial in the 1960s with advances in computational capabilities.

1.4.2 Beam-Waveguide Antennas

A beam-waveguide antenna is a variation of an az-el Cassegrain antenna optical system in which the feed is at the bottom of the alidade or possibly below ground in a basement. A set of additional secondary mirrors, some flat and some curved, route the microwave energy to the feed. Except for the one mirror closest to the surface, which is required to rotate in elevation with the tipping structure, the secondary mirrors can all be fixed to the alidade. Some of the advantages of the beam-waveguide antenna are the simplicity of servicing the feed because of improved accessibility, the ease of changing feeds for varying microwave purposes, and the advantage of the feed being situated in a protected indoor environment. However, there are some disadvantages, including loss of microwave efficiency because of the additional reflections and the longer path from

subreflector to the feed, and the extra effort and difficulty involved in accurately aligning the added mirrors. The particular microwave functions planned for an antenna ultimately determine the suitability of the beam-waveguide system. A schematic of a beam-waveguide antenna optical arrangement is shown in Figure 1-8.

1.4.3 Offset Antennas

The reflecting surface of a conventional Cassegrain antenna is partly blocked by the subreflector and subreflector support. Reduction of the effective aperture by the blocking shadow can degrade antenna efficiency by from 3 to 8 percent. The offset antenna eliminates this blocking by placing the subreflector and supports just past the edge of the aperture. Figure 1-9 shows the configuration.

A problem with this configuration is that the antenna structure is asymmetrical and therefore not as simple to design and build. Consequently, there are application-dependent tradeoffs between the improvements in microwave efficiency and the penalties from the offset structure. For many years the largest two-axis steerable offset antenna in the United States had only a 10-meter diameter.

1.5 CONIC SECTION GEOMETRY

Antenna surfaces are formed by the rotation of a plane conic section curve about a focal axis--thus the surfaces generated are parabolas, hyperbolas, or ellipses of revolution. Parabolic surfaces are used for main reflectors, and the hyperbolic and elliptical surfaces are used for the subreflectors of dual-reflector Cassegrain and Gregorian systems, respectively. The three basic plane curves are shown on Figure 1-10.

The two-dimensional equations of the three plane curves are represented in a rectangular coordinate system in terms of the focal axis direction z and the lateral direction r . The curves can be represented in a polar coordinate system in terms of the focal radius p and the angle from the focal axis β . The three-dimensional surfaces of revolution can be developed in a Cartesian X,Y,Z coordinate system by treating r as the radius of revolution and then replacing each radius by its projections on the X and Y axes.

The equations of the curves in rectangular and polar coordinates are:

parabola

Focal length = F

$$z = \frac{r^2}{4F} \quad [1.5a]$$

$$\rho = \frac{2F}{1 + \cos \beta} \quad [1.5b]$$

Hyperbola

Semi-transverse axis a, semi-conjugate axis b, focal length $c = (a^2 + b^2)^{1/2}$. The asymptotes pass through the origin of coordinates at the angles with tangents equal to $|b/a|$.

$$\frac{z^2}{a^2} - \frac{r^2}{b^2} = 1 \quad [1.6a]$$

$$\rho = \frac{b^2}{a + c} \cos \beta \quad [1.6b]$$

Ellipse

Semi-major axis a, semi-minor axis b, focal length $c = (a^2 - b^2)^{1/2}$

$$\frac{z^2}{a^2} + \frac{r^2}{b^2} = 1 \quad [1.7a]$$

$$\rho = \frac{b^2}{a + c} \cos \beta \quad [1.7b]$$

Special properties of these curves that make them useful in optical systems are:

Parabola

A normal(vector) to the curve bisects the angle between a line parallel to the focal (Z) axis and the focal radius. Therefore, incident rays parallel to the focal axis are reflected toward the focal point. Conversely, rays emanating from the focal point emerge as rays parallel to the focal axis after reflection.

Hyperbola

The normal to the curve at every point bisects the angle between the two focal radii at the point. Consequently, a ray towards one focal point that is intercepted by the nearest branch of the hyperbola is reflected toward the opposite focal point.

The hyperbola is the locus of points for which the difference in the length of the focal radii is constant. This difference is $2a$.

Ellipse

The normal to the curve bisects the angle between the focal radii (similar to the hyperbola). Consequently, all rays from one focal point will be reflected to the other.

The ellipse is the locus of all points for which the sum of the lengths of the focal radii is constant. This sum is $2a$.

In the special cases of "shaped" antennas, the basic surfaces are modified by small perturbations from the ideal conic equation. Nevertheless, the perturbations are typically so small that they can be ignored in structural design and surface deformation analysis. It will be seen in Chapter 2 that the original surface shape affects deformation analysis only through the direction cosines of this surface. The perturbations with respect to an idealized nearby approximating conic surface have an insignificant influence upon these direction cosines.

1.6 DUAL-REFLECTOR OPTICAL ARRANGEMENTS

1.6.1 Cassegrain and Gregorian Systems

Cassegrain and Gregorian configurations are shown in Figure 1-11. The Cassegrain system in Figure 1-11a employs a parabolic main reflector and a hyperbolic subreflector. The subreflector is positioned between the main reflector and its focal point. This main reflector focal point is really a "virtual" focus because of the presence of the subreflector. The Gregorian system (Figure 1-11b) has a parabolic main reflector and an elliptical subreflector on the far side of the main reflector focal point. The feeds for both Cassegrain and Gregorian systems are placed at the remote focal points with respect to the subreflector. Both systems capitalize upon the special reflective properties that were described above for parabolas, hyperbolas, and ellipses. The aperture planes and focal planes, shown on edge in the figure, are parallel planes; the aperture plane is tangent to the main reflector at the vertex and the focal plane contains the main reflector focal point.

1.6.2 Magnification Factor

It can be seen for the Cassegrain system (Figure 1-11a) that the aperture angle β at the main reflector virtual focus is larger than angle α , which illuminates the subreflector from the second hyperbola focal point (at the feed). If there were no

subreflector, as in the case of a focal point feed antenna, the feedhorn would need to be designed to illuminate the angle 2β . Here, in the Cassegrain case, the feed illuminates the much smaller angle 2α . This smaller illumination angle requirement provides some advantages for the microwave system.

Hannan, in Ref. 1.5, postulated that there is an equivalent focal point feed parabola of the same diameter D , but with longer focal length, for which the feed angle would also be 2α . The original and equivalent parabolas are shown on Figure 1-12. The magnification factor M is defined as the ratio of the focal length F^* of the equivalent parabola to the focal length F of the original parabola, 'so that $F^* = MF$. Hannan showed that M is given by the ratio of half the tangent of the aperture angle to half the tangent of the feed angle. That is

$$M = (\tan \frac{1}{2} \beta) / (\tan \frac{1}{2} \alpha) \quad [1.8]$$

In terms of the hyperbola parameters c and a (Eq. [1.6]), the magnification factor can be shown to be

$$M = (c+a)/(c-a) \quad [1.9]$$

Typical values of M are in the range of from four to ten for antennas with focal length-to-diameter ratios (F/D) in the range of from 0.25 to 0.50. This implies subreflector diameter-to-main reflector diameter ratios of about one to ten. The magnification factor will be encountered in a later chapter in conjunction with antenna boresight pointing.

1.6.3 Offset Antenna Geometry

The layout of an offset parabolic antenna is equivalent to that of a large diameter "parent" reflector from which a smaller circular region on one side and beyond the center of the parent is used as the reflecting surface. The subreflector is inside of the space between the center of the parent and the nearest rim of the aperture. Figure 1-13 shows the projection of an offset antenna on the aperture plane. In the figure, R_p is the radius of the parent, R_a is the aperture radius of the offset antenna, Y_o is the offset between the center of aperture and the center of the parent, and A is the dimension from center of parent to the nearside rim of the aperture.

The equation of the aperture projection is

$$X^2 + (y - Y_o)^2 = R_a^2 \quad [1.10]$$

and the equation of the reflector surface, which is an extension of Eq. [1.5a] with origin shifted to the center of the aperture, is

$$z = \frac{x^2 + (y+Y_0)^2}{4F} \quad [1.11]$$

Equations [1.10] and [1.11] are based on a right-handed Cartesian coordinate system in which x , y , and z are the coordinates of a point in the directions of the X , Y , and Z axes. The orientation of the X and Y axes are as shown in Figure 1-13; the Z axis is positive when pointing upward from the aperture plane.¹ As a consequence of the right-handed system, the positive direction of the Z axis is always upward above the main reflecting surface.

Figure 1-14 shows a profile of the surface along the Y axis. Three sets of axes are shown: The Y and Z set of axes are those for the parent parabola, the Y_1 and Z_1 axes are parallel to the Y and Z set but offset by Y_0 and Z_0 where $Z_0 = Y_0^2/4F$ (Eq. [1.5a]), and the Y_L and Z_L axes relate to a local coordinate system in which the Y_L axis is tangent to the surface at point p_1 (which is on the centerline of the offset aperture). The angle between the " L " and the " 1 " coordinate systems is ϕ_a , in which $\phi_a = \tan^{-1} Y_0/2F$. The X axis coordinates are the same for all three systems.

One property of a parabola of revolution is that the curve of intersection with any right circular cylinder with an axis offset from, but parallel to, the focal (Z) axis is a plane ellipse. When r is the radius of the cylinder, the semi major axis of the ellipse is $r/\cos\phi_a$ and the semi minor axis is r . The planes of intersection of all such cylinders whose axes coincide with the Z_1 axis of Figure 1-14 are parallel, and the centers of the ellipses contained in these planes have Z_1 coordinates equal to $r^2/4F$. A true view of the curves of intersection is given by the projections in the X - Y_L coordinate plane. The coordinates of the centers of the intersection curves in the local coordinate system are 0 , $r^2/4F \sin\phi_a$, $r^2/4F \cos\phi_a$.

According to the above, when the cylinder encloses the offset aperture, the major axis is $R_a/\cos\phi_a$, the minor axis is R_a (in the X direction), and the center of the ellipse has $Z_1 = R_a^2/4F$. The center of this ellipse in the local system has coordinates 0 , $R_a^2 \sin\phi_a/4F$, and $R_a^2 \cos\phi_a/4F$. More explicitly,

¹This coordinate system is used throughout the text for az-el antennas. The convention is that the X axis is always horizontal and parallel to the elevation axis and the Y axis is positive upward when the antenna is facing the horizon.

in terms of the points noted in Figure 1-14, the center of the ellipse has coordinates given by the distances O, p_1-p_6, p_6-p_4 . This ellipse lies in the plane perpendicular to the plane of the figure that contains the points p_3, p_4 , and p_5 .

Figure 1-15 shows an offset antenna that has been intersected by 12 cylinders with equally spaced radii. Figure 1-15a is a 3-dimensional view in the X-Y-Z coordinate system. An outline of the parent parabolic surface is marked by * symbols. Figure 1-15b is a projection of the rings on the X-Y_L local coordinate system plane. This shows a true view of the elliptical intersection curves, and also shows that the ellipses are eccentric (to a maximum offset of $R_a^2 \sin \phi_A / 4F$).

The transformation equations for the three coordinate systems, using $S = \sin \phi_A$ and $C = \cos \phi_A$, are

$$\begin{Bmatrix} y_1 \\ z_1 \end{Bmatrix} = \begin{Bmatrix} y - Y_o \\ z - z_o \end{Bmatrix} \quad [1.12]$$

$$\begin{Bmatrix} y_L \\ z_L \end{Bmatrix} = \begin{bmatrix} C & -S \\ S & C \end{bmatrix} \begin{Bmatrix} y_1 \\ z_1 \end{Bmatrix} \quad [1.13]$$

Returning to Figure 1-14, and using Eqs. [1.12] and [1.13] to compute the local coordinates of the points p_3 and p_5 , shows that both points have the Z_L coordinate of $p_4 = (R_a^2 C / 4F)$. Computing the Z coordinate of p_4 in the parent parabola coordinate system as the average of the coordinates of p_4 and p_5 results in $Z_4 = (Y_o^2 + R_a^2) / 4F$. A plane perpendicular to the Y-Z plane at a distance of Y_o from the Z axis will intersect the aperture plane-enclosing cylinder at $x=R_a$ and $y=Y_o$, and the Z coordinate on the parabolic surface here will again be $(Y_o^2 + R_a^2) / 4F$, which shows that p_4 is the projection of the intersection of the aperture cylinder and parabolic surface on the plane of Figure 1-14.

All of the foregoing relationships apply to any parabolic surface of revolution that, either physically or conceptually, is intersected by a circular cylinder offset from the axis of the parabola.

One more particular feature that conceivably could be used in the preparation of the tooling to either fabricate or check the surface is a single planar template, which could be used to define the contour of the surface. This template would be used in planes parallel to either the Y-Z plane or parallel to the X-Z

plane. In particular, if the template were held parallel to the Y-Z plane at a fixed value of x, the surface equation would be

$$z = y^2/4F + K \quad [1.15]$$

where K is a constant that depends upon the X coordinate at which the template is placed. The equation shows that the shape, which is a function only of y, does not change at each x location. However, the template has to be held at a different offset in the Z direction for every distinct value of x. This feature is well known, but we are not aware of any attempt, successful or otherwise, to exploit it. Another special type of surface template depends upon having fixed length pendulous probes suspended from a rigid bar. These probes define the theoretically exact contour when aligned parallel to the Z axis and the bar is aligned with a radial secant to the surface. This type of template could be used anywhere along any radial plane of the surface, but the idea also has not appeared practical enough for exploitation.

1.7 THE BLOCKED SHADOW

By using offset antenna geometry, obscuring of the main reflector by the subreflector and support leg shadows is avoided. Nevertheless, the antenna systems that predominate today are not offset and therefore are subject to these blocking effects. The blocked area consists of two types of shadows: plane wave and spherical wave. The plane wave blocking effects comprise the projections of the subreflector and an upper portion of the support legs. The spherical wave blocking is the shadow of rays emanating from the focal point that intersect the lower portion of the support leg. Figure 1-16 shows typical shadows projected onto the surface plane. Herndon (Ref. 1.6) developed a comprehensive numerical integration computer program to calculate the blocked areas; but results close to those from the computer program can easily be obtained with some simple approximations.

Figure 1-17a is a profile sketch of the reflector in the plane of one of the support legs. The leg is assumed to have a trapezoidal cross-section that is opaque with respect to transmission of microwave energy. Symbols of the figure are:

- F = Focal length
- R = Main reflector radius
- R_s = Subreflector radius
- s = Radial distance to centerline of leg at the intersection with the main reflector surface
- Z₀ = Z coordinate at S
- Z_s = Z coordinate at back of subreflector
- h = Half leg depth
- w₁ = Width at inside face of leg

w_0 = Width at outside face of leg
 β = Angle from the focal point to the rim of the
 main reflector

ϕ = Slope of surface at intersection with the centerline of
 the leg
 ψ = Slope angle of the leg

Figure 1-17b is an expanded detail at the intersection of the leg with the surface. S_1 and S_0 are the radial distances to the points where the extensions of the inner and outer faces of the leg would intersect the surface, and Q is the distance along the tangent from the leg centerline to either of the intersection points at S_1 or S_0 . The relatively small curvature makes it reasonable to replace the curved surface by the tangent in the vicinity of S . Q is given by

$$Q = h / \sin (\psi + \phi) \quad [1.16]$$

therefore

$$S_1 = S - Q \cos \phi \quad [1.17a]$$

and

$$S_0 = S + Q \sin \phi \quad [1.17b]$$

Figure 1-17c shows the spherical wave shadow of the leg as a trapezoid of length $R - S_0$. To find the maximum width of the trapezoid at the rim of antenna w_M , it is necessary to find the distances X_1 and X_0 where a ray from the focal point to the rim crosses the inner and outer faces of the leg. To find X_1 , for example, we have

$$F - Z_1 = X_1 / \tan \beta + (S_1 - X_1) \tan \psi \quad [1.18]$$

in which Z_1 is the Z coordinate at S_1 . By introducing Z_0 , the Z coordinate at S_0 , a similar expression can be formed for X_0 , and these expressions can be used to determine X_1 and X_0 .

If the width at the outer face of the leg governs the spherical wave shadow, then the width of the trapezoid at S_0 is w_0 and the width at the rim is

$$w_M = w_0 R / X_0 \quad [1.19]$$

If the width at the inner face of the leg governs, it is necessary to find the width of the trapezoid at S_0 . To do this, we use the distance X_{10} , which is where a ray from the focal

point to the surface at S_0 intersects the inner leg face. X_{I0} can be found from the following expression

$$F - Z_I = X_{I0} / \tan \beta_p + (S_I - X_{I0}) \tan \psi \quad [1.20]$$

in which

$$\tan \beta_p = S_0 / (F - Z_0) \quad [1.21]$$

and in this case the width of the spherical wave blocking trapezoid at its base is

$$w_B = w_I S_0 / X_{I0} \quad [1.22]$$

and the width at the rim is

$$w_M = w_I R / X_I \quad [1.23]$$

The ideal profile for the leg cross-section would be when the outer face provided the same width at the rim as the inner face. In this case, the outer width would be

$$w_o(\text{ideal}) = w_I S_I / X_{I0} \quad [1.24]$$

The foregoing computations imply several approximations that are expected to have only a minor effect on the results. Some of these are:

- (1) The leg is assumed to be entirely opaque.
- (2) The spherical wave leg shadow is modelled by the projection of a trapezoid on the aperture plane. The long sides of the trapezoid actually are curved and the approach here slightly overestimates the shadow.
- (3) The curve of the outer reflector rim is replaced by the straight edge of the trapezoid.
- (4) The leg profile is taken to have a constant cross-section for the full length, and any customary tapering towards a narrow point at the leg base is ignored.

A MATLAB program to calculate the blocked shadow essentially as described above is presented in Appendix 1-A.

1.8 THE ANTENNA SURFACE

The antenna surface is the primary microwave feature of the antenna reflector system, and is the essential component to either collect the microwave energy signal on reception or to reflect the energy on transmission. Antenna microwave efficiency is dependent on maintaining highly precise tolerances with respect to the shape of the ideal surface curve. Surfaces of

large antennas are traditionally composed of an arrangement of many (frequently hundreds) of small, carefully manufactured, individual separate panels.

1.8.1 Symmetrical Panel Arrangements

Figure 1-18 shows the reflecting surface and panel arrangement of a typical symmetrical 34m antenna. The outer six rings are subdivided into 48 separate panels, the next two inner rings contain 24 panels each, and the first inner ring has 12 panels. The center of the aperture, which is blocked by the subreflector, is open. All the panels are trapezoidal, and although there are significant differences in the areas of panels from ring to ring, the average area (projected on the aperture plane) of the 348 panels is 2.6 square meters. For convenient and accurate manufacturing, the range of panel areas tend to be from 2 to 5 square meters. The tooling for panel fabrication requires only one fixture per panel ring, because all panels in each ring are the same.

The panels are supported by radial and circumferential trusses of the backup structure. The nodes of the backup structure trusswork are arranged to be aligned with the panel corners so that each panel can be supported from a backup structure node by an adjustable jack. This panel support arrangement leads naturally to the conventional "rib and ring" backup structure configuration, in which the ribs are radial trusses that are the major structural components and the rings are circumferential (hoop) trusses that provide auxiliary supporting interaction.

1.8.2 Offset Arrangements

The convenient adaptation in symmetrical antennas of panels to backup structure does not hold for offset antennas. Offset antennas impose a choice between the need to provide many different panel fixtures or to sacrifice the desirably repetitive nature of rib and ring construction. Figure 1-19 shows three alternative arrangements for the panel and backup structures for offset antennas.

The offset rib and ring arrangement in Figure 1-19a provides only an approximation of the advantages of true rib and ring construction. As shown previously, the rings are elliptical and not circular, and there is no repeatability to reduce the number of panel fabrication fixtures.

The tetrahedron module backup structure in Figure 1-19b is equivalent to an interlocking set of two kinds of tetrahedral. One set of tetrahedra has its bases near the front surface and

the other set has its bases at the back surface of the backup structure. Particular rod members of the structure are shared by both sets of tetrahedral. The inset sketch provides an idea of the rod arrangement. The panels can either be of triangular or of hexagonal shape. The hexagonal panels would encompass a " pattern of six triangles of the figure, such as the group in the inset, so that alternate corners of each hexagon can be supported by jacks. Although all panels would necessarily be different, the arrangement does provide the opportunity for a three-point statically determinate support system, which is preferable to the four-point support of trapezoidal panels. The tetrahedron-type arrangement with hexagonal panels is frequently adopted for orbiting space antennas and has also been used successfully for small symmetrical ground-based antennas. In the case of the ground antennas it was possible to machine the entire surface in one setup.

The masked rib and ring format of Figure 1-19c requires only one panel fabrication fixture for each of its rings. (This is still about twice as many fixtures as would be required for a symmetrical antenna of the same aperture.) The backup structure is an isolated portion of the backup structure that would be used in constructing the complete parent antenna; ribs are aligned along the parent radii and rings follow the central parent circles. The structure loses some of the advantages of symmetry and structural efficiency of the traditional rib and ring framing and is more difficult to design and fabricate than a symmetrical antenna.

1.8.3 Surface Panel Installation

Panels are aligned in the field by adjustment of the corner jack heights. A customary method of alignment is to use a precise theodolite placed at the center of the aperture to read the position of the panel corners and to determine the necessary adjustments for the jacks. A tooling tape is frequently used to set the radial distances for theodolite targets placed at the panel corners. When the targets are in position at the prescribed radii, the elevation angle of the theodolite can be established for each target ring and the jacks are adjusted accordingly to provide the desired surface. After the panels are set via theodolite measurement and jack adjustment, an important antenna will be remeasured either by theodolite or by microwave measurements. Microwave holography (Ref. 1.7) or photogrammetric measurement (Ref. 1.8) are techniques that have been used effectively for this purpose. After remeasurement, the surface is re-adjusted to reduce any observed residual errors. Iterative repetitions of the process can be undertaken, depending upon the accuracy required for the surface. At this writing, procedures for accurate alignment of surface panels are still being studied,

with much attention being given to improved measurement techniques and to automation of these activities.

Field adjustment of the panels is almost always necessary for large antennas because it is either uneconomical, or even impossible, to fabricate and install the tons of backup structure components to the precise tolerances needed for the final surface. Typical installation surface accuracy specifications are from 0.1 mm to 0.5 mm root-mean-square (rms), which is much more restrictive than commercial fabrication and installation practice. The need to provide field adjustment is one of the reasons why the panels are parasitic; i.e., they are only required to support their own weight and the local environmental loadings (wind, snow, ice) applied directly to their surface. This way, the panels are not required to participate in the major structural action of the backup structure. It would be extremely difficult to provide reliable load transfer between the backup structure trusses and the panels. There are also other practical reasons that enforce the logic of parasitic panels, and non-parasitic panels are unusual.

1.8.4 Surface Area

It is useful to be able to calculate the surface area of the panels for the purpose of estimating the weight, costs, and loading on the backup structure. The surface area A_s of a symmetrical antenna is

$$A_s = 8/3 \pi F^2 [(1+R^2/4F^2)^{3/2} - 1] \quad [1.25]$$

When the focal length-to-diameter ratio is replaced by the symbol Φ and the projected aperture area is denoted by A_o , then Eq. [1.25] can be rewritten to give the ratio of surface area to aperture area as

$$A_s/A_o = 32/3 \Phi^2 \{1 + [1/16\Phi^2]\}^{3/2} - 1 \quad [1.26]$$

The surface area of an offset antenna can readily be calculated by numerical integration. From Figure 1-20, an increment in the planform area ΔA_i is given in terms of the variable parent radius R_i , the half central angle θ_i , and the increment in radius ΔR

$$\Delta A_i = 2 R_i \theta_i \Delta R \quad [1.27]$$

The central angle can be found from R_i , the aperture radius R_a , the offset Y_o , and the law of cosines, so that

$$\theta_i = \cos^{-1} [(R_i^2 - R_a^2 + Y_o^2) / (2 R_i Y_o)] \quad [1.28]$$

The surface area is equal to the planform area divided by the cosine of the surface slope ϕ_1 , where ϕ_1 can be obtained by differentiating the equation of the parent curve (Eq. [1.5a]), e.g.

$$\phi_1 = \tan^{-1} R_1/2F \quad [1.29]$$

A program to compute surface area factors for symmetrical and offset antennas is given in Appendix 1-B. Figure 1-21 shows curves of the area ratio factors for a range of focal length-to-diameter ratios. The figure shows that offset antennas have smaller surface areas than symmetrical antennas of the same aperture area. This has been confirmed by an independent method of computation.

REFERENCES

- 1.1. Haddock, F. T., "Introduction to Radio Astronomy,"
Proceedings of the **IRE**, 46, 1, January 1958, 3-12.
- 1.2. Jansky, Jr.; C. M., "The Discovery and Identification by
Karl Guthre Jansky of Electromagnetic Radiation of
Extraterrestrial Origin in the Radio Spectrum," Proceedings
of the **IRE**, 46, 1, January 1958, 13-14.
- 1.3. Reber, G., "Early Radio Astronomy at Wheaton, Illinois,"
Proceedings of the **IRE**, 46, 1, January 1958, 15-22.
- 1.4. Lovell, B., Sir, The Story of **Jodrell** Bank, NY: Harper &
Row, Publishers, 1968,
- 1.5. Hannan, P. W., "Microwave Antennas Derived from the
Cassegrain Telescope," **IRE Trans. Antennas and Propagation**,
AP-9, March 1961, 140-153.
- 1.6. Herndon, J., "Efficient Antenna Systems: A Program to
Calculate the Optical Blockage by the Quadripod on Large
Microwave Antennas," **Space** Programs Summary 37-48, V. II,
Pasadena, California: Jet Propulsion Laboratory, California
Institute of Technology, January 31, 1968, 58-63.
- 1.7. Rochblatt, D. J., A User Manual, Data Processing Software
for Microwave Antenna Holography: Computer Programs for
Diagnostics, Analysis, and Performance Improvement of Large
Reflector and **Beamwaveguide** Antennas, Pasadena, California:
Jet Propulsion Laboratory Internal Document D-10237, January
15, 1993.
- 1.8. Fraser, C. S., "Microwave Antenna Measurement,"
Photogrammetric Engineering and Remote Sensing, 52, October
1986, 1627-1635.

LIST OF FIGURES

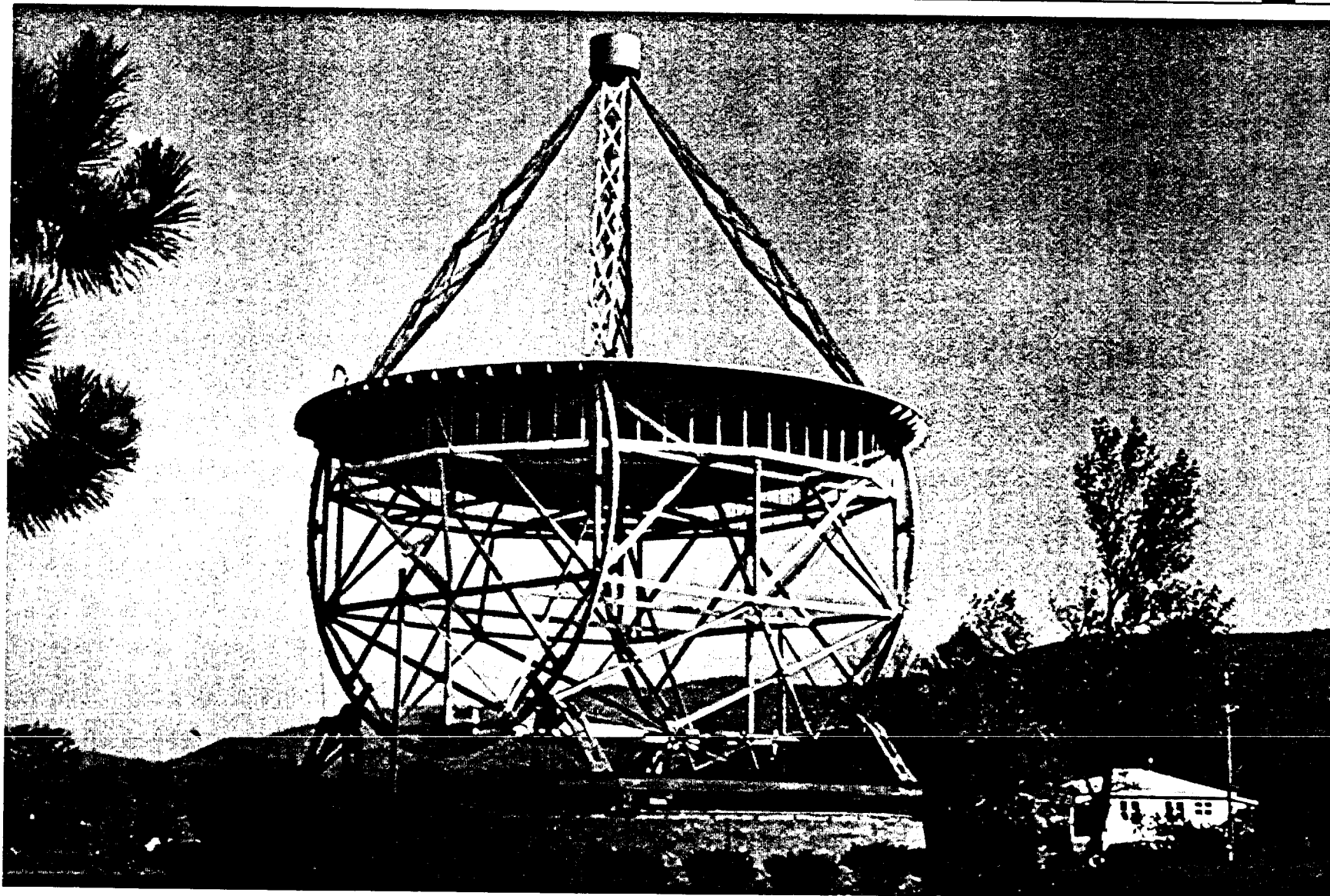
- 1-1. Reber Antenna
- 1-2. Jodrell Banks Antenna
- 1-3. 34m Antenna
- 1-4. 34m Azimuth-Elevation Antenna Configuration
- 1-5. NASA Deep Space Network 70m Antenna at Goldstone,
California
- 1-6. Hour-Angle and Declination (HA-Dee) Axes
- 1-7. HA-Dee Antenna
- 1-8. Beam-Waveguide Antenna
- 1-9. Offset Antenna Concept
- 1-10. Conic Sections (a,b,c)
- 1-11. Dual-Reflector Systems (a,b)
- 1-32. Equivalent Parabola
- 1-13. Projection of Offset Antenna on Aperture Plane
- 1-14. Offset Antenna Profile
- 1-15. Offset Antenna Views (a,b)
- 1-16. Plane and Spherical Wave Shadows
- 1-17. Geometry of Aperture Blocking (a,b,c)
- 1-18. Reflector Surface Panels
- 1-19. Offset Antenna Panels
- 1-20. Incremental Surface Area
- 1-21. Surface Area Factors

APPENDIX 1

- 1-A. Blocking Program
- 1-B. Surface Area Program

DEVELOPMENTS IN ANTENNA STRUCTURAL ENGINEERING REBER'S 1938 WOODEN ANTENNA

JPL



RL-1
7-21-92

1-1



RIGHT

31. 1957. The scene inside the bowl during the summer. Some of the steel plates for the last 9 rows of membrane are lying in the bowl near the welding equipment. Our first aerial can be seen on the top of the central mast at the focus.

INLIS\N

32. 20 JUNI 1957. The bowl of the telescope is moved in elevation for the first time. The membrane is incomplete and some of the supporting scaffolding is still visible.

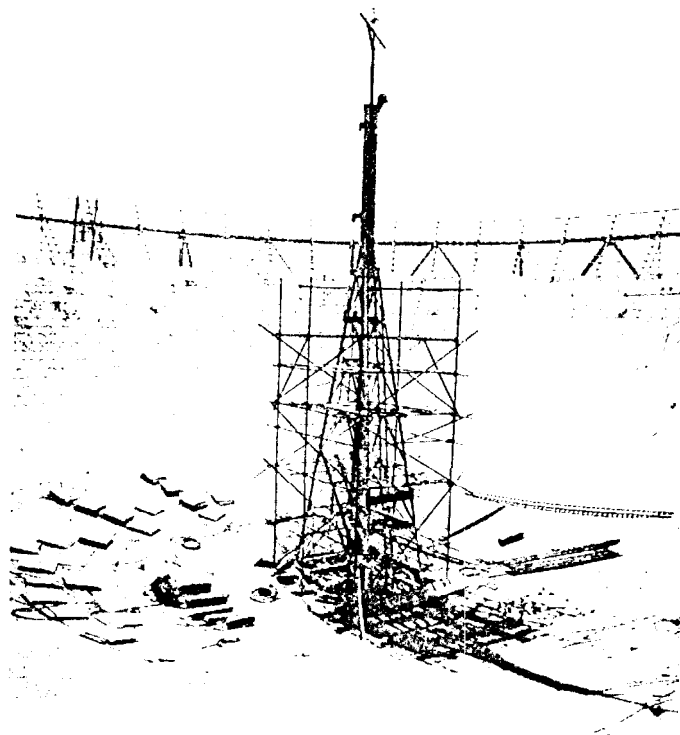
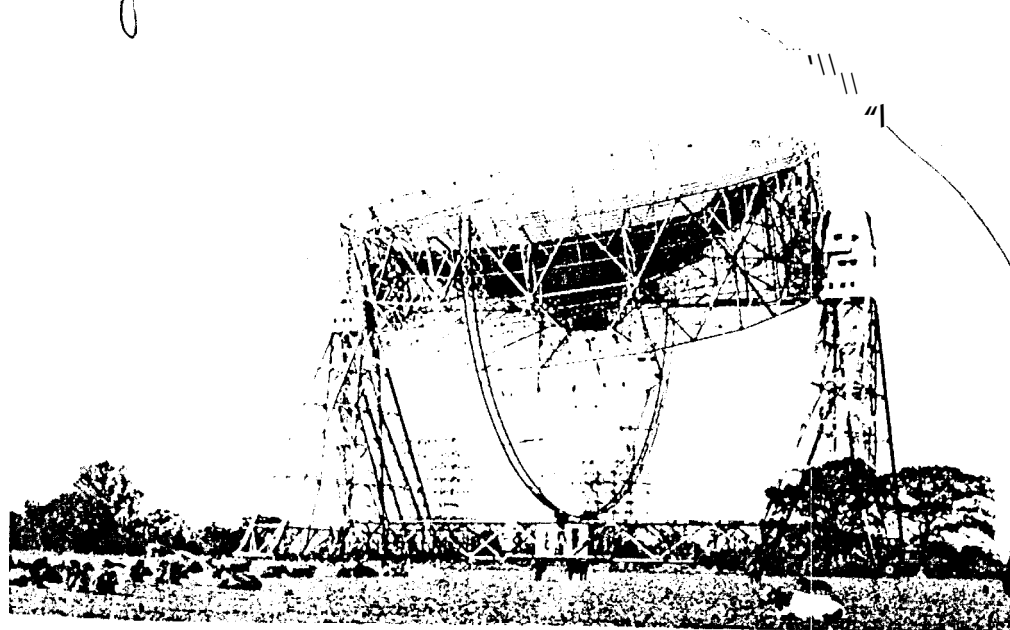
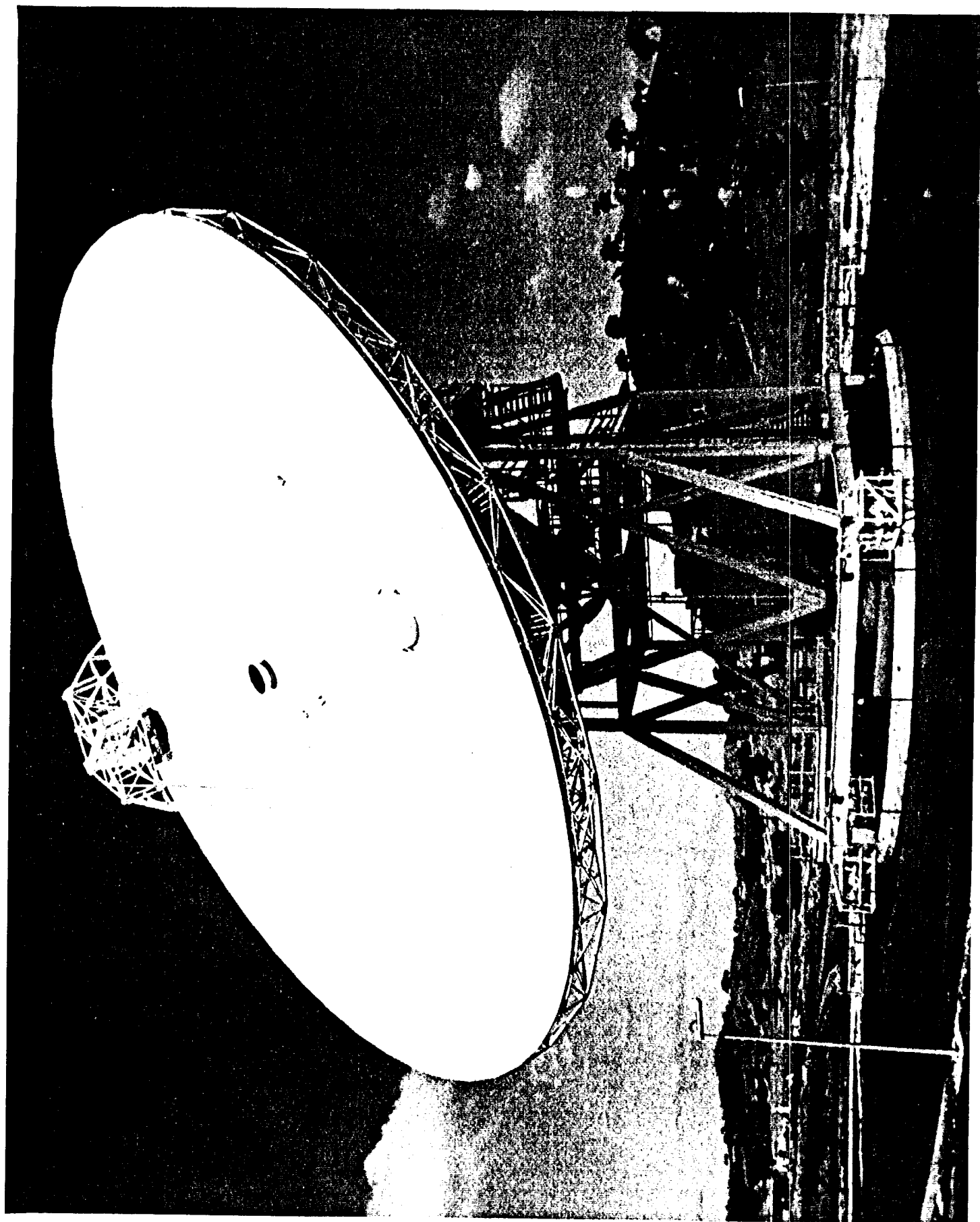


Fig 1-2



31. May the welders can be seen at work in the bowl with approximately 17 more rows of plates to be fixed. The large cranes have disappeared and the bowl is still supported on two scaffolding towers. (Aerofilms Ltd. Copyright reserved.)



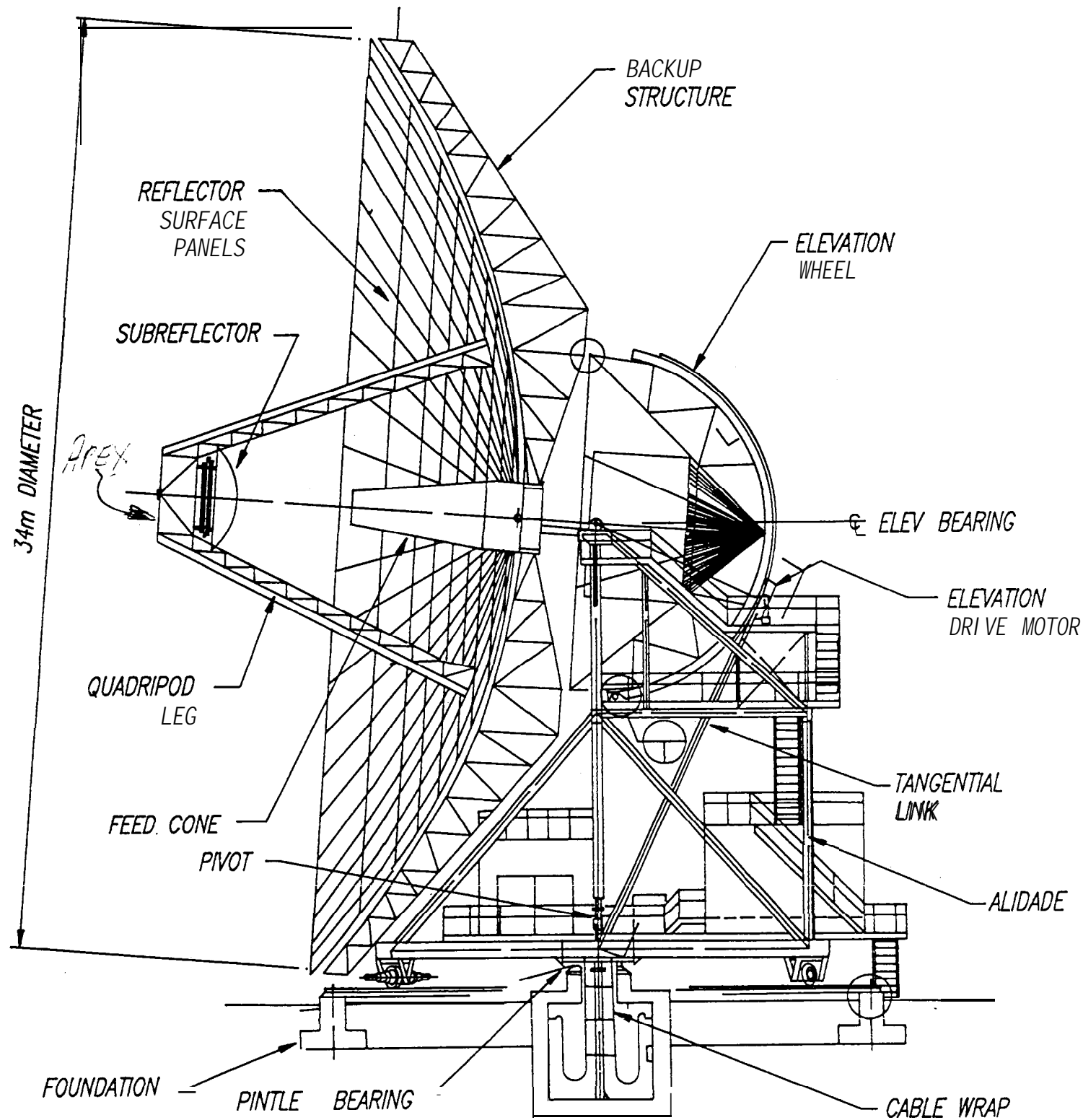
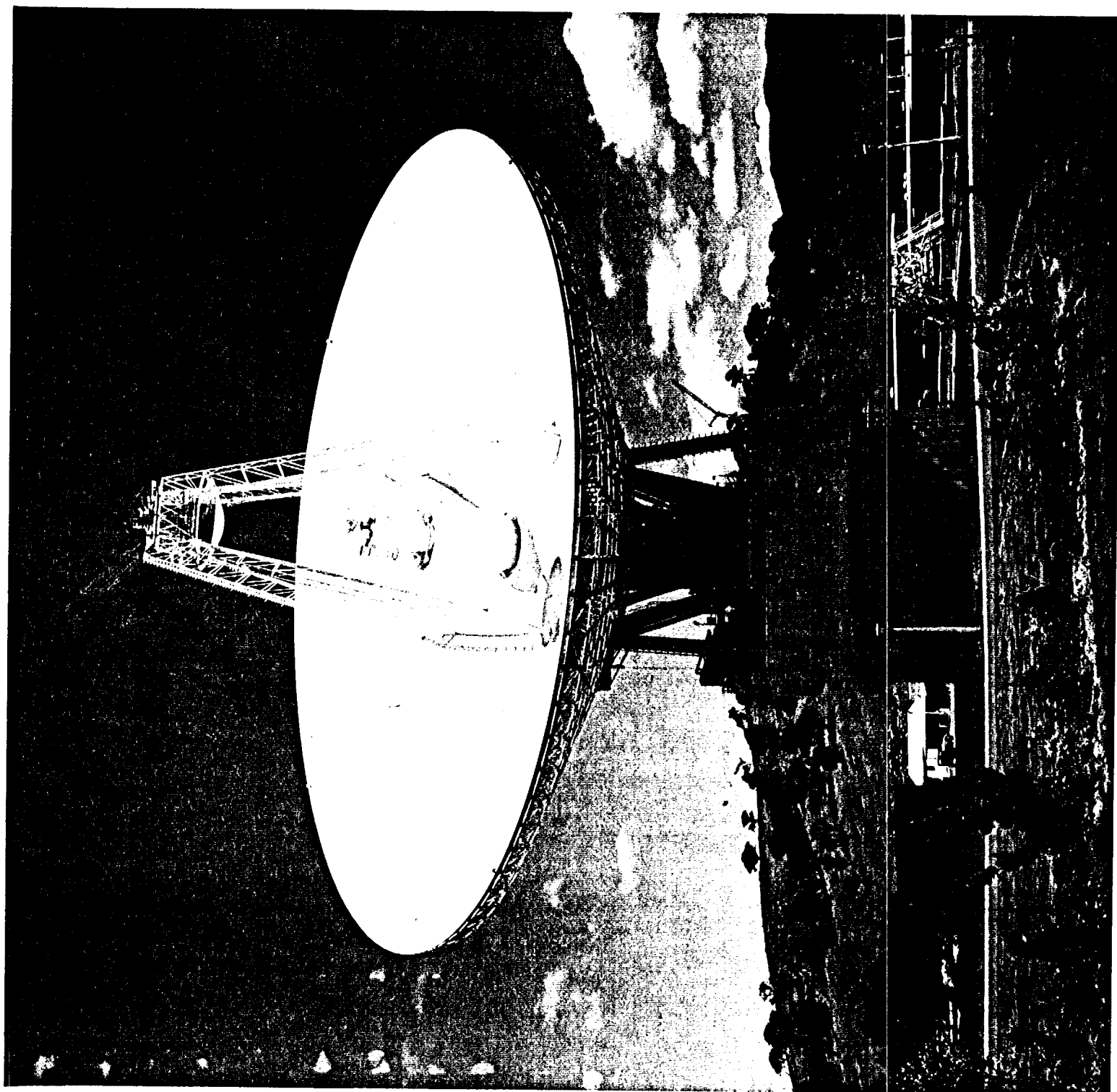


Fig 1-4



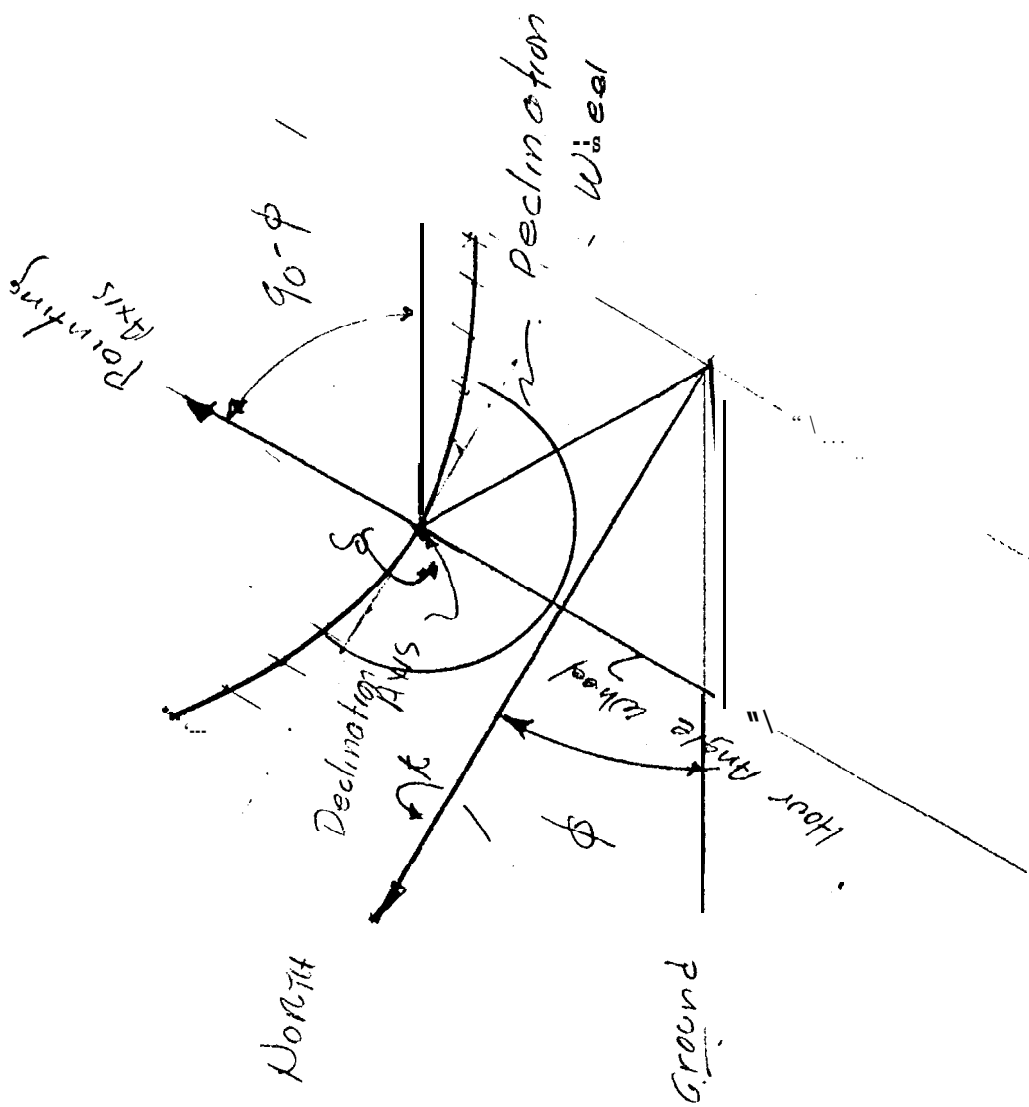
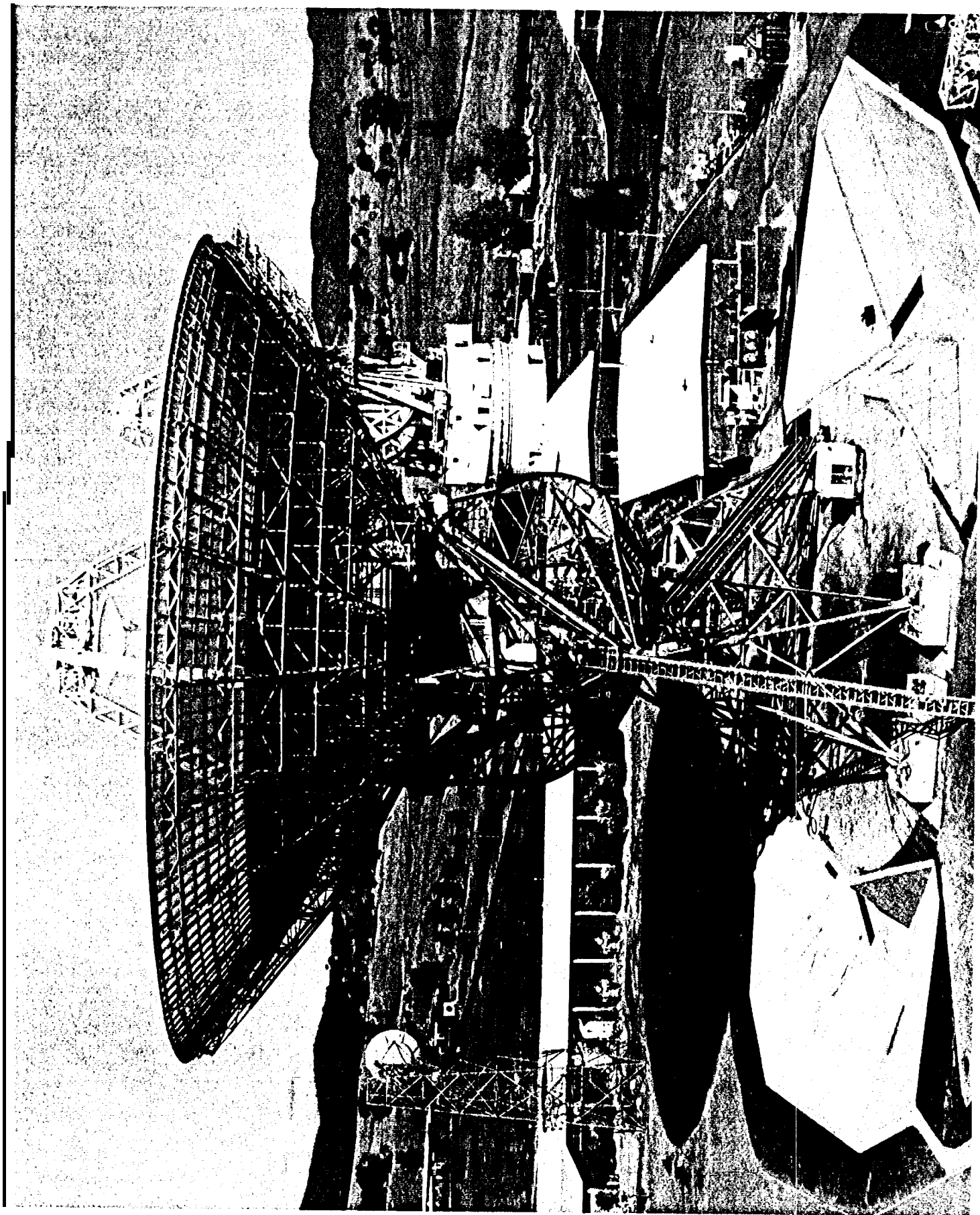


Fig 14



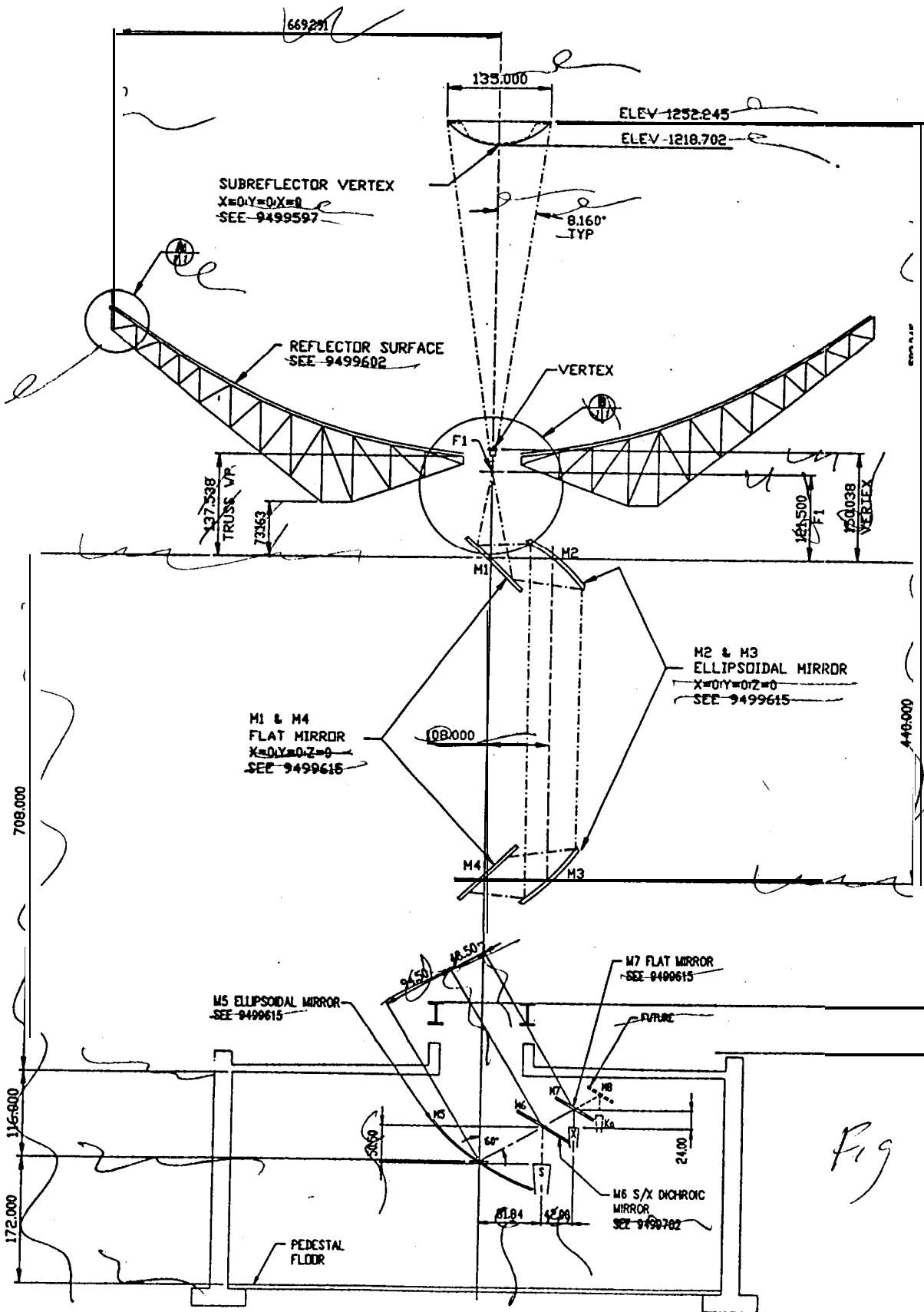


Fig 1-8



OFFSET ANTENNA ~~CONFIGURATION~~

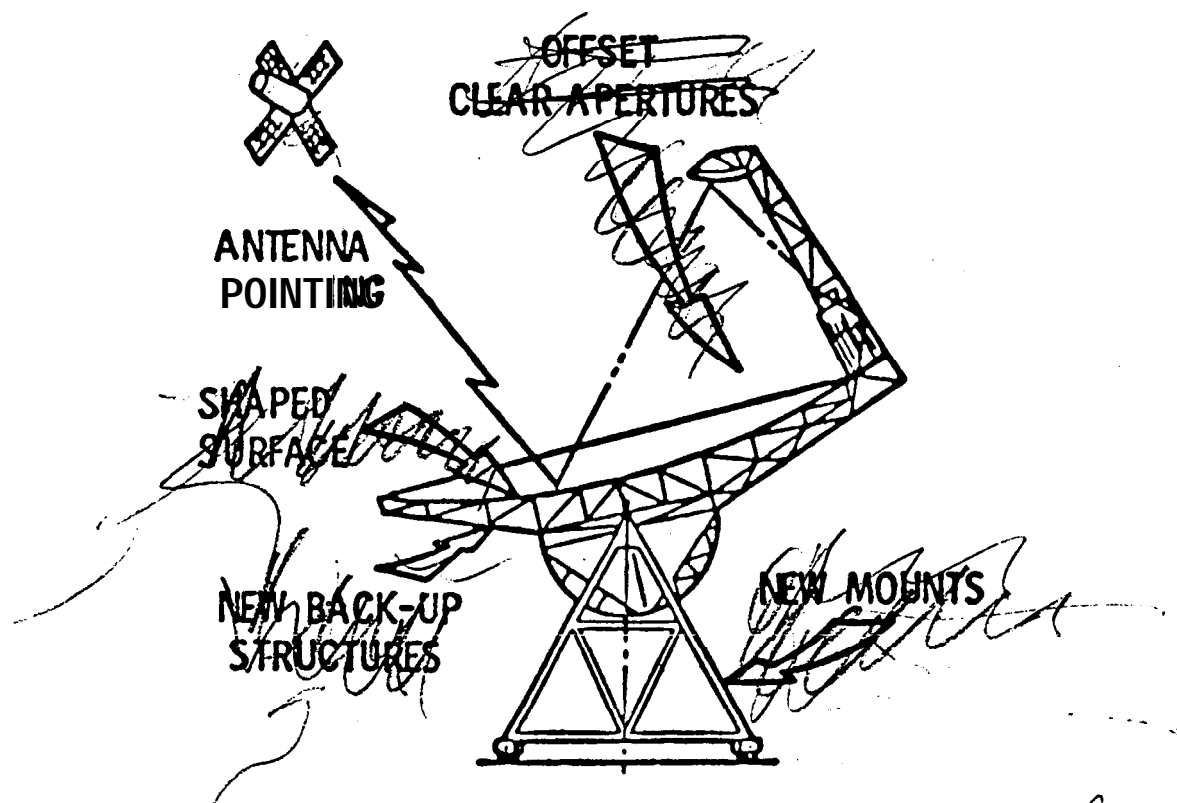
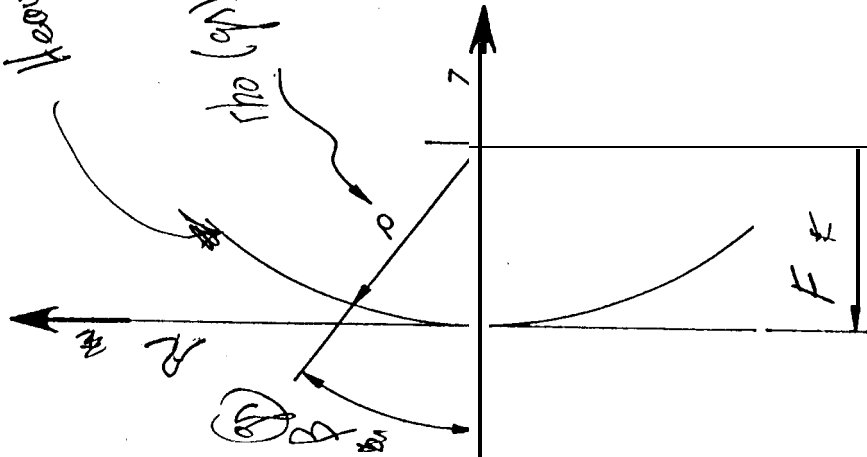


Fig 19

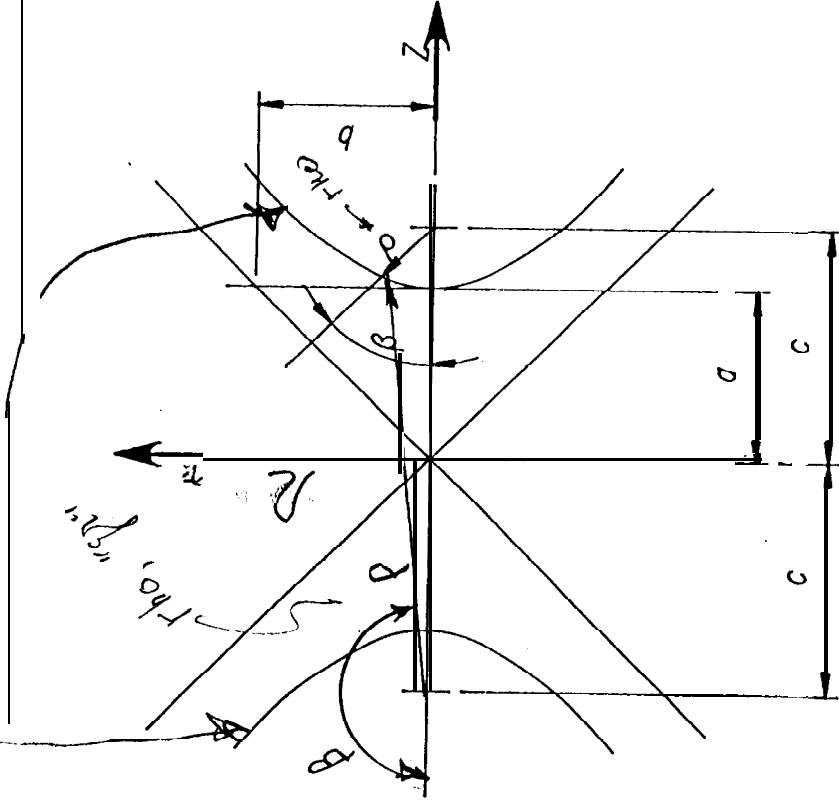
Don Mar 17

Weight

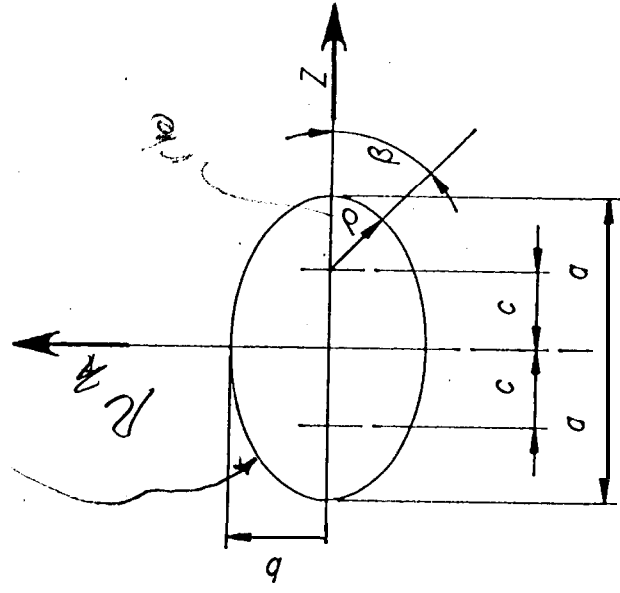
Heavier line



a) PARABOLA



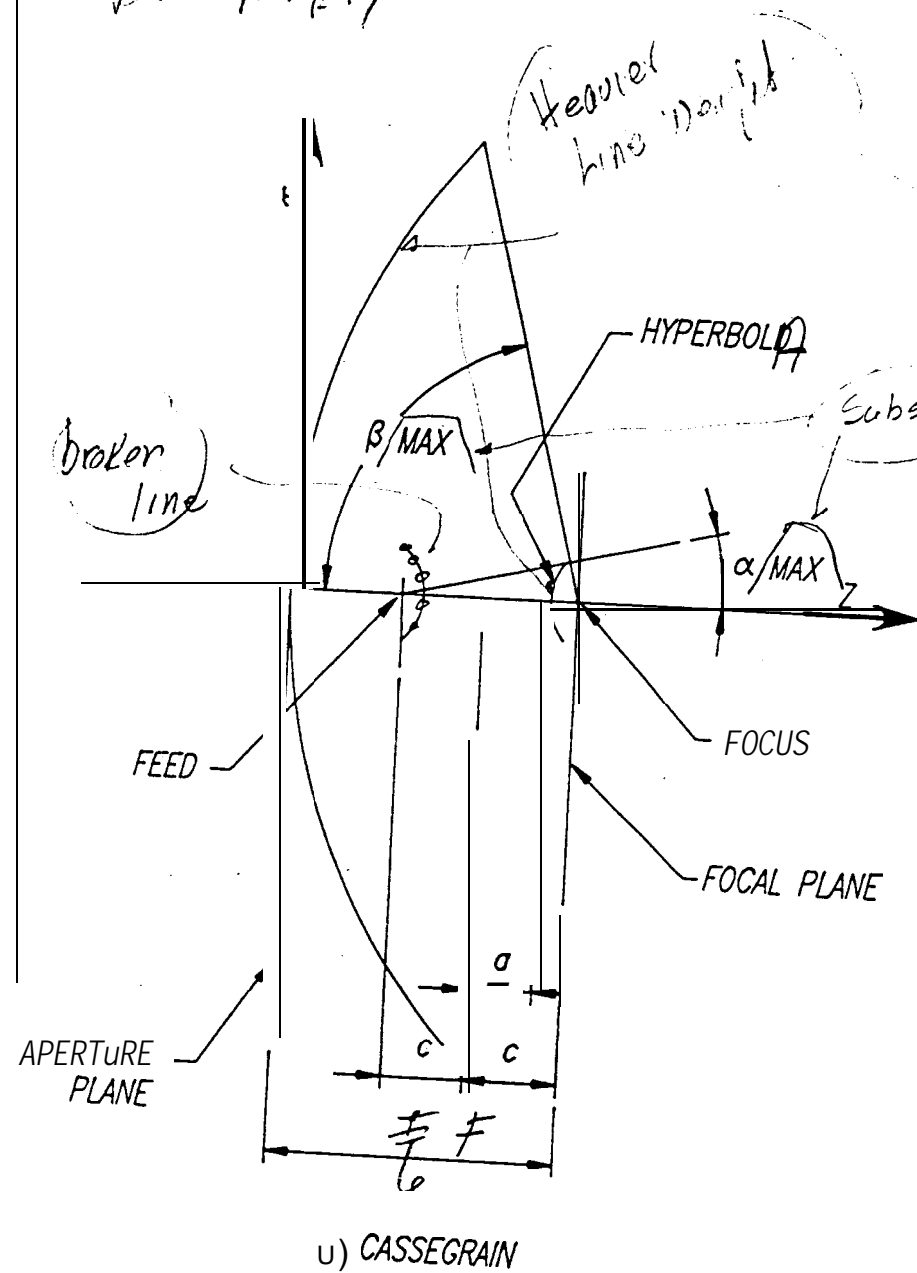
b) HYPERBOLA



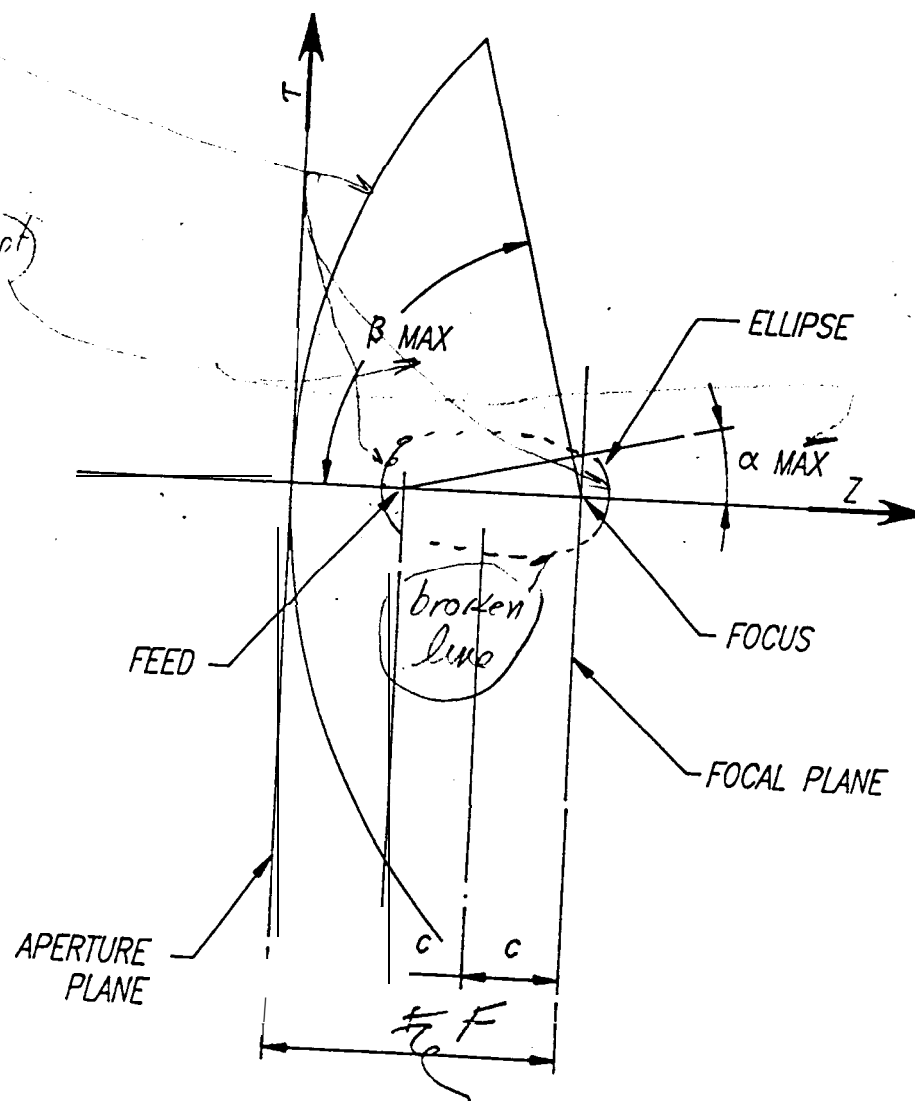
c) ELLIPSE

Figure 1-10 Conic Sections

En 10/4/17



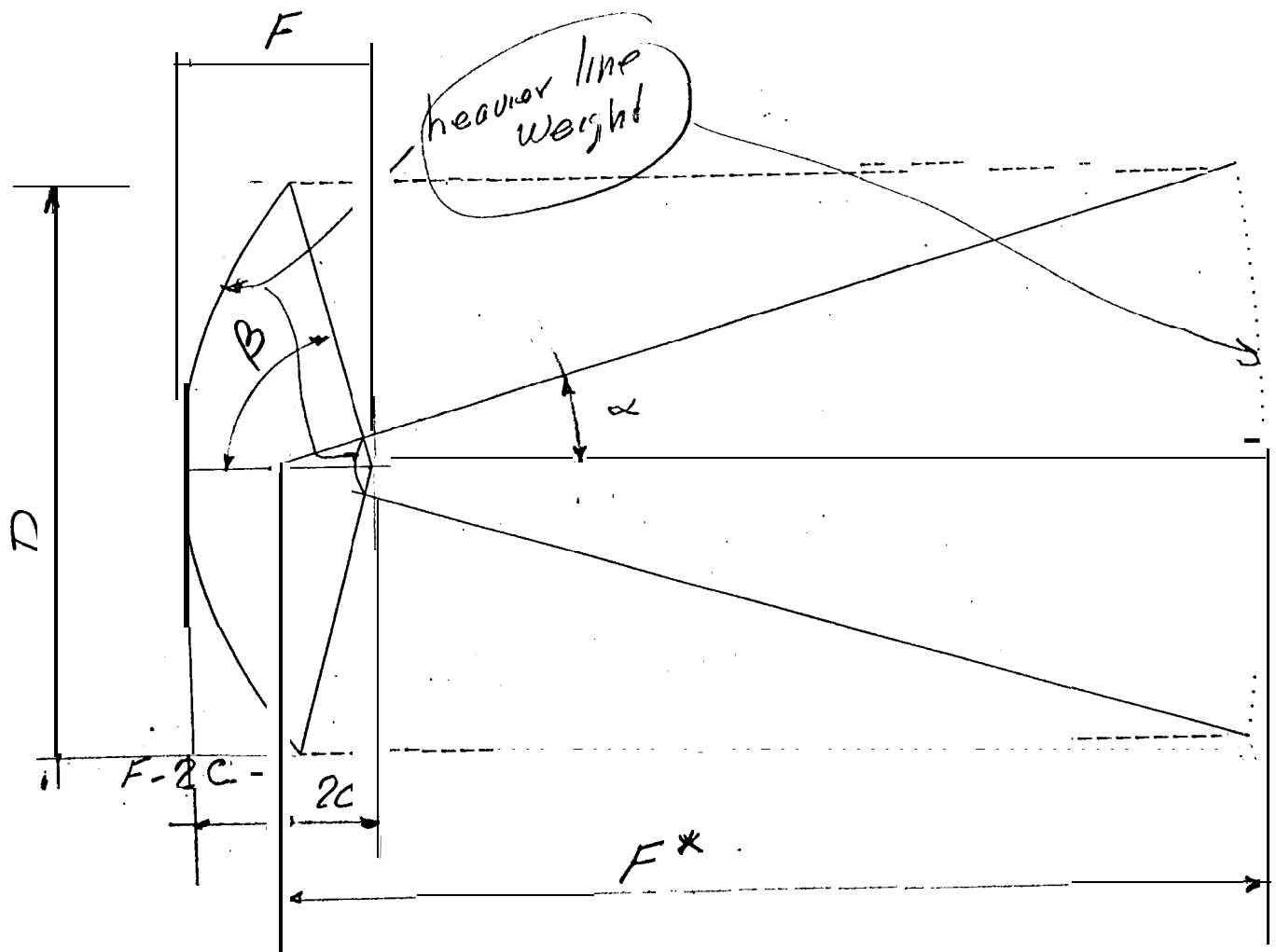
a) CASSEGRAIN



b) GREGORIAN

1-11

Fig 1-12



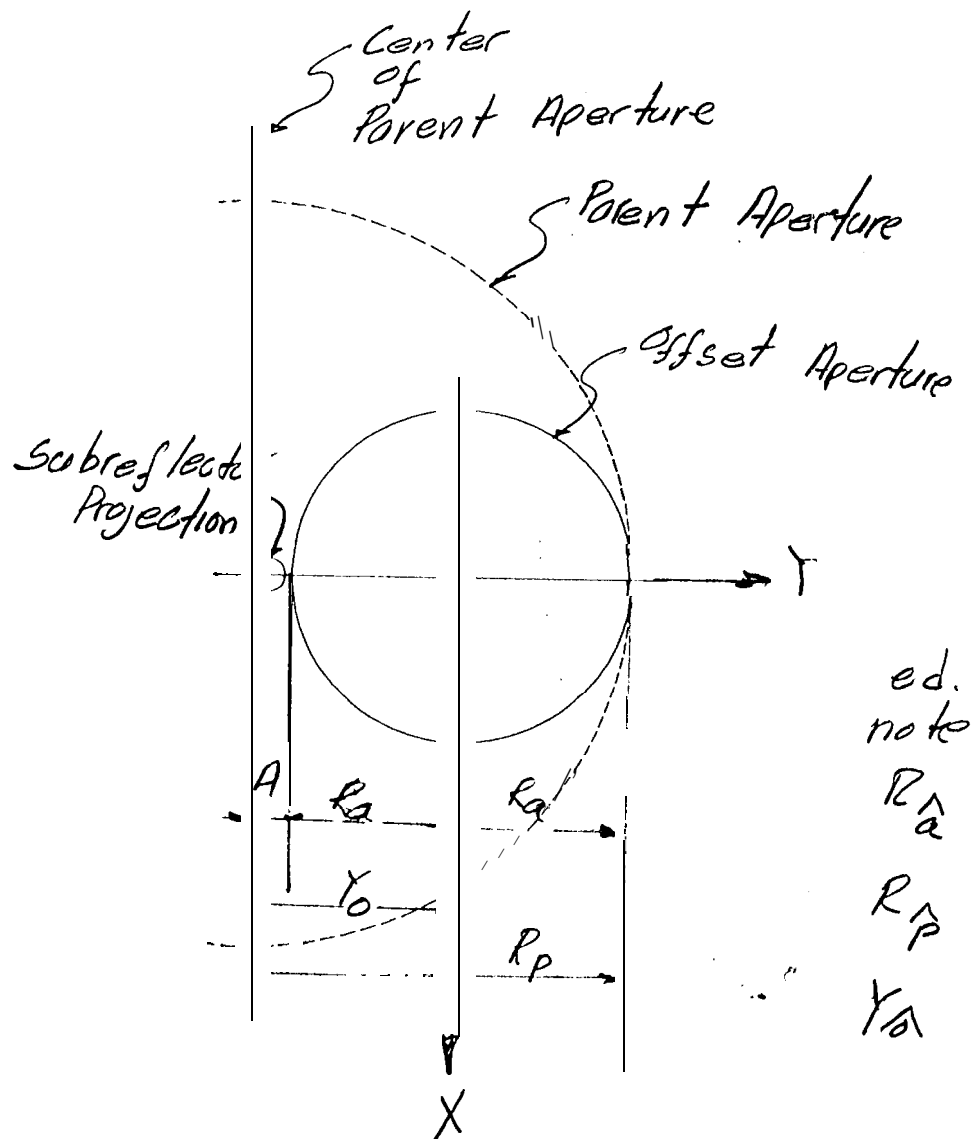


Figure 1-13
Projection of Offset Antennas
On The Aperture Plane

The diagram illustrates the geometry of a parabolic antenna system, showing both a cross-sectional view and a perspective view.

Cross-Sectional View (Left):

- A vertical Z -axis passes through the focus of the parabola, which is located at a distance F from the vertex.
- The focus is labeled "Focus".
- Points P_3 and P_6 are marked on the parabola's surface.
- Horizontal distances from the vertex to the projection of P_3 and P_6 are labeled A and R_A , respectively.
- A distance Y_{0A} is also indicated along the horizontal axis.

Perspective View (Right):

- This view shows the coordinate system with local axes Z_L and Y_L .
- A dashed line represents the path of a ray or signal, originating from a source point P_3 and reflecting off the surface towards a receiver point P_6 .
- An angle ϕ_a is shown between the Y_L axis and the direction of the reflected ray.
- An angle ρ_0 is indicated near the receiver point P_6 .
- A note "heavy line weight" is circled, pointing to the solid line representing the surface profile.

Fig/-14

11/19
Adm. R. P. 19

1-15

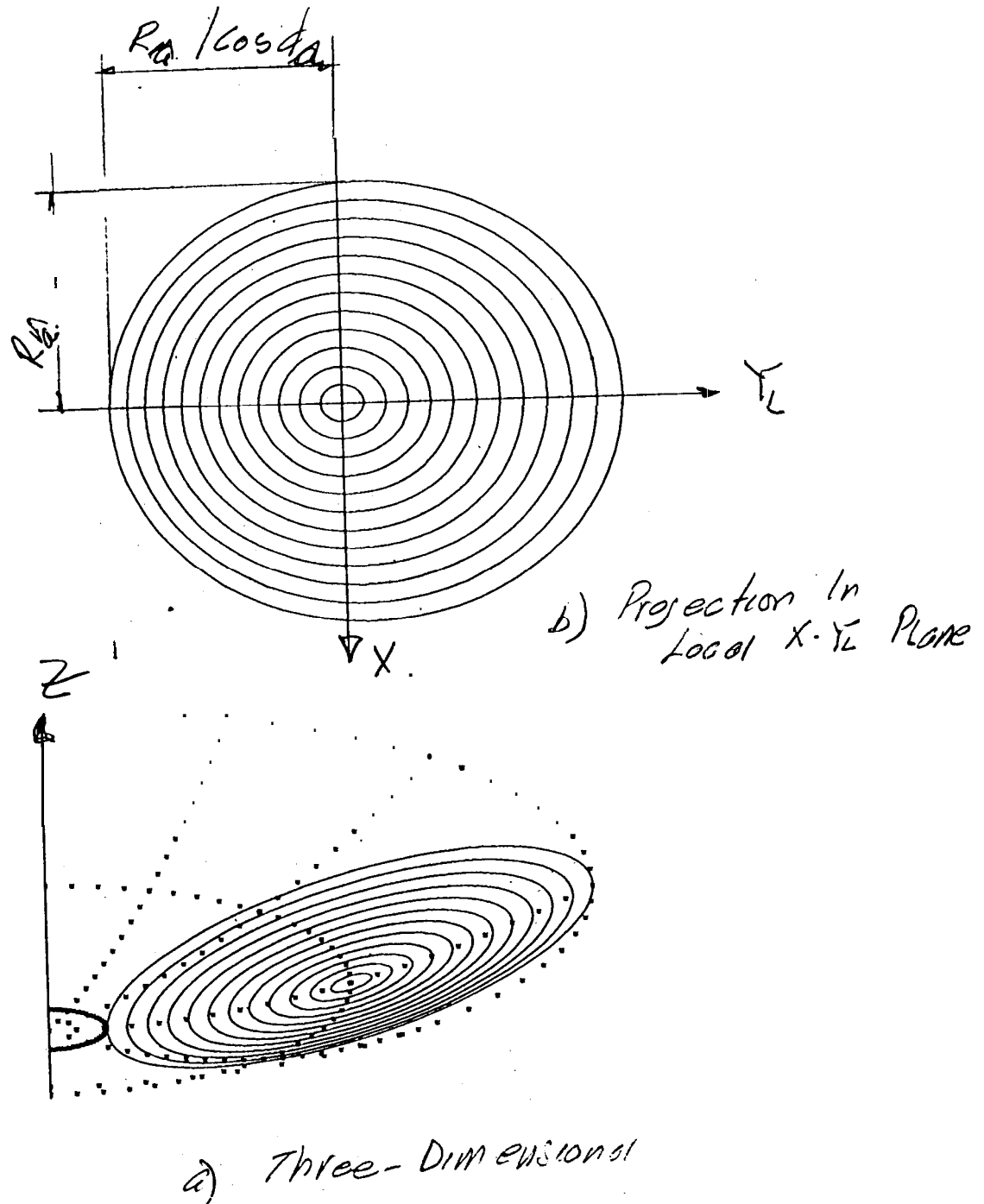


Figure 1-15 Offset Antenna View

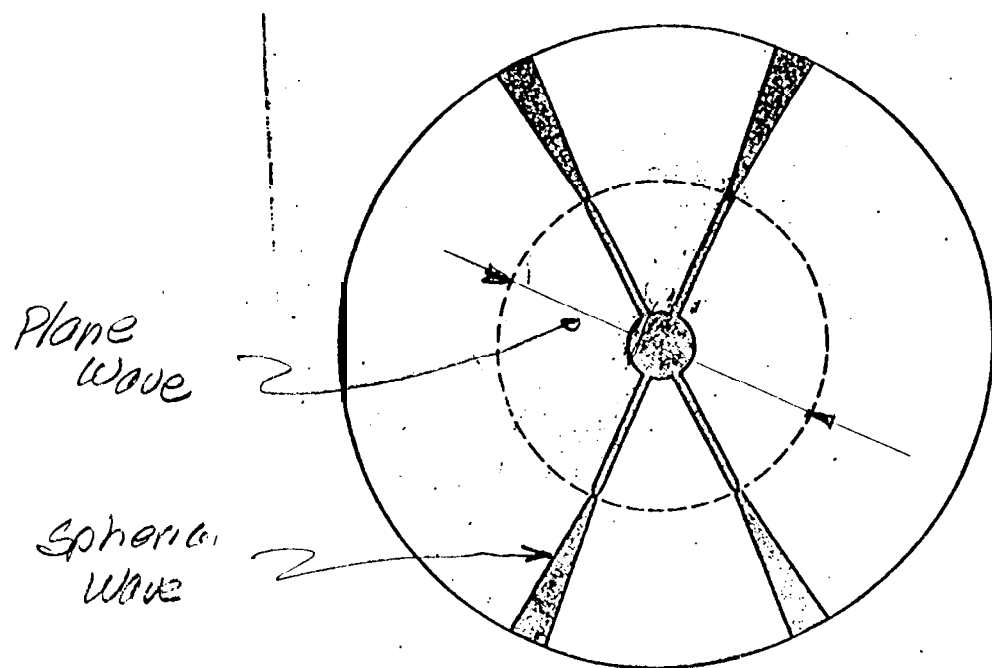


Figure 1-16
Plane and Spherical
Wave - Shadows

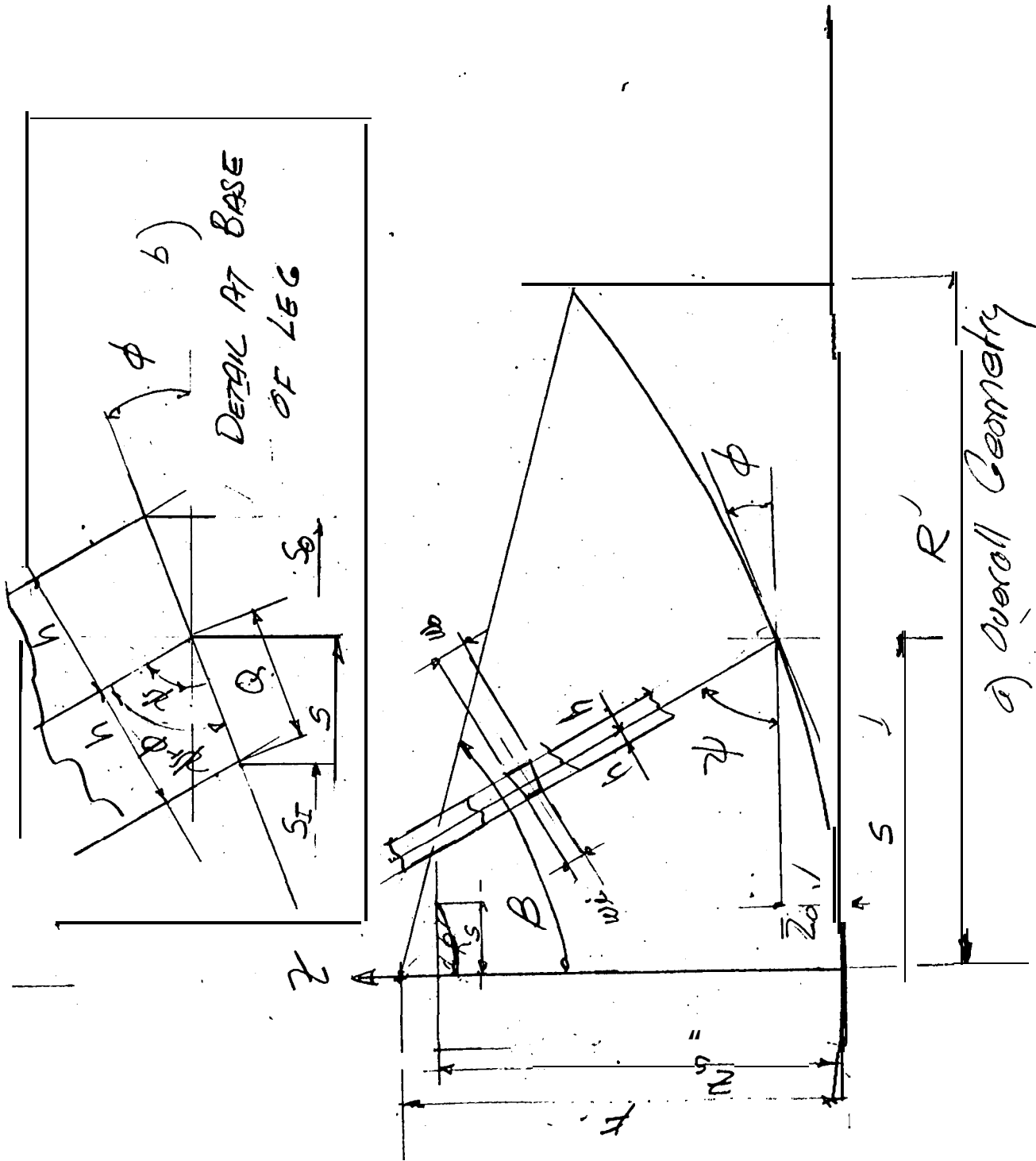
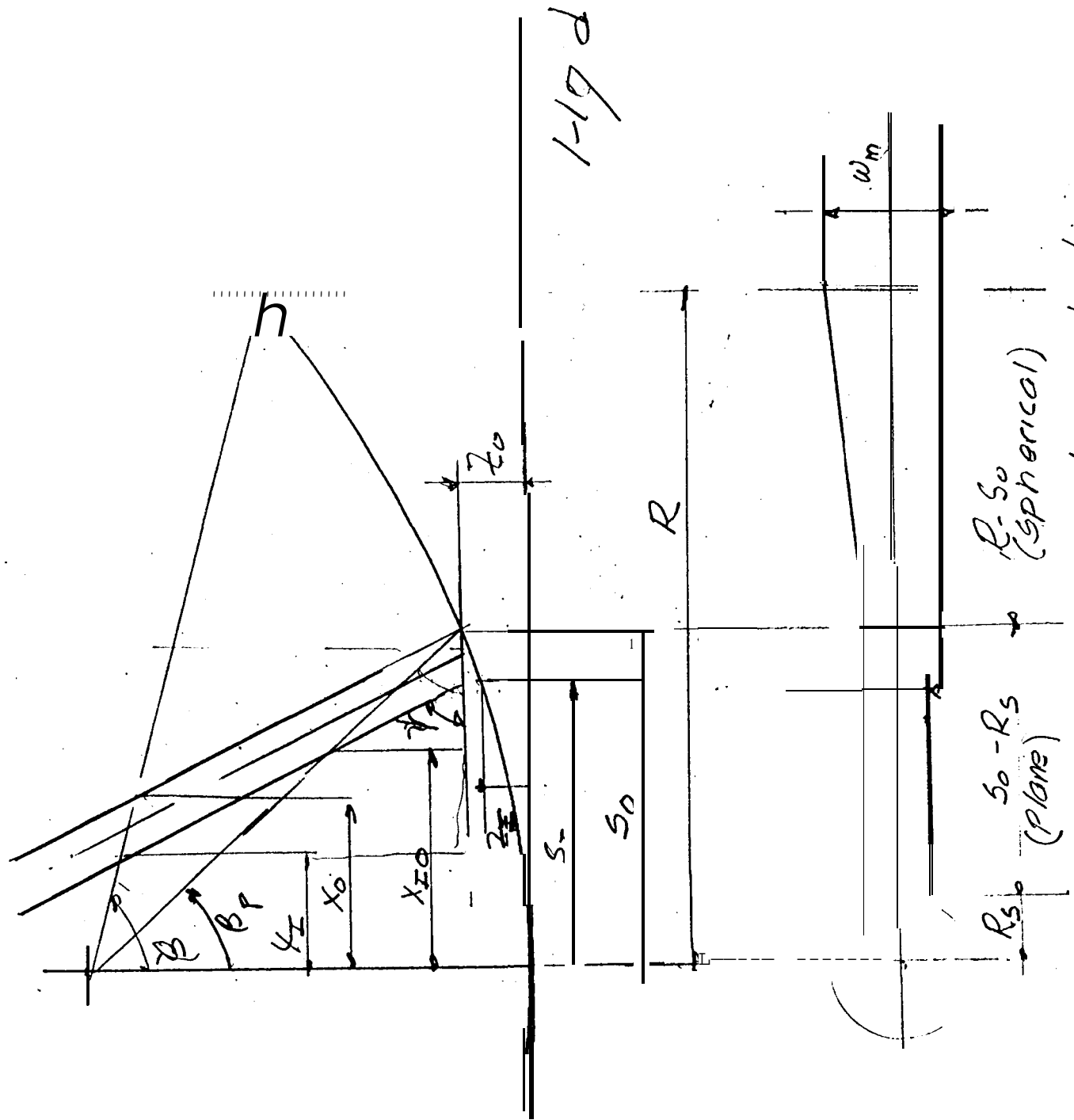
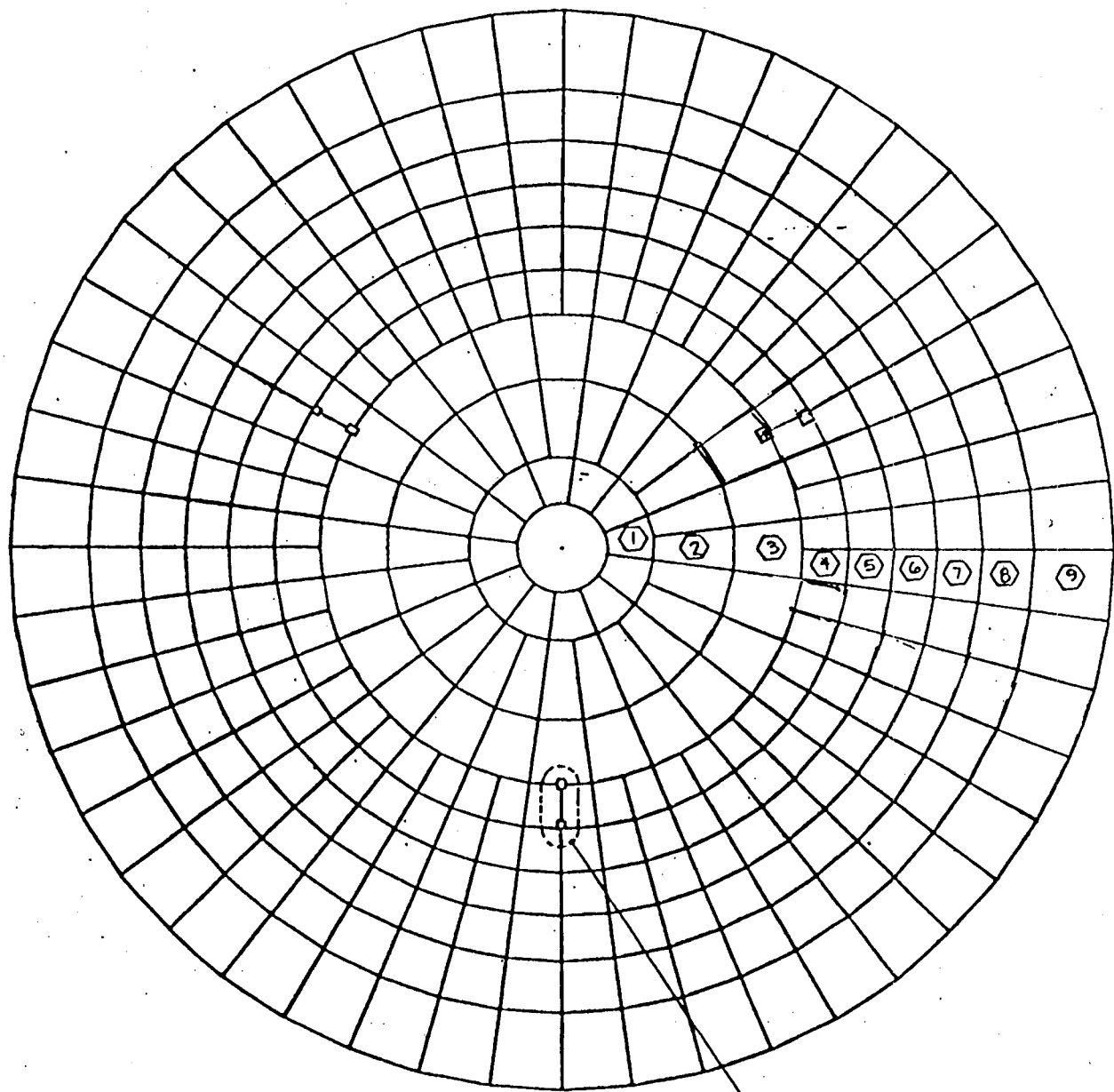


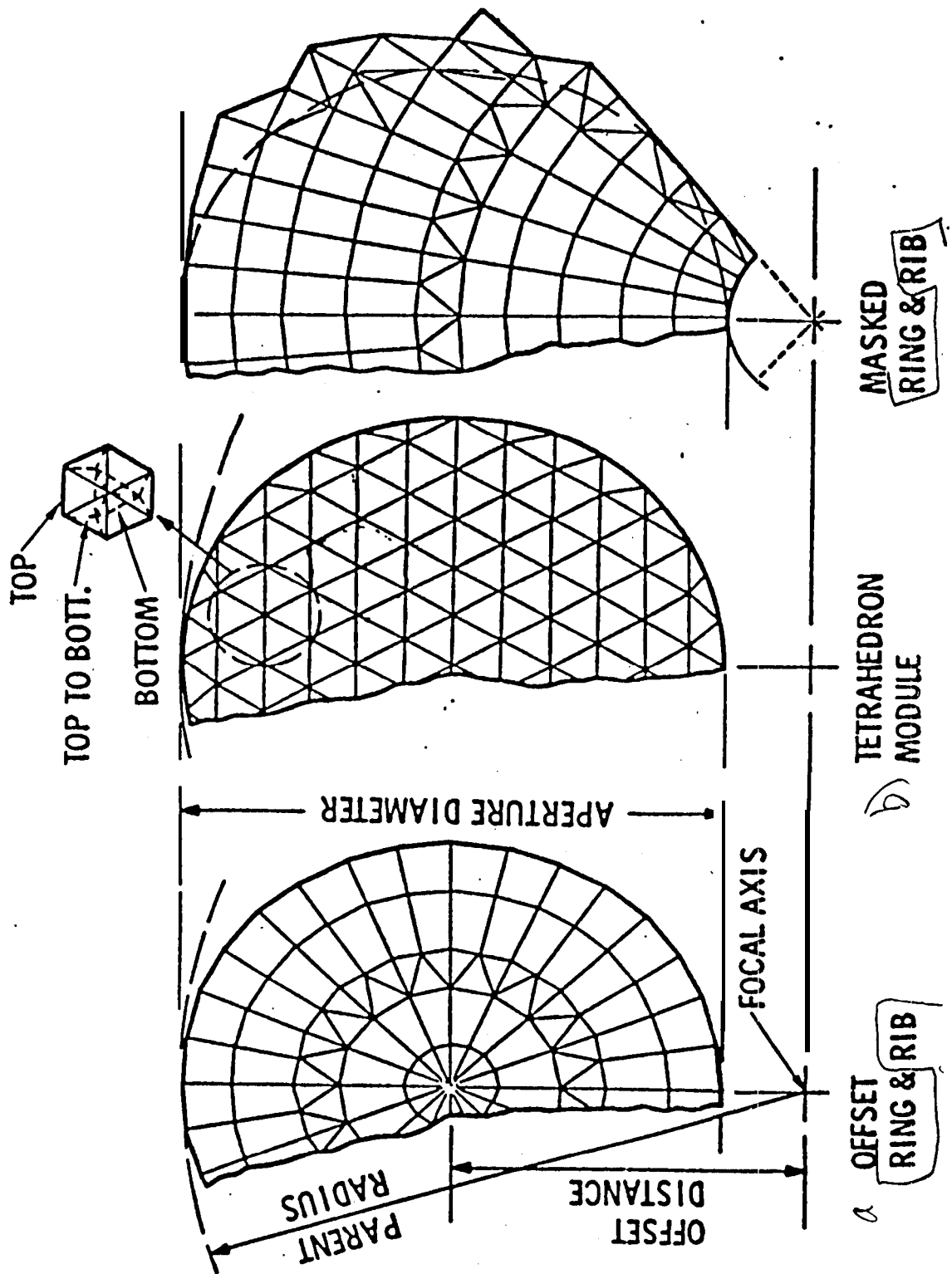
Figure 1-17
Aperture Blocking Geometry



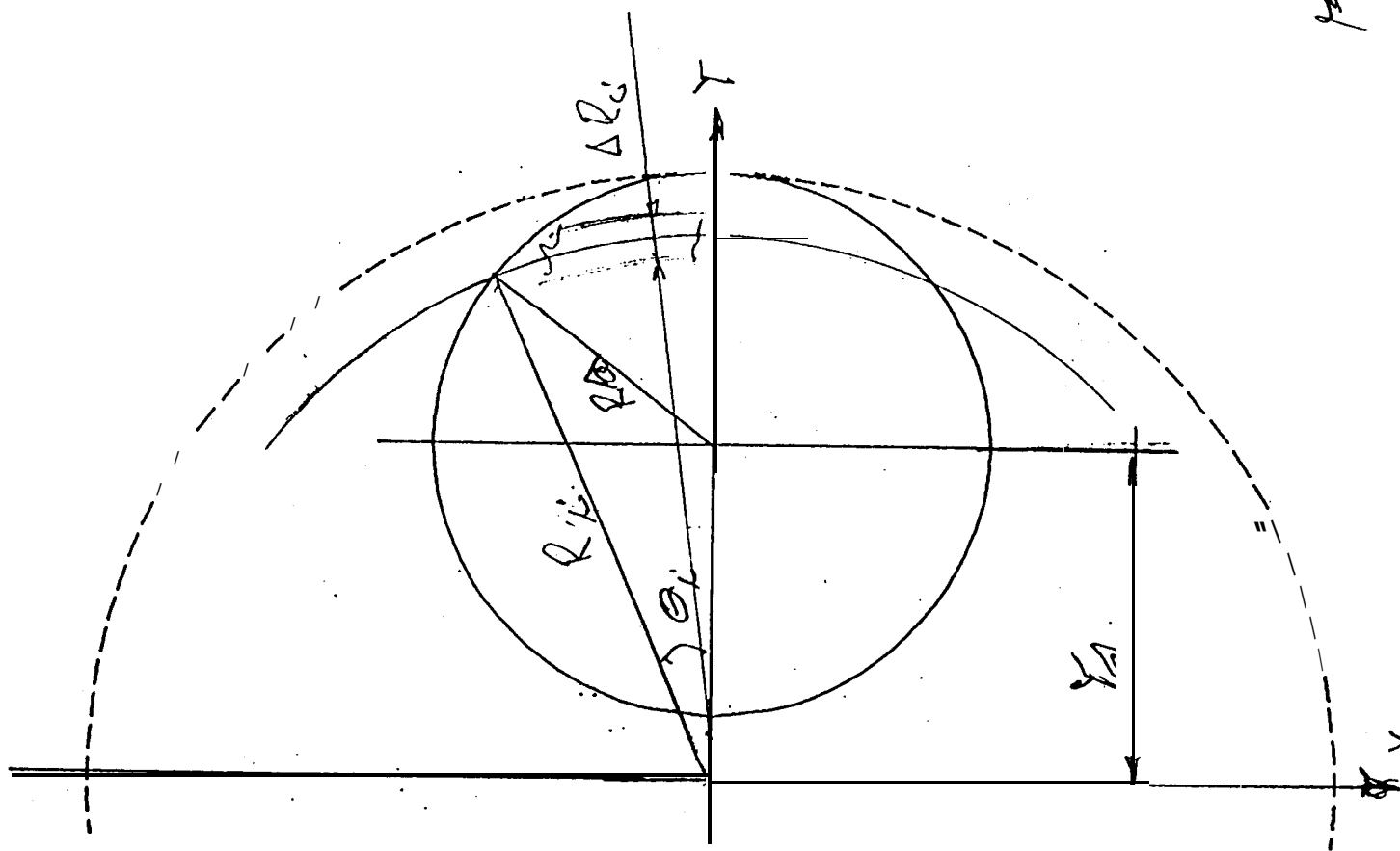
1. c) Leg shadows



TRIPOD GOT OUTS
9 PLACES, ...



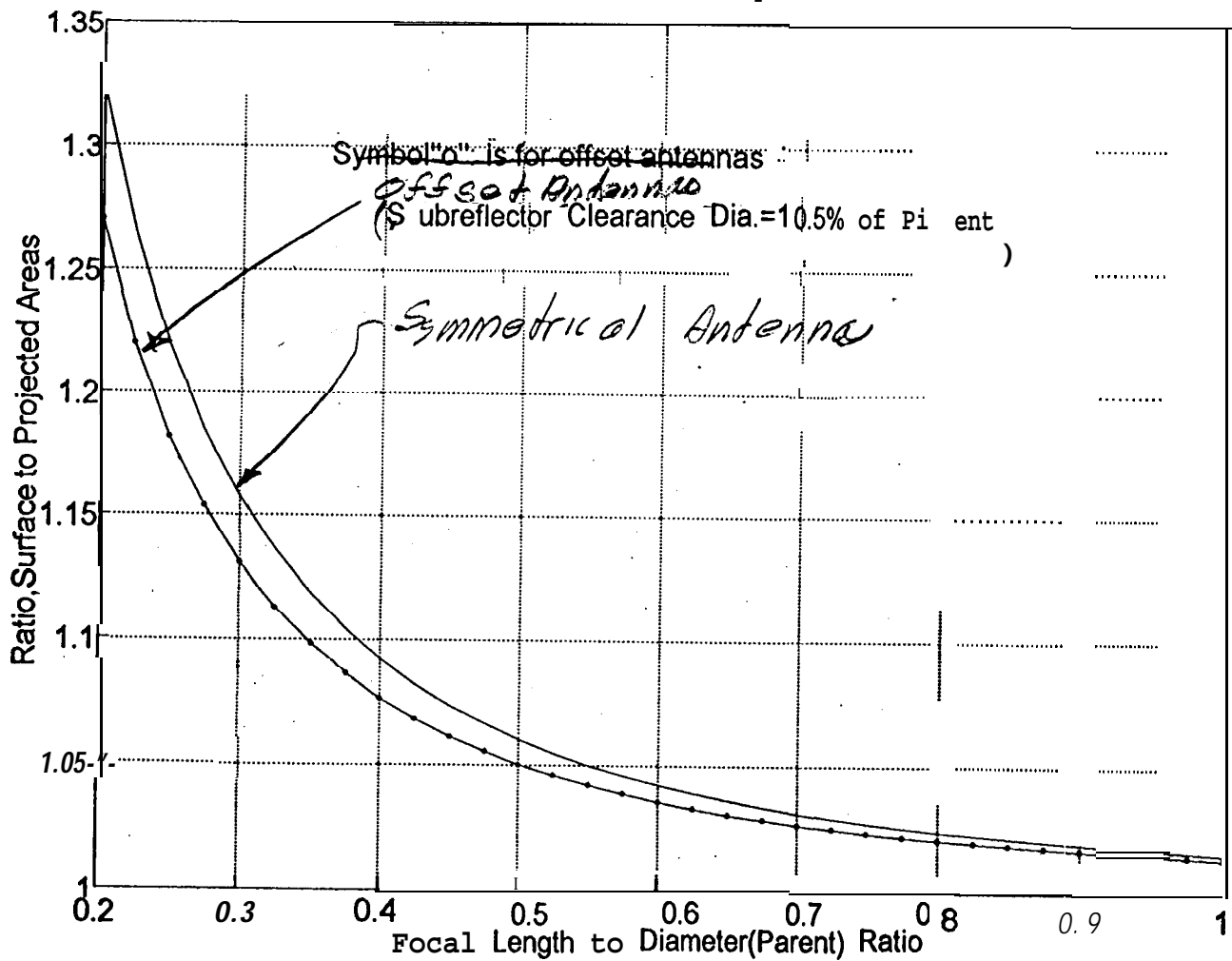
f 1-19
 OFFSET ANTENNA
 SURFACES AND STRUCTURE ARCHITECTURE



1-20

~~1-20~~

Parabolic Antennas: Surface to Aperture Areas vs F/D



Fig

1-21

SURFACE AREA FACTORS

APPENDIX 1-A

PROGRAM TO CALCULATE THE BLOCKED SHADOW

Figure 1-A shows a MATLAB program to calculate the blocked shadow. The total plane and spherical wave shadow areas and the relative proportions of each are provided. In addition, the user-furnished dimension Z_s is used to determine the clearances between the back edge of the subreflector and the inner support leg. A moderate acquaintance with any high-level coding language, such as FORTRAN, should make the code understandable, even with no prior exposure to the program; however, the following comments may be helpful:

- (1) The % symbol is interpreted as the beginning of a non-executable comment.
- (2) The program is case sensitive and almost all instructions and built-in functions require lower case.
- (3) In contrast to (2) above, all of our variables (including those of Figure 17) are represented in upper case (i.e. , WI represents w_i , TANBETA represents $\tan \beta$, PSI is ψ , and so forth.

The sample data built into the program, which the user is given the opportunity to replace, will result in a total shadow of 5.478 percent. The effect on the microwave antenna is more severe than the geometric aperture area reduction, perhaps by a factor of about two.

Appendix

1-A

```

%This is MATLAB\MISCPROBS\BLOCKING.M, Feb.10,1993
% compute blocking of subreflector and tripod or quadripod
% The following two functions are expected to be available to MATLAB:
%     function y=sine(x)           function y=cosine(x)
%     y=sin(x*pi/180) ;           y=cos(x*pi/180) ;

format compact
% Set some default values for 34M HEF antenna
NLEGS=4; PSI=61.3967; F=434; ZS=406.7;
R=669.3; RS=75. ; S=328; H=19.45; WI=9.5; Wo'=14.

disp('supply- NLEGS,PSI,F,ZS,R,RS,S,H,WI,WO, AND "return" ')
keyboard
Tanphi=S/2/F;
PHI=atan(Tanphi) *180./pi;
Q=H/sine(PSI+PHI)
SI=S-Q*cosine(PHI)
SO=S+Q*cosine (PHI)
ZI=SI*SI/4/F
ZO=SO*SO/4/F
ZMAX=R*R/4/F;
TANBETA=R/(F- ZMAX)
TANP=sine(PSI) /cosine(PSI)
DEN=1/TANBETA-TANP
XI=(F-ZI-SI*TANP)/DEN
XO=(F-ZO-SO*TANP) /DEN
TANBETAP=SO/ (F-ZO)
DENP=1/TANBETAP-TANP
XIO=(F-ZI-SI*TANP)/DENP
MAGI=R/XI
MAGO=R/XO
MAGIO=SO/XIO

WOPT=MAGIO*WI
AFACT=pi/144.
ASUB=RS*RS*AFACT %SQUARE FEET
AMAIN=R*R*AFACT
if WO>=WOPT
    ASPH=(R-SO)*WO* .5*(1+MAGO) ;
else
    ASPH=(R-SO)*WI* .5*(MAGIO+MAGI) ;
end
ASPH=ASPH*NLEGS/144
APLANE=WO*( SO-RS)*NLEGS/14 4
LEGSHAD=ASPH+APLANE
TOTSHAD=LEGSHAD+ASUB
TOTPCT=TOTSHAD/AMAIN* 100
LEGPCT=LEGSHAD/AMAIN* 100
% Blocking calculations completed above
% Now get leg-to-subreflector clearances
CLH=SI-(ZS-ZI)/TANP-RS % horizontal clearance
CLP=CLH*sine(PSI) % perpendicular to leg face clearance

```

APPENDIX 1-B

PROGRAM FOR AREA COMPUTATION

Figure 1-B is a MATLAB program to compute surface area factors for symmetrical and offset antennas. Although the notation is different, the formulation follows Eqs. [1.26 through 1.29], and there are also explanatory comments.

```

% Feb 16,1993 this is AREASOFF.M, surface area of offset paraboloid
format compact
% set some defaults
fed=.2:.05:1.0 % focal length to diameter ratio
sd=.105 % ratio, subreflector envelope to parent diameter
n=20 % number of increment to use for parent radius
disp('Supply"fod=a:b:c,sd= , n= ", or accept defaults, then "return"')
keyboard
rm=2/(1-sd);%radius of the parent, (aPerture radius is fixed at 1.0)
yo=rm-1; % offset to center of aperture
rmin=yo-1;rmax=yo+1;% rmax-rmin =2=aperture diam.
delr=2/n;
r=rmin+delr/2:delr:rmax-delr/2;
nf=length(fod);
f=fod*2*rm;% the set of focal lengths
cc=(r.^2 -1 +yo^2)./(r.*2*yo);
theta=acos(cc);
dela=2*r.*theta*delr;% vector of increments in projected aperture area
% the next few lines gets the factor for symmetric antennas
%creep up on the answer with fo, f1,f2,f3
fo=fod.^2; f1=(16*fo).^(-1); f2=1+f1; f3=f2.^1.5-1;
fsym=32/3*fo.*f3;
for j=1:nf
slopef=sqrt(1+(r./2/f(j)).^2 ); % 1/cos(surface slope)
asj(j)=sum(dela.*slopef);
foff(j)=asj(j)/pi;%ratio surface to aperture areas
end
disp('SUMMARY' )
disp('fsym,foff,are the ratios of surface to 'aperture areas')
disp('      fod      f      fsym      foff' )
[ fed'      f'      fsym'      foff' ]

```

Fig 1B

SURFACE ACCURACY	1
2.1 Antenna Gain and Efficiency	2
2.2 The Pathlength	2
2.3 Pathlength Error	3
2.3.1 <u>Computational Formula</u>	4
2.3.2 <u>Pathlength Error in Three Dimensions</u>	4
2.3.3 <u>parameters or Fitting</u>	4
2.3.4 <u>The Fitting Equation</u>	5
2.3.5 <u>Weighting Factors</u>	5
2.3.6 <u>Minimization of The Mean Squares</u>	5
2.4 Additional Notes	6
2.4.1 <u>Fitting Parameter Options</u>	6
2.4.2 <u>Reduction of the Mean Square Error from the Fit</u>	10
2.4.3 <u>Alternative Solution Method</u>	10
2.4.4 <u>Numbers of Surface Points to Include</u>	13

CHAPTER 2

SURFACE ACCURACY

Deviations from perfect geometrical accuracy of the reflecting surface have a major effect on the efficiency of the antenna system. Deformations of the structure are responsible for variations in the pathlengths of the microwave signals from the affected parts of the surface. These pathlength variations produce adverse errors in the phase characteristics of microwave signals.

The main reflector surface, which is usually parabolic or quasi-parabolic, is the most important contributor to surface inaccuracies because its large size makes it vulnerable to deflections. Consequently, this chapter concentrates on the geometry and deformations of the parabolic main reflector and how these effects are analyzed in terms of microwave pathlength errors. Nevertheless, there is hardly any difference in the analysis of deviations for any of the other subreflector surfaces.

Reflector surface analysis is based upon the geometry of optical ray tracing. These geometric relationships represent the first-order microwave effects adequately for all practical structural engineering analysis and design purposes. (More rigorous treatments, although not ordinarily needed for structural engineering, could be provided by the fields of diffraction analysis and physical optics). Optical ray tracing is a straightforward geometrical analysis that is capable of appropriately characterizing the efficiency of the structural surface using only two principles of optics: i.e., rays travel in straight lines, and the law of reflection (the angle of reflection at the surface equals the angle of incidence).

2.1 ANTENNA GAIN AND EFFICIENCY

Antenna gain is the ratio of the power transmitted by the antenna to the power of an ideal isotropic radiator. The gain of an ideal circular aperture antenna is concentrated in the boresight direction and is given numerically in terms of the diameter D and wavelength λ as

$$G_N = (\pi D / \lambda)^2 \quad [2.1]$$

A real antenna has an overall efficiency factor η_T of less than unity. In practice the numerical gain is replaced by the gain G in units of decibels (dB). Decibels are computed as ten times the common logarithm of the number. Consequently, the gain is

$$G=10 \log_{10} \eta_T (\pi D/\lambda)^2$$

[2.2]

The efficiency factor is the product of a chain of efficiency terms from a number of loss-contributing effects, each less than unity. Some of these effects are illumination, spillover, cross-polarization, leakage, aperture blocking, and surface efficiency (Ref. 2.1). Surface efficiency is the most significant of all of these and is a primary concern of the structural engineer. The magnitude is usually in the range of from 40% to 90%. The efficiency factor associated with the blocked surface area (Section 1.7) (primarily dictated by configuration rather than design) could be in the range of from 85% to 90%. The illumination efficiency could be as low as 85%, but can be improved significantly when the reflecting surface shapes are slightly perturbed ("shaped") with respect to the basic parabolic, hyperbolic, or elliptical surfaces. The other contributing efficiencies tend to be in the 95% to 99% range, so that they are individually much less significant. Our emphasis in this chapter will be on the reflector surface accuracy and efficiency, which to a large extent can be controlled by structural engineering because these factors are dependent upon the response of the structure to environmental loading.

It is fortunate that a simple, but sufficiently accurate, approximation exists to quantify reflector surface efficiency. The Ruze equation (Refs. 2.2 and 2.3) provides the efficiency η in terms of the wavelength λ and a readily calculated structural parameter, σ , which is the root mean square (rms) half-pathlength error. The Ruze equation is

$$\eta = \exp-(4\pi\sigma/\lambda)^2$$

[2.3]

Consequently, the reduction of gain due to the surface errors is

$$dB(\text{loss}) = 10 \log_{10} \eta = 10(\log_{10} e) \times (4\pi\sigma/\lambda)^2 = 4.3429 (4\pi\sigma/\lambda)^2 \quad [2.4]$$

The Ruze equation was derived originally for the assumptions that the surface errors have a Gaussian distribution, that they are uncorrelated outside of a region that is small in comparison with the reflector diameter, and that there are a sufficient number of terms in the computation of σ to make it statistically meaningful. The first two assumptions could be approximately satisfied by the random errors of manufacturing and field installation tolerances. However, when the surface errors are the result of structural deflections caused by the environmental loading, neither of these two assumptions are valid because structural deformations are correlated over long distances and have systematic deterministic (rather than random Gaussian) distributions. Nevertheless, the Ruze equation seems to hold in most practical cases despite violation of the assumptions. In

tests of surface deflection patterns caused by environmental loading, the validity of the equation has been verified to provide almost the same reduction in gain that was found by a much more comprehensive geometric theory of diffraction analysis. The third of the assumptions above presents no difficulties because the number of terms logically chosen for analysis usually will readily meet the statistical requirements.

The Ruze equation can be used to establish a term called the "gain limit" for an antenna of given diameter and pathlength error. At the gain limit the increase of gain (Eq. [2.1]) for an increase in operating frequency (e.g., reduction in wavelength) is offset by the loss of efficiency (Eq. [2.4]) for the smaller wavelength that accompanies the frequency increase. It can be shown that the half-pathlength error at the gain limit. is

$$\sigma = \lambda/4\pi \quad [2.5]$$

The surface efficiency at the gain limit is only 37% and the associated gain reduction is 4.3 dB. This value of the pathlength error is sometimes considered to be a practical upper limit of usefulness for a given antenna and frequency.

2.2 THE PATHLENGTH

Figure 2-1 shows a section through a radial plane of a Cassegrain antenna. This is a projection in the R-Z plane in which R is the radial coordinate axis and Z is the focal axis. An incident ray parallel to the focal (Z) axis at radius r crosses the focal plane at point 1 and is reflected at the surface at point 2. The reflected ray travels towards the focal point until it impinges on the subreflector at point 3. A subsequent reflection brings the ray to the feed at point 4. (The notations F, c, and a are the same as in Eqs. [1.5] and [1.6].)

The vector tangent to the surface at r is t and θ is the slope of the tangent. The normal to the surface is n and θ is also the angle between the normal and the incident and the reflected rays; $\beta (= 2\theta)$ is the full angle between incident and reflected rays. Point 2, with coordinates (r,z), is the point of incidence on the main reflector.

By differentiating Eq. [1.5a), we find

$$\tan \theta = r/2F \quad [2.6]$$

Also, by inspection of Figure 2-1

$$\tan \beta = r/ (F-z) \quad [2.7]$$

and the hypotenuse of the triangle 1-2-5 can be shown to be $F+z$. Consequently, if this was a focal point antenna (with a feed at the focus instead of a subreflector) the pathlength from focal plane to the surface to the focal point would be $(F-z) + (F+z) = 2F$. A simpler way to arrive at this is to consider a central incident ray along the focal axis ($r = 0$). It is clear that incident and reflected rays would travel the path distances of F from the focal plane to the surface and again back to the focal point. The pathlength from focal plane to feed for a Cassegrain antenna with a subreflector is also most easily found by considering a central ray. By adding the paths 1-2, 2-3, and 3-4 of the figure, this focal plane to focal point path is $2(F+a)$. It could be shown that the pathlength is also the same for any other incident ray parallel to the focal axis.

The important feature of the parabolic reflector is that the pathlength, either for focal feed or Cassegrain system, is independent of the radius to the incident ray. That is, the pathlength for an ideal geometric surface is a constant for any point of the surface. In determining the surface accuracy our prime interest is the change in this pathlength due to surface deformations. This change, which affects the microwave phase, is considered next.

2.3 PATHLENGTH ERROR

2.3.1 Computational Formula

Figure 2-2 shows an enlarged view of the region in the vicinity of point 2 of Figure 2-1. Now, however, a vector d that represents the deformation from the ideal surface has been added. This vector is the result of a change in surface shape due to any cause, such as external environmental loading, or fabrication, or alignment errors. It is convenient to consider a deformation from a point 6 of the original surface chosen so that d extends from point 6 and terminates at point 7, which is on the path of the original ray reflected from point 2 to the focal point. There is no loss of generality in this because every deformation vector will always terminate at a ray that extends from some originally undeformed surface point towards the focal point, or possibly at an extension of that ray below the surface.

The deformation has been greatly exaggerated in this figure; deformations are ordinarily so small relative to the scale of the original surface that the geometry in this region can be simplified with negligible error. This allows the analysis to replace surfaces in a small region by the tangents to the surfaces. The result is that the surface from point 6 to point 2 is replaced by the tangent plane at point 2. Furthermore the tangent at points 2 and 6 can be taken as the same.

It can be seen from the figure that the sum of the distances

from point 2 to point 8 and point 2 to point 7 is the difference in path from focal plane to focal point for an incident ray that crosses the focal plane at point 1 and the path of a ray that crosses the focal plane at point 9. These two distances are also dimensioned in the figure as s and p .

In the figure, the distance from point 2 to point 10 is the projection of the deformation vector on the normal to the surface vector and, from vector algebra, is equal to the dot(inner) product of the deformation vector with a unit normal n . The distance s is this dot product divided by the cosine of θ . That is,

$$s = d \cdot n / \cos \theta \quad [2.8]$$

and, from the figure, the distance p is

$$p = s \cos \beta = s \cos 2\theta \quad [2.9]$$

or using a trigonometric identity,

$$p = s (2 \cos^2 \theta - 1) \quad [2.10]$$

so that the pathlength error is

$$s + p = 2d \cdot n \cos \theta \quad [2.11]$$

Finally, we have an important equation that is used to compute ρ , the half-pathlength error at a particular point on the surface,

$$\rho = d \cdot n \cos \theta \quad [2.12]$$

In words: The half-pathlength error is the normal component of the deformation vector times the direction cosine with respect to the focal axis. Sometimes the half-pathlength error is referred to as the axial component of the normal error, which with proper interpretation is equivalent to the previous description. Equation [2.12], which was developed for a parabolic main reflector, can be used to compute the half-pathlength error for any deformed surface in terms of the normal to that surface and the associated direction cosine. It is common practice to refer to the half pathlength error more simply as the "pathlength error" and to drop the prefix "half". Following common practice, the remainder of this text will also imply that the half pathlength error is intended even though the prefix "half" may or may not be included.

2.3.2 Pathlength Error In Three Dimensions

It is necessary to generalize the pathlength error computation to the three-dimensional space of an antenna surface. In particular the pathlength error is computed at a discrete set of points distributed over the surface. These points provide a sampling of the surface for computation of the rms error in the Ruze equation (Eq. [2.3]). The set of points typically consists of the nodes nearest the surface in the analytical model of the structure. This set is usually closely equivalent to points at the corners of the surface panels.

Equation [2.12] can be rewritten to provide the half-pathlength error at a particular point i as

$$P_i = (\gamma_z \, dn)_i \quad [2.13]$$

in which γ_z is the direction cosine at point i with respect to the focal (Z) axis and dn is the projection ($\mathbf{d} \cdot \mathbf{n}$) of the deformation vector on the surface normal at point i . That is, dn is the normal component of the deformation vector.

In three-dimensional Cartesian space we will take the X and Y axes to be in the aperture plane and the Z -axis positive in the direction of the focal point. This is consistent with the definition of the coordinate system given in Section 1.6.3. The radial coordinate r of Figure 2-1 will be replaced by its x and y (Pythagorean Theorem) components. Furthermore, although the subscript i is typically omitted for convenience, the following discussion refers to some particular point i with coordinates (x_i, y_i, z_i) .

By extending Eq. [1.5a] from a curve to a surface of revolution, the equation of the parabolic surface $G(x, y, z)$ becomes

$$G(x, y, z) = Z - (x^2 + y^2)/4F = 0 \quad [2.14]$$

To find a unit normal to the surface, we first find the gradient ∇G , which is a vector normal to the surface and positive towards the focal point. Thus from Eq. [2.14] we have

$$\nabla G = [-2x/4F \quad -2y/4F \quad 1] \quad [2.15]$$

in which the components are ordered parallel to the X , Y , and Z axes, respectively. The unit normal vector is obtained by normalizing the gradient by its length. This provides the components of a unit normal to the parabolic surface as

$$\mathbf{n} = \nabla G / |\nabla G| = [-x \quad -y \quad 2F]/T \quad [2.16]$$

in which

$$T = (X^2 + Y^2 + 4F^2)^{1/2} \quad [2.17]$$

The unit normal is often expressed in terms of its direction cosines with respect to the coordinate axes. That is,

$$n = [\gamma_x \ \gamma_y \ \gamma_z] \quad [2.18]$$

Therefore, matching Eqs. [2.17] and [2.18] provides

$$\gamma_x = -x/T \quad [2.19a]$$

$$\gamma_y = -y/T \quad [2.19b]$$

$$\gamma_z = 2F/T \quad [2.19c]$$

The deformation vector in a Cartesian coordinate system is

$$d = [u \ v \ w] \quad [2.20]$$

in which u , v , w , are the components of the deflection vector at the point in the X , Y , and Z directions. Therefore, for Eq. [2.13],

$$dn = d \cdot n = (\gamma_x u + \gamma_y v + \gamma_z w) \quad [2.21]$$

Then substituting in Eq. 2.13, we have the half-pathlength error ρ_i at the point i in terms of the coordinates of the point

$$\rho_i = \frac{2F(-xu - yv + 2Fw)_i}{(T^2)} \quad [2.22]$$

or in terms of direction cosines

$$\rho_i = (\gamma_z \gamma_x u + \gamma_z \gamma_y v + \gamma_z \gamma_z w)_i \quad [2.23]$$

2.3.3 parameters For Fitting

It is not necessary to compute the pathlength error in terms of the original surface equation, but it is permissible (and advisable) to compute the pathlength error from an alternative surface that best-fits the deformed surface. The important effect on the microwave system is the phase error distribution over the surface. Specifically, if the original parabolic surface deformed into another parabolic surface, all rays from the second surface would have the same new overall pathlength. Since these rays would arrive at the feed with a constant phase there would be no adverse microwave effect. Therefore the approach is to compute pathlength errors as the residual errors with respect to an alternative new parabolic

surface that best fits the deformation data.

The alternative surface is defined in terms of five parameters that constitute a rigid body motion and an additional parameter that is related to a change in the original focal length. Nevertheless, it is necessary for the position of the subreflector for a dual reflector system, or for the position of the feed for a focal feed reflector, to be movable. This would allow compatibility variations in the microwave path geometry established by the fitting parameters. Typical antennas actually do have provisions for providing these necessary motions.

The five parameters (Ref. 2.4) are indicated in Figure 2-3. They consist of three translations, U_0 , V_0 , and W_0 , parallel to the X, Y, and Z coordinate axes, and rotations θ_x and θ_y about the respective axes. One more parameter is related to the new focal length F_0 . Reference 2.6 describes a widely distributed FORTRAN program to compute the best fit surface and residual pathlength error. A focal change parameter k was defined in this reference in terms of the focal length of the new parabola F and the original focal length F as follows:

$$k = (F_0/F - 1) \quad [2.24]$$

In Ref. 2.5 the six parameters were called the "homology parameters" because they represent a transformation from the original parabolic surface to an alternative parabolic surface.

2.3.4 The Fitting Equation

The three translation parameters produce the following changes in the original displacements with respect to the new surface:

$$\Delta u = -U_0 \quad [2.25a]$$

$$\Delta v = -V_0 \quad [2.25b]$$

$$\Delta w = -W_0 \quad [2.25c]$$

The parameter k , which was taken in Ref. 2.6 as the fourth parameter, produces

$$\Delta w = -kz \quad [2.26]$$

The structural deformations are always small for any reasonable antenna structure so that the best-fitting surface will differ very little from the original. In particular the magnitudes of the rotations are small enough to allow the sines

of rotation angles to be replaced by the angles and the cosines to be replaced by unity. Consequently, the rotation parameters θ_x and θ_y additionally affect the u , v , w , components as follows:

$$A u = -z \theta_y \quad [2.27a]$$

$$A v = z \theta_x \quad [2.27b]$$

$$A w = -y \theta_x + x \theta_y \quad [2.27c] \quad .$$

Combining Eqs. [2.25), [2.26), and [2.27] we have

$$\begin{array}{l} A u = \\ A v = \\ A w = \end{array} \left\{ \begin{array}{cccccc} -1 & 0 & 0 & 0 & 0 & -z \\ 0 & -1 & 0 & 0 & z & 0 \\ 0 & 0 & -1 & -z & -y & x \end{array} \right\} \left(\begin{array}{c} U_0 \\ V_0 \\ W_0 \\ k \\ \theta_x \\ \theta_y \end{array} \right) \quad [2.28]$$

Equation 2.28 can be written for any particular node i as

$$A u v w_i = c_i H \quad [2.29]$$

in which $A u v w$ is the triad on the left-hand side of Eq. [2.28], c_i on the right hand side is the 3-by-6 coefficient matrix on the right-hand side, and H is the vector of fitting parameters on the right-hand side. The equation relates the change in deformation coefficients at node i to the coefficient matrix for that node and the fitting parameters for all nodes.

With omission of the subscripts, Eq. [2.23] can be written for this node in matrix form as

$$p = a u \quad [2.30]$$

in which

$$a = [\gamma_z \gamma_x \quad \gamma_z \gamma_y \quad \gamma_z \gamma_z] \quad [2.31]$$

and

$$u = \begin{pmatrix} u \\ v \\ w \end{pmatrix} \quad [2.31]$$

Consequently, after fitting we have

$$p(\text{fit}) = a(u + \Delta uvw) \quad [2.32]$$

or

$$\rho(\text{fit}) = a u + b H \quad [2.33]$$

where

$$b = a c$$

For reference, the row-column order of the matrices just defined are summarized in the table below:

<u>Matrix</u>	<u>Order</u>
H	6 x 1
u	3 X 1
a	1 x 3
c	3 x 6
b	1 x 6

Now it is possible to expand Eq. [2.33] to include the half-pathlength error vector p (after fitting) for all of the nodes of the surface as

$$p = A U + B H \quad [2.35]$$

In the above if there are N nodes in the surface, p is an N-by-1 row of half-pathlength errors, A is an N-by-3N matrix in which the a vectors are contained in the rows, beginning in column 1 in the first row, column 4 in the second row, column 7 in the third row, and in column 3j-2 in the jth row; U is a 3N-by-1 vector containing the u vector triads in the order of the associated nodes, B is an N-by-6 matrix that contains the associated b vector in each of its rows, and H is the same as in Eq. [2.28].

2.3.5 Weighting Factors

At this point it would be possible to solve a least squares problem to find H and then find the mean square pathlength error (the mean of the squares of the components of the pathlength error vector). This would not be strictly accurate because the nodes do not have equal microwave importance. It is more appropriate to compute a weighted rms error. To do this, the weighting factors for each node can be based upon two factors: one is a microwave illumination factor (a function of feedhorn design), the other depends upon the aperture area tributary to the particular surface node.

When the panels are arranged in a circular pattern, as in

Figure 1-18, it is straightforward to compute the area weighting factors in terms of the central angle and mid-radii of the adjacent panel rings. It may also be instructive to normalize the area weighting factors so that they sum to N. In this manner a weighting factor of unity applies to a node associated with the average aperture area. These area weighting factors can also be used in the computation of environmental loading that depends upon the reflector area, such as from panel weight or wind forces.

Illumination factors are given in a variety of ways as functions of a radius ξ that has been normalized to unity. An example illumination factor is

$$f(g) = 0.3 + 0.7(1-\xi^2) \quad [2.36]$$

At the rim, ($\xi = 1$) the illumination factor is 0.3. The attenuation in decibels would be about 10 dB (since this is an amplitude factor, rather than a factor on antenna power, decibels are computed as 20 times the logarithm). Consequently, the feed that produces this illumination would be called a "10-dB horn."

In many of the more modern antennas, the main reflector is a "shaped" parabolic surface. The shaping consists of a very small perturbation of the surface from a parabolic curve. As an example, the maximum departure from a parabolic curve for a 34-m antenna would be on the order of less than 20 mm. The purpose of shaping is to provide an illumination factor of close to unity for most of the surface; therefore the weighting factors for shaped antennas could be based upon only the area that is tributary to the nodes. In any case the weighting factors can be assembled in a diagonal matrix W where the entries correspond to the nodes associated with the pathlength error vector.

By including the nodal weighting factors, the mean square pathlength error, MSE, is given by

$$MSE = \rho^T W \rho / \sum w_i \quad [2.37]$$

where $\sum w_i$ is the sum of the weighting factors.

It has been found in a number of tests that the rms error is not strongly sensitive to the weighting factor. Many times a weighting factor of unity at the interior nodes, and one-half at the rim nodes, produces a result similar to that of more precisely computed weights.

2.3.6 Minimization of the Mean Square

The conventional least squares method to find H to

minimize the weighted mean square half-pathlength error is equivalent to pre-multiplying the right-hand side of Eq. [2.35] by $B^t W$ and setting this to zero. This provides the usual least squares "normal equations"

$$B^t W A U + B^t W B H = 0 \quad [2.38]$$

Equation [2.38] can readily be solved for H by a number of software programs. The coefficient matrix $B^t W B$ is usually of full rank and well conditioned and the order is at most only 6.

Once H has been computed, the best-fit (half)pathlength error vector can be found from Eq. [2.33] and the mean square error can be found from Eq. [2.37). The square root of the mean square error is σ , which then can be used in the Ruze equation to compute the efficiency or gain reduction (Eqs. [2.3-2.4]).

The foregoing solution was described in terms of a matrix formulation to simplify the presentation. In practice the solution code performs the summations indicated by the matrix operations without explicitly forming the matrices. For example, the diagonal weighting matrix W could be replaced by a vector consisting of its diagonal elements and all the operations could be done in terms of this vector. This is favorable both for numerical computations and computer storage. A MATLAB program to compute the best-fit rms pathlength error as described here is included in Appendix 2-A.

2.4 ADDITIONAL NOTES

2.4.1 Alternative Fitting Parameter Combinations

When the structure and loading are symmetrical about the $Y Z$ plane, the finite element model that provides the deformation vector U is often condensed and assembled to represent only one side of the structure, such as the side in the first and fourth quadrants. In this case the first and sixth fitting parameters (X_0 and θ_y) should be suppressed. This is dealt with by replacing the first and sixth rows and columns of the matrices in Eq. [2.38] by zeros and then inserting unity in "the first and sixth diagonal entries of the coefficient matrix. If it is appropriate to suppress any of the other fitting parameters, this can be done in a similar way.

If parameter suppression produces a non zero mean pathlength error the mean should be subtracted from each term of the pathlength vector. That is, any constant term should be removed because it does not affect the microwave phase. Consequently, it is reasonable to conclude that "rms" error is actually a misnomer and should be replaced by "standard deviation."

2.4.2 Reduction of the Mean Square Error from the Fit

Best fitting of the pathlength error almost always produces a major reduction of the mean square error, perhaps by one or more orders of magnitude. The change in the mean square pathlength error as well as the effect of each of the individual terms in the fitting vector can be readily developed. For example, H is obtained by solving the following set of linear equations:

$$(B^t W B)H = -(B^t W A U) \quad [2.39]$$

where the coefficient matrix and the "right-hand side" are readily identified. With a little bit of algebra that involves substituting H as found from the equation above in Eq. [2.35] and by computing the weighted best-fit mean square pathlength error and subtracting the weighted mean square (raw) pathlength error before fitting, it will be found that the change in the mean square ΔMSE is

$$\Delta MSE = H^t (B^t W A U) \quad [2.40]$$

That is, the change(reduction) in mean square pathlength error is the dot product of the solution vector and the right-hand side vector used in the solution. Consequently, each of the six individual terms in the dot product summation can be examined to assess the contribution of the particular fitting parameter to the reduction in mean square error.

2.4.3 Alternative Solution Method

As an alternative to forming and solving the normal equations, it is possible to condense the procedure when software is available to solve the least squares problem by operating directly on a rectangular (not square) coefficient matrix. To accomplish this we ask for a solution to the system

$$B H = -p \text{ (raw)} \quad [2.41.]$$

Equation [2.41] follows from Eqs. [2.30] and [2.33]. The weighting factors can be included by premultiplying both sides of Eq. [2.41] by the square root of the weighting matrix. The MATLAB instruction to develop H is

$$H = WB \backslash WR \quad [2.42]$$

where

$$WB = W^{1/2} B$$

and

$$WR = -W^{1/2}\rho \text{ (raw)}$$

2.4.4 Numbers of Surface Points to Include

One of the assumptions in the Ruze equation is that there are a statistically sufficient number of points in the mean square pathlength error calculation. Ordinarily the calculations include all the surface nodes of the analytical model of the structure, which is approximately equivalent to the numbers of surface panel corners, which is also approximately the number of panels. Although a statistical analysis will not be undertaken to determine the sufficient number of points, the results of a simulation will be described. This will show that not too many points are needed to obtain reasonable results.

The simulation was based upon the 34-m antenna for which the panel layout was shown in Figure 1-18. There are 528 nodes in the top surface of the antenna. The procedure was to select fractional subsets of this number of nodes at random and to compute the pathlength errors for each subset for one particular case of external loading. The fractions selected produced approximately 1/2, 1/4, 1/8, 1/16, and 1/32 of the original nodes. The original weighting factors were always retained for the selected nodes. The tabulations below show the normalized rms best-fit pathlength error, the normalized value of the maximum fitting parameter (in this case it was always W_0), and the numbers of nodes in the subset.

RMS Pathlength	1.000	0.978	0.964	1.000	0.906	0.827
Maximum Parameter	1.000	0.997	1.000	0.991	1.020	1.026
Number of Nodes	528	266	130	66	34	15

It can be seen that there was not any significant difference in the pathlength error until more than 90% of the nodes were deleted. The maximum fitting parameter was even less sensitive to the number of nodes. On the one hand, there are no computational difficulties that would make it important to process less than all of the nodes, at least on paper. On the other hand, when in the field, and especially when in the process of taking theodolite measurements of the nodes, it is reassuring to know that the imposition of a truncated set of nodes need not introduce a major error.

REFERENCES

- 2.1. Bathker, D. A. , Microwave Performance Characterizations of Large Space Antennas, JPL Publication 77-21, Jet Propulsion Laboratory, California Institute of Technology, Pasadena, CA, May 15, 1977.
- 2.2. Ruze, J. , "The effect of aperture errors on the antenna radiation pattern," Supplemento del Nuovo Cimento, vol. 9, no. 3, pp 364-380, 1952.
- 2.3. Ruze, J., "Antenna Tolerance Theory--A Review," Proc IEEE, v. 54, 633-640, April 1966.
- 2.4. Barondess, S. M., and Utku, S., Computation of Weighted Root Mean Square of Path Length Changes Caused by the Deformations and Imperfections of Rotational Paraboloidal Antennas, Technical Memorandum No. 33-118, Jet propulsion Laboratory, California Institute of Technology, Pasadena, CA, March 1, 1963.
- 2.5. von Hoerner, S. , "Homologous Deformations of Tiltible Telescopes," J of the Structural Division. Proceedings of the ASCE, V. 93a no. ST5, October 1967.
- 2.6. Katow, M. S. , and Schmele, L. , "Utku/Schmele Paraboloid RMS Best-Fit Program," in Ludwig, A., ed., Computer Programs for Antenna Feed System Design and Analysis, Vol. 1: Programs and Sample Cases, Technical Report No. 32-979, Jet Propulsion Laboratory, California Institute of Technology, Pasadena, CA, 75-82, April 15, 1967.
- 2.7. Rochblatt, D. J., A User Manual. Data Processing Software for Microwave Antenna Holography: Computer Programs for Diagnostics, Analysis, and Performance Improvement of Large Reflector and Beamwaveguide Antennas, JPL D-10237, Jet Propulsion Laboratory, California Institute of Technology, Pasadena, CA, January 15, 1993.

FIGURES

2-1* Microwave Pathlength

2-2. Surface Deformation

2-3. Fitting Parameters

A2-1. MATLAB Pathlength Error Program

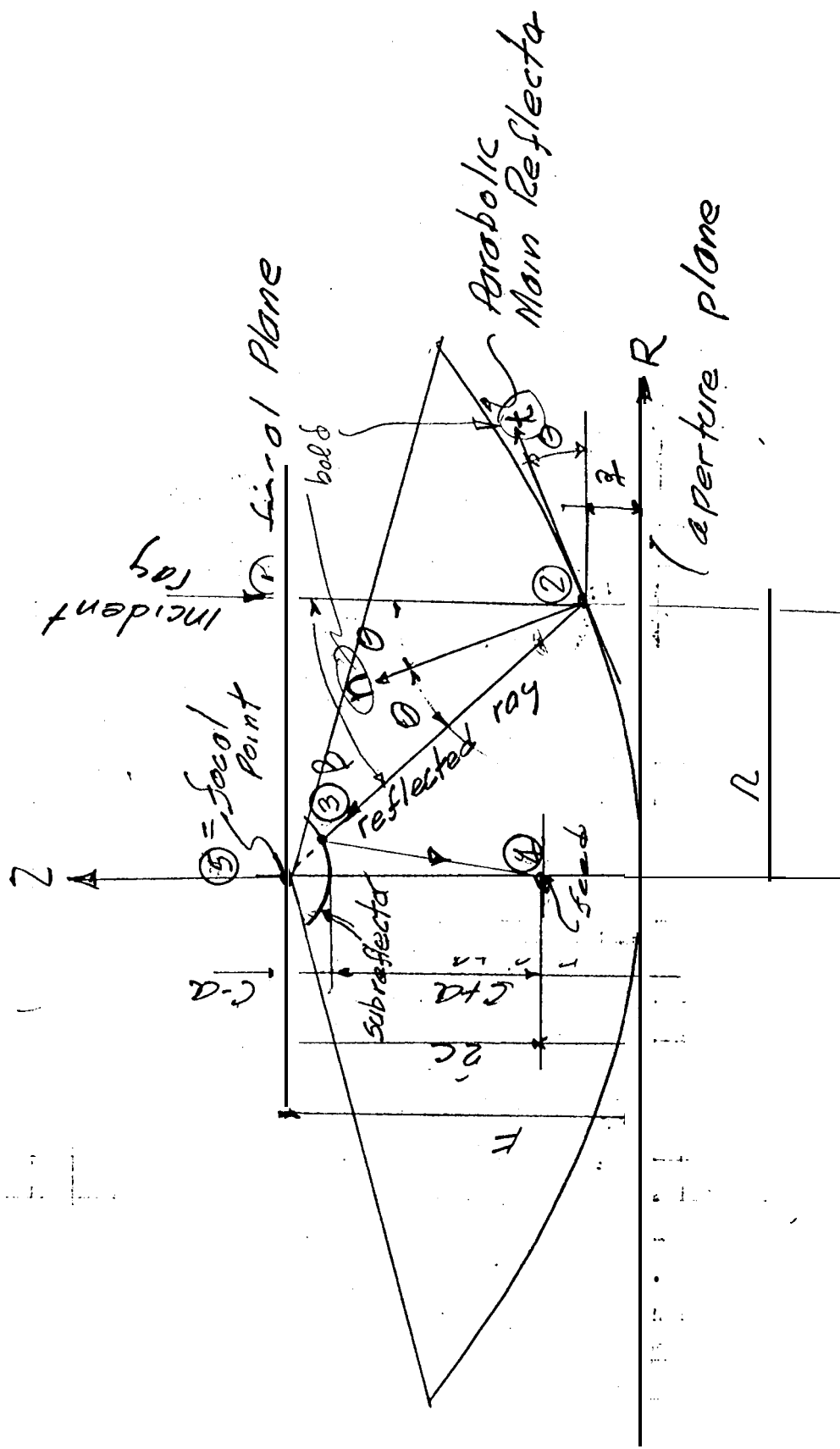


Figure 2-1

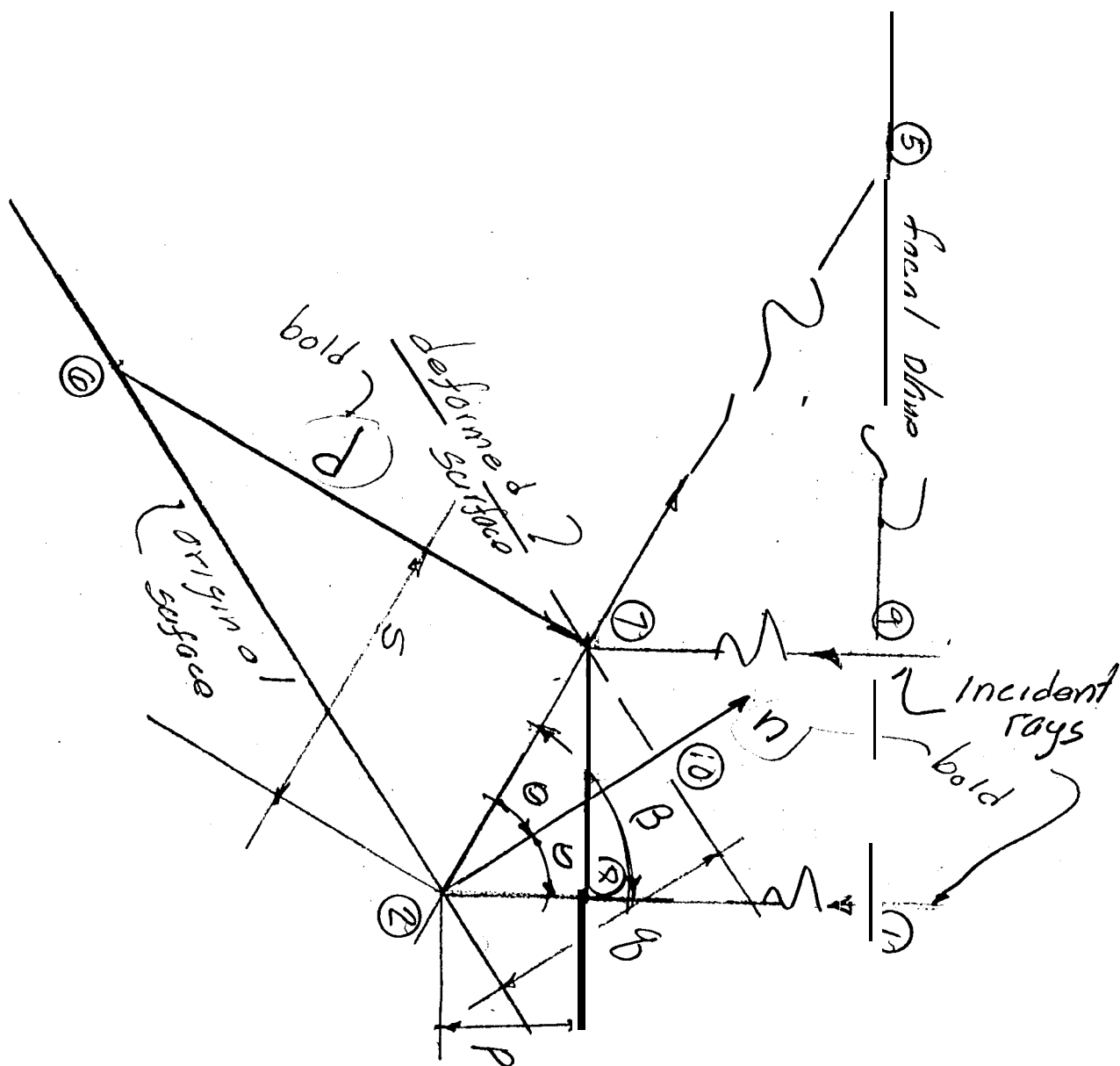


Figure 2-2

APPENDIX 2-A

PROGRAM TO COMPUTE BEST-FIT RMS PATHLENGTH

PATHA2 (Figure A2-1) is a MATLAB program to compute the half-pathlength error and the fitting parameters. The algorithms are constructed similarly to the process described in Chapter 2. The bulk data input is defined as the matrix "data," and there is one row for each node. The first two columns contain the X and Y coordinates (in a standard coordinate system; see Chapter 1). The third column, which traditionally contains the Z coordinate from some arbitrary data, is ignored because the code computes the Z coordinate from the parabolic equation. The next three columns contain the displacement triad, u, v, w. The last two columns contain the weighting factor and the node label. The node label is arbitrary, and it would be easy to modify the code so that only seven columns need be supplied. The focal length must also be supplied as input. The row vector "nopt" is an optional input that can be used to suppress any of the fitting parameters. The user prompt explains how this could be used. The six components of H, the fitting parameters, are ordered as in the text and the components are printed in that order at the end. Names of variables computed within the program are not always exactly the same as in the text. Nevertheless, the variables should be recognizable without difficulty.

```

% Dec 9, 1992 this is now PATHA2.M for Appendix 2
% A Matlab program to do pathlength analysis
% the input data requires focus, options and
%
%          (1) (2) (3)      (4) (5) (6) (7)      (8)
% bulk data(IDEAS format)[X   Y not used u v   w weight label]
format compact
disp('If there are nonzero options, supply row vector "nopt" ')
disp('(up to 6 terms) ')
disp(' such that nopt=[6 1] (alt or [ 1 6])')
disp(' will suppress X translation and Y-axis rotation;')
disp(' and nopt=[-2]will be changed to [1 6](symmetry) ')
disp(' for anti-symmetric half, supply nopt=[2 3 4 5]')
disp(' (any order is o.k.)')
disp('need to have "focus=..", & the n by 8 file "data", & CTRL-Z')
)
keyboard
x=data(:,1);y=data(:,2);u=data(:,4);v=data(:,5);w=data(:,6);
wgt=data(:,7);label=data(:,8);
z=(x.*x+y.*y)/4/focus;
t2=(x.*x+y.*y+4*focus*focus*ones(size(x))):
rho=-2*focus*(x.*u+y.*v-2*w.*focus)./t2;
t=sqrt(t2);
% form rho(new)=rho+A*H H=[X Y Z -deltaf/(f+deltaf) thetaX thetaY
]
f=focus;
gzgx=-2*f*x./t2 ;gzgy=-2*f*y./t2;gzgz=4*f*f*ones(size(x))./t2;
A=[-gzgx -gzgy -gzgz -z.*gzgz(z.*gzgy-y.*gzgz) (-z.*gzgx+x.*gzgz)
];
%now do classical normal equations
for j=1:6,qwa(:,j)=wgt.*A(:,j);end,
Am=A'*qwa; Bm=A'*(wgt.*rho); % this took <.1 sec
en=exist('nopt');
if(en==1)
    if ( nopt==-2),nopt=[ 1 6 ];,end %This "-2" is traditional
    nopt=sort(nopt);ll=length(nopt);
    for j=1:ll
        q=nopt(j);
        Am(:,q)=zeros(6,1);Am(q,:)=zeros(1,6);Am(q,q)=1; Bm(q)=0;
    end % on j
end % on if(en==1)
xx=-Am\Bm;
rhofit=rho+A*xx;
% get the best fit normals from rhofit
gz=2*focus*ones(length(wgt),1)./t; % gamma z
invgz=ones(size(gz))./gz;
dn=diag(invgz)*rhofit;
sumw=sum(wgt);
mmm=rhofit.*wgt; mmm1=mmm'*rhofit;
meansq=sum(mmm1)/sumw;
RMSNEW=sqrt(meansq)
NEWF=f/(1+xx(4))

```

```
DELTAf=NEWf- f
XOFF=XX(1)
YOFF=XX(2)
ZOFF=XX(3)
ROTX=XX(5)
ROTY=XX(6)
fprintf('Sum of weights is %g\n',sumw)
```

CHAPTER 3

DEFORMATION ANALYSIS

It was shown in Chapter 2 that the deformation vector \mathbf{d} is fundamental to the computation of the pathlength error. Antenna surface deformations are a function of environmental loading, factors such as wind, temperature, and - of primary importance - the effect of the gravity (self-weight) loading on the structure. The gravity effect is caused by the variable direction of the gravity vector with respect to the moving antenna surface as the antenna rotates about the elevation axis. Deformations are usually computed from a finite element method (FEM) analysis that applies the loading to a mathematical (analytical) model of the physical structure. FEM antenna models entail thousands of displacement degrees of freedom¹ and require the solution of a corresponding set of simultaneous linear equations. Nevertheless, the computer processing of antenna structures by any of a number of public or proprietary FEM software programs is well within conventional software and hardware capabilities.

The steps of model generation, data preparation, and computer utilization are familiar to almost all structural analysts, so they will only be touched upon here. This chapter will provide a brief overview of structural deformation analysis to orient those who may be unfamiliar with the process. More extensive details are available in many references that span the recent 30 year time period (e.g., Refs. 3.1 and 3.2). Some of the noteworthy development history will be reviewed first. Then deflection analysis will be illustrated for a primitive structure model. Both the Force and Displacement methods of structural analysis will be considered. Although the Force method is not the usual approach in production computer analysis software, it provides useful insight into the response of loaded structures and provides the basis for the antenna structure optimization procedure that will be covered in a subsequent chapter. The Displacement method is the more powerful of the two when automated computer structural analysis procedures are employed. Following these illustrations, analysis procedures will be extended from the primitive model to a more complex antenna structure.

¹There is one degree of freedom for each possible displacement component. Antenna structures, for example, will usually have three translational degrees of freedom at each node (joint) of the model, corresponding to the displacement components parallel to the X, Y, and Z coordinate axes. Three additional nodal degrees of freedom could be considered for structural models that include the rotations about these axes.

3.1 HISTORICAL BACKGROUND

Modern FEM analysis systems were preceded by matrix analysis methods in which the matrices were hand-generated and solved by whatever methods were available at the time. In the early days of structural analysis the solution methods consisted of slide rules and mechanical desk calculators and the equations were solved by iteration, relaxation, or elimination. The emergence of primitive computer systems dates to the 1940s and 1950s, but the process of adapting structural analysis to these computers and industry acceptance took many years.

The earliest widely distributed paper on matrix structural analysis may have been the 1952 classical Wehle and Lansing paper (Ref. 3.3), "Stiffness and Deflection Analysis of Complex Structures," in which the Force method of analysis (which has been supplanted by the Displacement method in more modern FEM programs) was used for airframe analysis. The extent of computer analysis prevalent at the time can be deduced from the author's caution that the analyst should always include check rows and columns in the computations, "even if the calculations are performed by means of IBM equipment" (Ref. 3.3, p. 681). The Displacement method, which is the method of choice in current FEM programs, was introduced in 1956 in another classic paper by Turner, Clough, Martin, and Topp (Ref. 3.4). The Force method is based upon the flexibility matrix, which is an influence coefficient matrix that provides the displacements at each degree of freedom of the model for independent unit loads at the other degrees of freedom. The Displacement method is based upon the stiffness matrix, which establishes the forces on the structure when an independent unit displacement is imposed upon each degree of freedom.

Clough, in a 1960 conference, coined the term "finite element," and also introduced the concept of assuming rational shape functions to represent element displacement patterns (Ref. 3.5). Shape functions are the basis of the more modern isoparametric element idea. Berman, a pioneering but sadly unappreciated advocate of computer processing, was one of the first to apply matrix computer analysis to a complex structure (Ref. 3.6). He proposed to analyze a large antenna structure by the Force method. The Force method effectively met its end for large-scale production applications when it was dropped as an alternative computer analysis procedure in developing the NASTRAN program (Ref. 3.7) in the late 1960s. Nevertheless, as will be demonstrated here, the Force method can be preferable to the Displacement method for hand analysis of models that entail only a small number of components. Also, this method can most readily supply the analyst with information about and insight into response characteristics of the particular structure. On the other hand, if the analytical model contains more than a few degrees of freedom, contemporary computer processing by any

method other than the displacement method is unusual.

In 1962, the STAIR program (Ref. 3.8) was developed for analysis of the 120-foot-diameter Haystack antenna. The STAIR program considered only the three orthogonal translational degrees of freedom at each of the nodes of the model. The FRAN program (Ref. 3.9) was subsequently developed for the same antenna to supplement the STAIR capability with the three rotational nodal degrees of freedom. Nevertheless, it traditionally has been assumed (and sometimes verified) that bending stiffness, which can be treated in programs that recognize rotational degrees of freedom, are higher order effects and can be ignored in contemporary well-designed antenna structures. Today, as deformation tolerances tend to become more stringent, this assumption warrants further investigation. The 64-meter MARS antenna was also analyzed by the STAIR program (Ref. 3.10) at about this time. Here, although STAIR contained an innovative version of what later was to become known as "substructuring," the available computer resources limited the model to a doubly-symmetrical one-quarter section of the full structure. This limitation has disappeared with modern computer capability. The primitive substructuring capability at that time required a great deal of ad hoc data preparation by the analyst. More recent programs attempt to go as far as possible in freeing the analyst from the chores of hand data preparation. As a matter of fact, computer automation has become so extensive that it is possible for a neophyte analyst to execute substantial computer processing without any real understanding of structural behavior. The possible consequences of an over-permissive computer program have actually become a source of concern for the structural engineering profession.

3.2 FORCE METHOD

A simple way to illustrate the Force method is to go through the steps in the analysis of an elementary model. This allows the essentials of the method to be demonstrated readily and the associated computations to be followed easily.

3.2.1 Analysis of a Three-Bar Truss

Figure 3-1a shows the analytical model of a two-dimensional truss structure that consists of the three bars labelled 1, 2, and 3. Specific values of the bar lengths, L_1 , L_2 , and L_3 , are dimensioned in the figure. Symbolic external loads P_1 and P_2 are applied in the directions of the X and Y coordinate axes, respectively. The structure is restrained in the X and Y directions at the left end. The roller shown at the right end permits movement in the X direction, so that at this end the structure is restrained only in the Y direction.

All three nodal joints² (at the junctions of each pair of bars) are assumed to be connected by pins that are capable of transmitting direct forces along the member axes but are not capable of restraining rotations of the members. The pin-jointed assumption is usually appropriate for antenna framework construction; the neglect of rigidity of the connections between members that can restrain the independent rotations at the joints is usually of secondary and higher order, rather than primary, importance. Because of the pin-jointed assumption, it would be more appropriate to denote these members that resist only the forces along their axes as "rods" and to reserve the connotation "bar" for members that resist both axial forces and the end moment couples that result from restraining free rotation at the joints.

The internal forces in the rods that result from the external loads can be computed in this case from static equilibrium. The requirements at each node are given by the three conventional force equilibrium conditions

$$\sum \text{Force}_\alpha = 0, \quad \alpha = X, Y, Z \quad [3.1]$$

where the summation is over all of the force contributions at the node. Therefore, "Force_α" in this equation does not distinguish between internal forces of the members acting on the joint, external loading, or the reactions that result from the restraint to joint displacements. From here on, to provide this distinction, "P" will be reserved to denote external loading, n will be used to denote internal member force, and R or P_r will be used to denote external reaction forces of restraint. All of the foregoing symbols can be particularized by appending subscripts as appropriate.

Individual free body diagrams of the rods are shown in Figure 3-lb. Here, n₁, n₂, and n₃ are assumed to be tensile forces on these members. By convention, the direction of the arrows shown at the ends of the member represent the directions of the forces applied by the members on the joint. Conversely, the forces applied to the members by the joints are in the opposite directions. Although not indicated in the figure, these forces can be visualized as acting in the directions opposite to those shown by the end arrows and in each case would tend to stretch the member, consistent with the assumption of member tension.

The components of the member force acting in the direction of any of the coordinate axes have the magnitude of the member

²"Nodes" and "joints" are considered here as interchangeable terms.

force times the direction cosine with respect to that axis. Consequently, the equilibrium conditions can be written in terms of the direction cosines and the as yet unknown rod forces. For example, at the upper joint of the truss the equations of equilibrium in the X and in the Y directions follow:

$$P_1 - n_1 \cos \gamma_{1x} + n_2 \cos \gamma_{2x} = 0 \quad [3.2a]$$

$$-P_2 - n_1 \cos \gamma_{1y} - n_2 \cos \gamma_{2y} = 0 \quad [3.2b]$$

For example, the term $\cos \gamma_{1x}$ refers to the direction cosine of rod 1 with respect to the X axis. Also, a positive sign is associated with forces in the positive X and Y directions. Here, the appropriate signs for n_1 and n_2 are determined by inspection from the arrow directions on the free body diagrams.

The direction cosine of a rod member with respect to a particular coordinate axis is given by the projection of the length of the member on that axis divided by the member length. For example, $\cos \gamma_{1x} = 18/30$ and $\cos \gamma_{1y} = 24/30$. It can be seen that when direction cosines in this form are substituted into Eqs. [3.2], or any of the equilibrium equations that can be written at the other nodes, the ratio n_i/L_i will appear for each rod i . Then by defining new terms $\lambda_i = n_i/L_i$ called the "tension coefficients" (Ref. 3.11), member force components are represented as the product of the tension coefficient and the projection of the member length along the corresponding coordinate axis. Using the tension coefficients instead of Eq. [3.2], the equilibrium conditions can immediately be written as

$$P_1 - 18\lambda_1 + 32\lambda_2 = 0 \quad [3.3a]$$

$$-P_2 - 24\lambda_1 - 24\lambda_2 = 0 \quad [3.3b]$$

Although it was simple to determine the signs in these equations by inspection, the signs above could readily be established automatically. One way to do this would be to apply a conceptual shift of the origin of coordinates to the center of each node at which the equilibrium equation is written and to consider whether or not the projected lengths are in the positive or negative coordinate directions with respect to the new origin.

We now consider two independent loading cases, where the loading is $P_1 = 1.00$ for the first case with $P_2 = 0$, and the loading is $P_2 = 1.00$ for the second case with $P_1 = 0$. The following is readily obtained from Eqs. [3.3]:

Load

Reference Equation

First Case

$$\lambda_1 = -\lambda_2 \quad 3.3b$$

$$\lambda_2 = -P_1/50 \quad 3.3a$$

Second Case

$$\lambda_1 = 32\lambda_2/18 \quad 3.3a$$

$$\lambda_2 = -18 P_2/(24*50) \quad 3.3b$$

λ_3 can be found from equilibrium in the X direction at the right end support. That is

$$-50\lambda_3 - 32\lambda_2 = 0; \text{ or } \lambda_3 = -0.64 \lambda_2$$

The equilibrium equations were established by assuming all the rods to be in tension. Whenever the tension coefficient is computed to have a negative algebraic sign the implication is that the rod force represents compression. The analysis for the rod forces is completed in the following table:

ROD	LENGTH	$P_1 = 1.00$ $P_2 = 0.00$		$P_1 = 0.00$ $P_2 = 1.00$	
		λ	$n = L\lambda$	λ	$n = L\lambda$
1	30	0.0200	0.60	-0.0267	-0.80
2	40	-0.0200	-0.80	-0.0150	-0.60
3	50	0.0128	0.64	0.0096	0.48

3.2.2 Displacements of a Three-Bar Truss

Hook's Law can be used to compute the extension of an elastic rod subjected to a tensile load, or equivalently, the shortening of a bar due to a compressive load. The law is

$$\sigma = E\epsilon \quad [3.4]$$

in which

σ is the stress (force per unit area)

ϵ is the strain (change in length per unit length,

E is the modulus of elasticity (Young's modulus)

Since the strain is non-dimensional, the modulus will have the same units as the stress. (We will not assign dimensional units here, but rather we will assume that dimensional quantities have

consistent appropriate units.) Representing the rod area as A and the extension as e , in terms of the prior notation, we have

$$\sigma = n/A \quad [3.5]$$

and

$$\epsilon = e/L \quad [3.6]$$

Then from Eqs. [3.4-3.6], it follows that

$$e = nL/AE \quad [3.7]$$

For illustration, arbitrary values are assigned for the rod areas, P_1 and P_2 , and $E = 10 \times 10^6$. The computations for the rod extensions are 'completed in the table below':

ROD	L	A	$P_1 = 2 \times 10^4$ $P_2 = 0.0$		$P_1 = 0.0$ $P_2 = 4 \times 10^4$	
			$n(x10^{-4})$	e	$n(x10^4)$	e
1	30	2.0	1.2	0.018	-3.2	-0.048
2	40	3.2	-1.6	-0.020	-2.4	-0.030
3	50	4	1.28	0.016	1.92	0.024

A physical requirement for the deformed truss is that the configuration with the applied loading must provide for fitting the extended rods together without gaps or interference. The application of this principle is illustrated conceptually in Figure 3-2. The effect of the second loading case is considered. Although the scale of the rod extensions has been greatly exaggerated, the figure is qualitatively accurate. The approach is to draw arcs with radii equal to the original lengths and to locate the new positions of the nodes at the intersection of the arcs. The restraint in the Y direction provides a simplification here because the displaced position at node 3 requires the new location to be shifted by the extension of rod 3 in the positive X direction ($u_3 = 0.24$) and to have no displacement in the Y direction ($v_3 = 0$). The new position of node 2 is found at the intersection of an arc with radius of $L_2 - 0.030$ drawn from the new location of node 3 and an arc with radius of $L_1 - 0.048$ from the fixed location of node 1. Consequently, the new location of node 2 shows that U_2 is positive and v_2 is negative with an obviously larger magnitude than U_2 .

In the years before computerized structural analysis matured, graphical analysis was frequently the means used to

compute truss deflections. A science of graphic statics was developed to simplify the procedure just described and to overcome the impracticality and inaccuracy of graphics that results from the several orders of magnitudes of differences in extensions when compared with the original lengths. Essentially, the need to represent member lengths as radii was eliminated and the arcs, such as in Figure 3-2, were replaced by tangents drawn perpendicular to the original directions of the rod members. Then a subsequent correction diagram was developed to ensure that the deflected configuration passed through the restrained nodes. The graphical procedures tended to become very difficult with complex planar trusses and were hopeless when applied to three-dimensional space. Nevertheless, understanding of the methodology of graphical analysis can provide an appreciation of structural behavior that may not be available from the much more comprehensive, but abstract, mathematical analysis.

There are several ways to compute deflections analytically. One well-known method is the Method of Virtual Work. This is based upon the principle that in a conservative structural system the work done by the external loading is equal to the internal energy stored within the structure. Note that work and energy are dimensionally equivalent and that work is the product of force and the component of displacement aligned with the force (the dot product). When a hypothetical "virtual" load is applied to the structure, this loading will cause "virtual" forces on the internal members of the structure. Assume that the virtual loading is applied first and that the real loading is applied subsequently. Then the added external virtual work will be the product of the virtual loading and the displacements of the "real" loaded structure. The added internal energy (work) of the members will be the product of the internal forces caused by the virtual loading and the extensions caused by the real loading. In practice, it is customary to apply a single-unit virtual load in the direction of the desired displacement component at any node whose displacement is to be determined. Therefore, equating the external virtual work to the virtual internal stored energy,

$$P_v \Delta_R = \sum n_v e_R \quad [3.8]$$

in which P_v is the external virtual load
 Δ_R is the displacement of the real structure
 n_v is the internal member force for the virtual load
 e_R is the extension of the member for the real load
and the summation on the right-hand side is taken over all members of the structure

Equation [3.8] applies in a generalized sense. That is, it includes generalized forces (forces and moments) and generalized displacements and extensions (translations and rotations). Therefore, work and energy are the products of forces times

translations, or else, moments times rotations. In the case of a structure consisting entirely of rod members, e_R is given by Eq. [3.7] and the displacement component at any point where a unit virtual load ($P_v = 1.0$) is applied parallel to that component becomes

$$u_\alpha = \sum n_v n_R L/AE \quad [3.9]$$

where u_α is the displacement component parallel to the X, Y, or Z axis (u, v, or w), and n_v and n_R are the rod forces for the virtual and real loading, respectively. Then the displacements at node 2 for the Three-Bar Truss can be developed in the following table:

ROD	L/AE (x10')	(xTo-')	n_v		$n_R n_v L/AE$ (x10 ²)	
			u	v	u	v
1	1.50	-3.20	0.60	0.80	-2.880	-3.840
2	1.25	-2.40	-0.80	0.60	2.400	-1.800
3	1.25	1.92	0.64	-0.48	1.536	-1.152
Σ					1.056	-6.792

Therefore, at node 2 we have

$$\begin{aligned} u_2 &= 0.01056 \\ v_2 &= -0.06792 \end{aligned}$$

which can be compared qualitatively with the graphical construction in Figure 3-2. Note that Eq. [3.9] can be constructed to get the deformation vector d (Eq. [2.20]) at each node of the structure. Also the terms L/AE in the second column of the table above are referred to as "element flexibilities." These terms represent the extensions of the rod elements for unit member loads.

3.2.3 Displacements by Matrix Formulation

A vector n_v in Eq. [3.9] represents the internal member forces for a unit external loading applied at a specific node in a specific direction. Then it follows that any particular vector of internal forces for some real external loading P_R can be constructed as the product of a matrix B with columns to contain an appropriate set of n_v vectors post-multiplied by the real loading P_R . The matrix B will have the form

$$B = [n_1 \ n_2 \ . \ . \ . \ . \ 0 \ . \ n_r] \quad [3.10]$$

where each n_i is the internal force vector for a unit external load at a particular degree of freedom. A vector of internal forces for a real external loading can be constructed as

$$n_R = B \{ P_R \} \quad [3.11]$$

and matrix of "real" internal forces n for a set of external loadings is obtained by substituting a matrix P on the right-hand side of the above equation to contain all the P_R columns of external loading. That is

$$n = B P \quad [3.12]$$

The matrix of internal member forces for a set of external virtual unit virtual loads is actually the B matrix post-multiplied by an identity matrix, which is equivalent to B . Also, a diagonal matrix f , called the "element flexibility matrix," is constructed to contain all the member L/AE flexibility terms. Equation [3.9], in conjunction with Eqs. [3.11] and [3.12], can then be written in matrix form to provide U , the matrix of displacement vectors for the set of external loadings P as follows:

$$u = B^t f B P \quad [3.13]$$

The first three matrices on the right-hand side of Eq. [3.13] are usually combined and called the structure flexibility matrix F , so that we have

$$u = F P \quad [3.14]$$

in which

$$F = B^t f B \quad [3.15]$$

and the row orders of U , P , B , and F are equal to the numbers of degrees of freedom in the model (which is approximately three times the number of unconstrained nodes for a pin-jointed three-dimensional structure).

To illustrate, using data in the table following Eq. [3.9],

$$B = \begin{bmatrix} 0.60 & 0.80 \\ -0.80 & 0.60 \\ 0.64 & -0.48 \end{bmatrix}, \quad f = 10^{-6} * \begin{bmatrix} 1.50 & 0.00 & 0.00 \\ 0.00 & 1.25 & 0.00 \\ 0.00 & 0.00 & 1.25 \end{bmatrix}$$

and from Eq. [3.15] the computation provides

$$F = 10^{-4} \begin{bmatrix} 0.1852 & -0.0264 \\ -0.0264 & 0.1698 \end{bmatrix}$$

Then, from Eq. [3.14], with

$$P = 10^4 * \begin{bmatrix} 2 & 0 \\ 0 & -4 \end{bmatrix}$$

$$u = F P = 10^{-2} * \begin{bmatrix} 3.704 & 1.056 \\ -0.528 & -6.792 \end{bmatrix}$$

It can be seen that the last column of u is consistent with the computations in the previous table.

3.2.4 Statically Indeterminate Structures

Member forces in the foregoing analysis of the Three-Bar Truss were statically determinate. That is, there was a one-to-one match in the number of unrestrained displacement degrees of freedom (two at node 2 and one at node 3) and the number of internal rod forces to be found. Consequently, there was exactly one equilibrium equation available for each internal force that was to be determined. Specifically, the truss, which was two-dimensional, had a total of six degrees of freedom (two per node), of which three were restrained (two at node 1 and one at node 3), leaving a remainder of three unrestrained degrees of freedom.

If there were more degrees of freedom than rod members, the structure would be unstable. For example, if the Y restraint were removed at node 3, there would be four equilibrium equations and only three rods. On the other hand, if there would be more rods than unrestrained degrees of freedom, say as for the truss in Figure 3-3, the rod forces (7) could not be uniquely found from the insufficient (5) equations of static equilibrium and the structure would be statically indeterminate. In this case some of the rods could be considered as redundant and the structure would be stable with these rods removed. A requirement for static equilibrium for a two-dimensional structure is that the number of rod members should be equal to twice the number of nodes minus the number of restrained degrees of freedom. The number of rods for a three-dimensional truss structure should be equal to three times the number of nodes minus the number of restraints. This is necessary but not a sufficient condition for statically determinate truss structures. It is insufficient because a structure meeting this criteria could be statically indeterminate in some local region and unstable in another.

The procedure to analyze a redundant truss structure is to reduce it to a statically determinate system by conceptually cutting selected redundant rods or by removing over-restraining reaction components. The forces in the cut members or the removed restraints are then treated as additional loads on the

reduced structure. The displacements of this statically determinate variation of the structure can then be analyzed to determine the hypothetical gaps between the cut members or the movement at the removed reaction points. Setting these gaps or movements to zero provides the means to evaluate the redundant member forces or reactions. The procedure will be outlined for the truss in Figure 3-3.

Figure 3-3b shows the statically determinate variation of the truss. Rod 1 has been selected to be cut and the Y reaction at node 1 has been selected for removal. The element flexibility matrix f is constructed as described previously for the seven bars, but the B matrix is partitioned vertically into the columns B_r associated with the member forces for the loads from the selected redundant and into the columns B_e associated with the actual external loads. That is

$$B = [B_r \quad B_e] \quad [3.16]$$

Carrying out the operations of Eq. [3.13], the displacement vector will contain U_r associated with the redundant forces P_r and U_e associated with the external loading P_e . The result is

$$\begin{bmatrix} U_r \\ U_e \end{bmatrix} = \begin{bmatrix} B_r^t f B_r & B_r^t f B_e \\ B_e^t f B_r & B_e^t f B_e \end{bmatrix} \begin{bmatrix} P_r \\ P_e \end{bmatrix} \quad [3.17]$$

Setting U_r equal to zero provides the following equation that can be solved for P_r

$$[B_r^t f B_r] P_r = -[B_r^t f B_e] P_e \quad [3.18]$$

The row equations in the bottom partition of Eq. [3.17] can be used to produce U_e after solving Eq. [3.18] for P_r . Also, by expressing P_r in terms of P_e , Eq. [3.12] shows how the member forces of the statically determinate variation are changed because of the redundant effects. The selection of redundant is an analyst's choice; the preferred selection will be the one that results in the smallest changes due to the redundancy.

In the example truss. of Figure 3-3 the P_r vector contains the indices n_1 and R_1 as indicated in Figure 3-3b. B_r contains two columns, one for each of these indices. The order of B_r is 7 rows by 2 columns. The order of B_e is 7 rows by as many columns as there are external loadings. The matrix f will have the order of 7 rows and 7 columns. U_r will have two components, one for the gap in rod 1 and one for the movement at R_1 . U_e can have as many as one row for each unrestrained degree of freedom and columns to match P_e .

Here, the order of the coefficient matrix used in the solution of Eq. [3.18] is two, which is equal to the order of the

redundancy. This illustrates a computational advantage of the Force method compared with the Displacement method; i.e., the order of linear simultaneous equations to be solved in the Force method is only the order of the redundancy, while, as it will be shown subsequently, the order in the Displacement method is equal to the number of unrestrained degrees of freedom.

For example, if the Displacement method were used to solve this problem, the coefficient matrix would be of order 5. This would not be a trivial problem to solve without computer aid. A drawback in the statically indeterminate case, however, is that, since the selection of redundant is arbitrary, it is necessary to choose an appropriate set of redundant. An inappropriate selection could lead to numerical conditioning problems and inaccurate results. There have been attempts to automate treatment of redundant by the Force method (Ref. 3.12), but the numerical effort is cumbersome.

3.2.5 Other Structural Components

Reference 3.1 discusses the extensions to treat other structural elements by the Force method. Some of the structural components for which elemental flexibility matrices are available in addition to rods are beams, triangular and rectangular plates, shear panels, and three-dimensional tetrahedra.

The method is particularly simple when applied to beams, such as in a building frame. For example, a simple beam element of span "a" is shown in Figure 3-4. The internal forces for which the element flexibility is developed are the bending moments m_L on the left side and m_R on the right side. The directions shown - clockwise on the left and counterclockwise on the right - indicate the sign convention for positive bending moments. Neglecting the effect of deflections due to shearing strain energy (which could be included if desired), the flexibility matrix of a beam element can be shown to be

$$f = \frac{a}{6EI} \begin{bmatrix} 2 & 1 \\ 1 & 2 \end{bmatrix} \quad [3.19]$$

where I is the bending moment of inertia and f provides the end rotations for the effect of end moments.

Figure 3-5 shows a simply supported beam with a transverse load P at the center. It is modelled by two beam elements, each of span $a = L/2$. Strictly speaking, when computing the deflection at the center, elemental flexibility matrix f of the beam structure would be a four-by-four diagonal block matrix with two-by-two flexibility matrices (according to Eq. [3.19]) on the diagonal, and the B matrix would have four components to represent the moments shown in the figure. However, a

simplification is available by taking into account that the moments at the two supports are zero and that the moment at the junction of the two elements is the same on each side of the centerline. Then the first and fourth rows and columns of F can be eliminated and the remaining two diagonal terms can be summed into a single term. Therefore, we have the simplifications $B = L/4$ and $f = L/(2EI) * (2+2)/6 = L/(3EI)$. Performing the multiplications of Eq. [3.15] we have $F = L^3/(48EI)$, which is a well-known result that has been obtained here almost by inspection.

3.3 DISPLACEMENT METHOD

It was shown previously that with the Force method it was first necessary to establish the member forces to compute the extensions and then after that the displacements could be obtained. In contrast, the Displacement method finds the displacements as the first step and from these can provide the member forces as a second step.

The key matrix of the Displacement matrix is the structural stiffness matrix K . By definition the stiffness matrix contains the forces that must act on the structure when unit displacements are imposed in turn on each particular degree of freedom and all other degrees of freedom are restrained (by the forces) to be zero.

The Displacement method is not considered to be as readily adaptable to intuition as the Force method; it is often possible to visualize the displacement vector, which is one column of the flexibility matrix, caused by a particular unit load. For the Displacement method, the forces that represent one column of the stiffness matrix that are necessary to provide a single unit displacement while preventing all other displacements are not as obvious.

The fundamental Displacement method relationship, which is the dual of Eq. [3.14], is

$$P = K U \quad [3.20]$$

An initial computation task is to generate K , which is a summation of the stiffness matrices k of all the component structural members. Then, when the external loading P is assembled, Eq. [3.20] is solved for U . One frequently employed method of solution will be described in Section 3.3.4.

Whenever the stiffness matrix K and the flexibility matrix F represent a matching set of degrees of freedom, these matrices form an inverse pair. Both matrices are symmetrical, which implies that the displacement at degree of freedom i for a unit

load at degree of freedom j is equal to the displacement at degree of freedom j for a unit load at degree of freedom i . Correspondingly, the force at degree of freedom i for a single unit displacement at degree of freedom j is equal to the force at degree of freedom j for a single unit displacement at degree of freedom i .

A major advantage of the Displacement method is that redundant do not have to be counted or identified and redundancy does not affect the computational procedures. On the other hand, the solution of Eq. [3.20] for U could entail the solution of a system of linear equations in the order of thousands, which is a highly computer-intensive operation. The order of the linear equation set to be solved in the Force method could be trivial in comparison.

3.3.1 Rod Element Stiffness Matrix

Equation [3.7] can be rearranged to provide the force n in a rod member for a known extension e in terms of the length L , cross-sectional area A , and modulus of elasticity E . Thus

$$n = AE/L e \quad [3.21]$$

and we have the stiffness relationship for the rod element, e.g.

$$n = k e \quad [3.22]$$

where $k = AE/L$, is sometimes referred to as the "spring constant" of the rod. That is k is equal to the force to provide a unit extension.

Figure 3-6 shows an extended rod subject to force n . The rod is connected to the nodes a and b as shown in the figure and a local coordinate system is aligned with the axis of the rod. The extension of the rod is $e = u_a - u_b$, where the arrow shows the positive direction of the local axis displacements, u . Then the stiffness relationship for the rod in the local coordinate system is

$$n = k \begin{bmatrix} 1 & -1 \end{bmatrix} \begin{Bmatrix} u_a \\ u_b \end{Bmatrix} \quad [3.23]$$

The components of a transformation from the local u coordinate system of the rod to a two-dimensional global X, Y coordinate system of a structure are shown in Figure 3-7. In Figure 3-7a the components of the extension u along the local axis are resolved into u and v along the X and Y axes, respectively. In Figure 3-7b the components of the rod force n are resolved into the components n_x and n_y along the

corresponding axes. Direction cosines γ_x and γ_y are identified as $\cos \theta_x$ and $\cos \theta_y$, respectively. Then, performing the transformations at both ends of the rod (ends a and b of Figure 3-6), we have

$$\begin{Bmatrix} \{U_s\} \\ \{u_b\} \end{Bmatrix} = \begin{bmatrix} \gamma_x & \gamma_y & 0 & 0 \\ 0 & 0 & \gamma_x & \gamma_y \end{bmatrix} \begin{Bmatrix} \{u_a\} \\ \{v_a\} \\ \{u_b\} \\ \{v_b\} \end{Bmatrix} \quad [3.24]$$

$$\begin{Bmatrix} \{n_{ya}\} \\ \{n_{xb}\} \\ \{n_{yb}\} \end{Bmatrix} = n \begin{Bmatrix} \gamma_x \\ \gamma_y \\ -\gamma_x \\ -\gamma_y \end{Bmatrix} \quad [3.25]$$

By substituting Eqs. [3.24] and [3.25] in Eq. [3.23], the result can be given exactly by Eq. [3.22], but now n and e are expressed in the global coordinate system as

$$n = \{n_{xa} \quad n_{ya} \quad n_{xb} \quad n_{yb}\}^t \quad [3.26a]$$

$$e = \{u_a \quad v_a \quad u_b \quad v_b\}^t \quad [3.26b]$$

and k in Eq. [3.22] is replaced by

$$k = \begin{bmatrix} k_n & -k_n \\ -k_n & k_n \end{bmatrix} \quad [3.27]$$

in which for a two-dimensional problem

$$k_n = k_2 = AE/L \begin{bmatrix} \gamma_x \gamma_x & \gamma_x \gamma_y \\ \gamma_x \gamma_y & \gamma_y \gamma_y \end{bmatrix} \quad [3.28]$$

In three-dimensional space with coordinate axes X , Y , and Z Eq. [3.22] is again valid, however the pairs n_x and n_y are replaced by the triplets n_x , n_y , and n_z , and the pairs u and v are replaced by the triplets u , v and w , and k_n in Eq. [3.28] is replaced by

$$k_n = k_3 = AE/L \begin{bmatrix} \gamma_x \gamma_x & \gamma_x \gamma_y & \gamma_x \gamma_z \\ \gamma_x \gamma_y & \gamma_y \gamma_y & \gamma_y \gamma_z \\ \gamma_x \gamma_z & \gamma_y \gamma_z & \gamma_z \gamma_z \end{bmatrix} \quad [3.29]$$

The stiffness matrices of the rods in the Three-Bar Truss will be developed explicitly with the help of the following table:

ROD	L/AE $\times 10^6$	AE/L $\times 10^{-6}$	γ_x	γ_y	$\gamma_x^2\gamma_y^2$	$\gamma_x\gamma_y$	$\gamma_y\gamma_x$
1	1.50	0.6667	18/30	24/30	0.36	0.48	0.64
2	1.25	0.8000	32/40	-24/40	0.64	-0.48	0.36
3	1.25	0.8000	50/50	0	1.00	0.0	0.0

Then, from Eq. [3.28] the k_2 partitions of the rod stiffness matrices are computed as:

$$\text{Rod 1} \quad k_2 = 10^6 \quad \begin{bmatrix} 0.240 & 0.320 \\ 0.320 & 0.420 \end{bmatrix}$$

$$\text{Rod 2} \quad k_2 = 10^6 \quad \begin{bmatrix} 0.512 & -0.384 \\ -0.384 & 0.288 \end{bmatrix}$$

$$\text{Rod 3} \quad k_2 = 10^6 \quad \begin{bmatrix} 0.800 & 0.0001 \\ 0.000 & 0.0001 \end{bmatrix}$$

The above 2-row, 2-column partitions of the rod stiffness matrices can be expanded to 4-row, 4-column stiffness matrices according to Eq. [3.27]. The element stiffness matrices are square and symmetrical. They will be used to construct the structure stiffness matrix in the following section, and it follows that this will also be square and symmetrical.

3.3.2 Structure Stiffness Matrix

The stiffness matrix of the full structure will have row and column indices for all of the degrees of freedom of the structure. For example, the column indices for the Three-Bar Truss will represent the displacements ($u_1, v_1, u_2, v_2, u_3, v_3$). The row indices will represent the matching set of external forces or reactions ($P_{x1}, P_{y1}, P_{x2}, P_{y2}, P_{x3}, P_{y3}$). The stiffness matrices of the rod element are entered into the structure stiffness matrix according to the correspondence of the element indices with the structure indices. Specifically, the element stiffness matrices will be entered to correspond with the following structure indices:

$$\begin{aligned} \text{Rod 1} & \quad [u_1 \quad v_1 \quad u_2 \quad v_2] \\ \text{Rod 2} & \quad [u_2 \quad v_2 \quad u_3 \quad v_3] \\ \text{Rod 3} & \quad [u_1 \quad v_1 \quad u_3 \quad v_3] \end{aligned}$$

When the stiffness matrix for more than one element contributes to a particular cell of the structure stiffness matrix, the contributions are added. Assembly of the structure stiffness matrices as just described is called the "Direct Method" of assembly. There are alternative ways for assembly, but the direct method is prevalent.

The assembled structure stiffness matrix K , for the Three-Bar Truss becomes

$$K_s = 10^6 \times$$

1.0400	0.3200	-0.2400	0.3200	-.8000	0.0000
0.3200	0.4267	-0.3200	-0.4267	0.0000	0.0000
-0.2400	-0.3200	0.7520	-0.6400	-.5120	.3840
-0.3200	-0.4267	-0.0640.	0.7147	.3840	-.2880
-0.8000	0.0000	-0.5120	0.3840	1.3120	-.3840
0.0000	0.0000	0.3840	-0.2880	-.3840	.2880

The rank of K_s above is three, which is equal to the number of rods. Since the matrix is of order six (two times the number of nodes), it has three singularities. Physically, these singularities represent possible rigid body modes of the structure. A rigid body mode represents a displacement vector that could occur in the absence of external forces. For example, three possible rigid body modes for this structure could be: 1) a translation in the X direction, 2) a translation in the Y direction, and 3) a rotation about an axis perpendicular to the X Y plane. Consequently, K_s , since it permits rigid body displacements, is referred to as the "unrestrained" stiffness matrix. It is necessary to apply restraints to this matrix to remove the singularities.

The restraints for the Three-Bar Truss can be found by inspection of Figure 3-1a. These are the u and v displacements at the left end node (node 1), and the v displacement at the right end node (node 3). These correspond with the first, second, and sixth rows and columns of K_s . Removal of these rows and columns would result in a stable structure with a non-singular stiffness matrix of rank 3. This is consistent with the criteria given in Section 3.2.4 that the number of rods (three) should equal twice the number of nodes (2 x 3) minus the number of restraints (3).

The singularities in the unrestrained stiffness matrix can be treated by rewriting Eq. [3.20] in partitioned form. The partitions in the following expression use the subscripts r and u

to represent restrained and unrestrained. The load vector P is partitioned into P_r , the reactions at the restrained degrees of freedom, and P_u , the external loads at the unrestrained degrees of freedom. The displacement vector is partitioned into U_r and U_u to correspond with the load vector. Then, the partitioned form of Eq. [3.20] is

$$\begin{Bmatrix} P_r \\ P_u \end{Bmatrix} = \begin{bmatrix} K_{rr} & K_{ru} \\ K_{ur} & K_{uu} \end{bmatrix} \begin{Bmatrix} U_r \\ U_u \end{Bmatrix} \quad [3.30]$$

By expanding the lower row equations and rearranging we have

$$K_{uu} U_u = P_u - K_{ur} U_r \quad [3.31]$$

which can be solved for U_u since P_u and U_r (if not null) are prespecified. Solution of Eq. [3.31] is the major computational task of the Displacement method.

Once the displacements at the unrestrained degrees of freedom are found from the equation above, the reactions can be recovered from the upper row equations of Eq. [3.30]. Thus

$$P_r = K_{rr} U_r + K_{ru} U_u \quad [3.32]$$

Specifically K_{rr} for the Three-Bar Truss is obtained by removing the first, second, and last row and column of K . Then the remaining three rows and columns are associated with the unrestrained displacements ($u_2 \ v_2 \ u_3$). This matrix becomes

$$K_{uu} \quad 10^6 \times \begin{bmatrix} 0.7520 & -0.0640 & -0.5120 \\ -0.0640 & 0.7147 & 0.3840 \\ -0.5120 & 0.3840 & 1.3120 \end{bmatrix}$$

Then the unrestrained displacements of the Three-Bar Truss are obtained by solving

$$K_{uu} U_u = \begin{bmatrix} 2 \times 10^4 & 0 & 1 \\ 0 & -4 \times 10^4 J \end{bmatrix}$$

from which the result is

$$\begin{Bmatrix} u_r \\ v_2 \\ u_3 \end{Bmatrix} = 10^{-2} \times \begin{bmatrix} 3.704 & 1.056 \\ -0.528 & -6.792 \\ 1.600 & 2.400 \end{bmatrix}$$

The final steps of the Displacement method are to compute the internal forces in the members (which can be used to

determine the stresses). This can be accomplished readily from Eqs. [3.23] and [3.24].

3.3.3 Input Data for Computer Analysis

The simple example of the Three-Bar Truss structure covered the typical steps that would be performed by a finite element computer program. These programs operate on personal computers, workstations, or mainframe computers to analyze antenna structures with many thousands of degrees of freedom and members. Prior to the use of these programs the analyst must develop an appropriate idealization of the actual structure, prepare a mathematical model of the idealization, either by hand notes, or by drawings and sketches, or with automated assistance. The mathematical model is converted to input data for the computer program in the form of records that resemble punchcard input, which is a carryover from the days when the input to a computer was primarily in the form of the, now-archaic IBM punchcards.

In preparing the data, the analyst can supplement or replace manual data generation and employ preprocessor programs, computer-aided design, or automated data generation procedures. The existing capabilities to assist in input data are too widespread and diverse to be covered here. Instead, we will consider the typical input data itself without being concerned with the machinery to develop it.

The essential input data for static loading deformation analysis consists of the following descriptions as a basis:

- a) Nodal geometry (coordinates).
- b) Elements and connectivity (type and associated nodes).
- c) Restrained degrees of freedom
- d) Element properties (cross-sectional).
- e) Material properties (with modulus of elasticity as a minimum and other material constants such as density, thermal coefficients, and terms of the material stiffness matrix when necessary).
- f) External loading.

Figure 3-8 shows a specification for the input data of a MATLAB finite element analysis program. The input records are the rows of the specific matrices provided for each type of data. The integer numbers arranged above the first row of each matrix indicate the column of the matrix for the entries. Additional data that can be input relate to the user's output requests, such as displacements, reactions and forces. The output of even a moderate size of structure model can be voluminous, and it is worthwhile for the user to be selective and to request only critical information.

This data format is similar to that of the NASTRAN program,

except that the NASTRAN input is not contained in matrices, but in individual records with a mnemonic in the columns of the first field of each record. NASTRAN records are 80 "card" columns wide and are subdivided into ten fields of eight columns each. The NASTRAN program and the input card format are widely known and understood. Consequently, a closely related format was adopted for the MATLAB structural analysis program. The NASTRAN input records can also be compressed to provide the same information in a free-field form.

Some notes on the data contained in the particular matrix columns of Figure 3-8 are given in Table 3-1. The specific data input to the finite element program for analysis of the Three-Bar Truss are shown in Figure 3-9.

3.3.4 Solution of the Load Displacement Problem

In a small problem such as the Three-Bar Truss, or even one that is one or two orders of magnitude larger, no special techniques are needed for the programming strategies, data management, or the numerical algorithms. However, production type structural analysis computer programs are developed with careful, and often innovative attention given to efficient and effective ways to handle and process the sometimes overwhelming amount of associated data. Historically, the scope of finite element structural analysis complexity and computer capability have kept pace with each other, and both have grown rapidly.

The solution of Eq. [3.20] represents the maximum imposition on the computer capability in terms of data storage and computation time. This phase of computer execution can be one-half or more of the total. At the outset, recognizing that the structure stiffness matrix and the element stiffness matrices are symmetrical provides one major reduction in storage. Then recognition of the sparse nature of the stiffness matrix provides another way to condense the storage space. The matrix is sparse because the nodes represented within the stiffness matrix are connected only to adjacent nodes. Therefore, each single row assigned to the stiffness matrix to represent one degree of freedom could contain only the one or two dozen coefficients associated with the adjacent nodes. This row will have as many columns - possibly thousands - assigned to it as there are degrees of freedom in the structure. Therefore, the row will be mostly empty except for the relatively few coefficients for the adjacent nodes. This emptiness leads to stiffness matrices that can be less than 1 percent populated.

Conceptually, the solution of the load deflection equations could be expressed as

$$u = K^{-1}P \quad [3.33]$$

However, the computation of the inverse of the stiffness matrix could be a formidable task except for small matrices of orders less than a few hundred. One of the preferred ways to solve Eq. [3.20] is to decompose the stiffness matrix into triangular factors by Gaussian elimination. The factors are applied in two subsequent steps - forward substitution and backward solution - to produce the displacements. The procedure is outlined below:

The factorization produces

$$\mathbf{K} = \mathbf{L} \mathbf{U} \quad [3.34]$$

where \mathbf{L} and \mathbf{U} are lower and upper triangular matrices.

It is customary to write Eq. [3.20] in the form

$$\mathbf{KU} = \mathbf{P} \quad [3.20a]$$

where \mathbf{P} is referred to as the "right-hand side." Therefore, Eqs. [3.20a] and [3.34] provide

$$\mathbf{L} \mathbf{U} \mathbf{U} = \mathbf{P} \quad [3.35]$$

Next the equation

$$\mathbf{L} \mathbf{Y} = \mathbf{P} \quad [3.36]$$

is solved for \mathbf{Y} . This step is the "forward substitutional step, and it is an explicit solution step that proceeds downwards along the lower triangular matrix to produce Y_1, Y_2 , etc. from the preceding values. The next step is obtain \mathbf{U} by solving

$$\mathbf{U} \mathbf{U} = \mathbf{Y} \quad [3.37]$$

This step is the backward "substitution" step and proceeds upwards from the bottom of the upper triangular matrix to produced the last component of \mathbf{U} first and each next higher component in turn from those already determined.

The major computations in this procedure are to decompose the stiffness matrix into the factors. Once the decomposition is available, the forward and back substitution to process numbers of right-hand side vectors is performed with only a relatively small effort.

One way to perform the decomposition is to start with the upper triangular portion of \mathbf{K} and to modify each row of the triangle by a subtractive correction that is contributed by the rows above the row that is being modified. The algorithm is

$$u_{ij} = K_{ij} - \sum_{q=1}^{i-1} u_{qi} u_{qj} / u_{qq} \quad [3.38]$$

The lower triangular matrix \underline{L} is obtained by dividing each row of \underline{U} by its diagonal term and taking the transpose. A common variation of the \underline{LU} decomposition is to let \underline{U} be the transpose of \underline{L} and introduce a matrix D , which contains the reciprocals of the diagonals of the prior \underline{U} . This leads to the well known \underline{LDU} decomposition of K in which \underline{U} is the same as \underline{L}^t , both have unity on the diagonals, and only one of them has to be stored.

The decomposition as described above entails dividing each row by the diagonal of that row to obtain the lower triangle. A very small divisor could be a warning of instability of the numerical process or also of instability of the physical structure. The numerical singularity (Ref. 3.13) is defined as the smallest ratio of the diagonal divisor of any row of the decomposition to the diagonal of the original stiffness matrix of the row. This diagonal ratio provides an easily obtained estimate of the condition number of the stiffness matrix; and the rule of thumb is that the absolute value of the exponent of the condition number indicates the number of digits of accuracy lost in the computations. We have found that models are suspicious when the magnitude of the exponent of the diagonal ratio is greater than about five, but that three or less can be considered "robust". In particular, when the diagonal ratio approaches zero (say $1 \cdot 10^{-10}$ or worse), it is possible that the structure has degenerated to a mechanism.

The decomposition will not preserve all of the sparsity of K . It can be seen from Eq. [3.38] that although a particular K_{ij} is null, there will be a contribution to the decomposition if any \underline{u}_{qj} and \underline{u}_{qi} from an upper row q are both not zero. The contribution is sometimes referred to as "fill," which results from "rain" falling down from an upper row in the "same column."

3.3.5 Matrix Bandwidth and Wavefront

According to Eq. [3.38], if K_{ij} is empty and if there are no terms in column j of the stiffness matrix above the term in row i , the decomposition will be empty in position ij . Thus the original sparseness of K will be preserved in this case. Large-capacity computer programs for structural analysis operate most efficiently when the computational procedure is formulated to capitalize on sparseness. Sparseness is used to advantage by confining the computational operations to a compact region densely populated with non-zero coefficients and by omitting operations for the empty region in which the coefficients are zero.

One measure of sparseness is the matrix bandwidth. The half-bandwidth at any row of the stiffness matrix is the number of columns from the diagonal to the furthestmost term of the row. There is no need when generating the decomposition to store or

process any of the zeros of a symmetrical stiffness matrix that are beyond the half-bandwidth. The maximum bandwidth is the maximum of all of the row bandwidths; the maximum is important because it is typically used to set the storage space for the decomposition and the scope of the processing. Another common measure of sparseness is the matrix wavefront (Ref. 3.14). The wavefront at a row is the number of active columns that follow the diagonal element; a column becomes active at the row containing the first entry for that column, and it remains active until that column is absorbed into the diagonal at a lower row.

Figure 3-10a shows the nodes and bars of a hypothetical structure to illustrate wavefront and bandwidth counting. Figure 3-10b shows the nodal connectivity matrix. The wavefront and half-bandwidth are tabulated on the right. An advantage of the wavefront method is that the wavefront can be less than, but never more than, the bandwidth. Another advantage for the wavefront storage is that one more node added to an existing structure model could be responsible for a devastating increase in bandwidth, but would add at most one connection to the wavefront.

Bandwidth or wavefront of the stiffness matrix are greatly affected by the numbering sequence of nodes and connections chosen by the analyst. A judicious numbering scheme could provide a major advantage in computer storage and calculations. Although the structural stiffness matrix is almost never small enough to be stored in core, there are reasons to keep one of the triangular decompositions matrices entirely in core. Storage needed for the decomposition is proportional to the square of the maximum criterion (bandwidth or wavefront). Similarly, the arithmetic to compute the decomposition is also proportional to the same criterion.

In addition to bandwidth and wavefront, "frontal," and "skyline" are other stiffness matrix storage schemes that capitalize on sparsity and are conveniently adaptable to the solution of the load deflection equations. Some of these storage schemes are summarized in Ref. 3.15.

Structural analysis software programs used in industry often allow the user the options of employing preprocessor codes to automatically resequence the nodes to reduce storage and to expedite the decomposition process. The programs provide a new nodal sequence in the form of a "was-is" list, which is transparent to the user and does not affect the sequence in which output results are presented. Most of these programs assume that the number of degrees of freedom for each node are approximately the same. This simplifies the preprocessing program by allowing it to operate at the nodal level rather than at the degree-of-freedom level. Several algorithms have been developed over the years to improve the sequencing of the connectivity matrix

(Refs. 3.16 thorough 3.18). Although there is a continuing search for the "optimum" resequencing algorithm, the existing algorithms do a good enough job to make the analysis of large structures tractable.

3.3.6 Centinuum Elements

The wide class of structures analyzed by computer can use many types of finite elements in the analytical models. Available elements include rods, beams, membrane, shear and bending plates of various shapes, curved plates, shell elements, toroids, ring elements, three-dimensional solids such as brick and tetrahedrons, etc. Nevertheless, only a minute subset of these element types are important to antenna structure models.

The rod element, which has been discussed at length here, predominates in the antenna backup structure. The beam, or bar, briefly considered in Section 3.2.5, is not frequently a primary member in antenna structures. Antenna performance requirements such as those that were considered in Chapter 2 make it necessary to control surface deformations to very small magnitudes. This is done by emphasizing stiff structures, which are achieved by deep trusses composed of rods. The beams are much shallower than the trusses that can be assembled and consequently are much more compliant. Although some rods will be connected to allow their bending stiffness to participate, this stiffness is ordinarily secondary because the rods are very shallow in contrast to the depth of the truss that contains the rod.

Nevertheless, there are plate-type elements within components of the antenna structure other than in the reflector backup. Some of these components could occur in subreflector supports, elevation axis wheels, and alidades or pedestals. These plates act primarily as membrane elements. That is, their in-plane load carrying capability will overshadow the ability to carry loads applied normal to their planes. Furthermore, although they have some small capability to resist in-plane bending about an axis normal to the plane of the plate, the membrane plates are not ordinarily connected to the remainder of the structure at their exteriors to develop this capability. The usual FEM models of these plates, which are either triangular or quadrilateral, represent only the three translation degrees of freedom at their corner nodes. Their stiffness matrices, similar to the rods, model only the three nodal forces in terms of the nodal degrees of freedom.

Rods and bars are two-node "lattice" (Ref. 3.13) elements that can be modelled accurately with finite numbers of degrees of freedom. Lattice elements do not introduce discretization errors; that is, adding nodes to subdivide them into additional intervening elements will not change their accuracy. For

example, if the structure of Figure 3-4 were subdivided into many more than the two bar elements shown, the computed deflection under the load would be the same. On the other hand, plates are continuum elements that have infinite numbers of degrees of freedom and can be modelled only approximately by finite numbers of degrees of freedom.

The plates that occur in antenna structures are triangular and quadrilateral membrane plates. The stiffness matrix for a constant strain, three-node triangular plate can readily be expressed in closed form. However, the constant strain condition imposes a constant stress condition also. This makes the plate overly rigid and therefore detrimental to modelling accuracy. Although the closed form stiffness matrix is desirable for computer code generation and processing, it is best not to employ the triangular plate except when necessary as a transition between the nodes of an irregular region. The four node quadrilateral membrane plate is a useful continuum element that can model a linear stress distribution within its boundaries and therefore is capable of a higher level of accuracy than the three-node triangular plate.

The approach in treating continuum elements with the restriction that only a finite number of degrees of freedom are available at their exterior nodes³ is to postulate continuous functions for interpolating the interior coordinates from the nodal coordinates, and also the interior displacements from the exterior nodal displacements. The "isoparametric" elements use the same interpolation functions for coordinates and for displacements. These elements can represent irregular shapes and curved boundaries when necessary.

Generation of the stiffness matrix for the isoparametric quadrilateral plate entails some engineering mechanics theory and also a substantial amount of computation. Details of the procedure can be found in a number of references, including Refs. 3.1, 3.2, 3.13, and 3.15. The procedure, following the exposition in Ref. 3.2, starts from the "Principle of stationary energy" (sometimes referred to as the "minimum of the total potential;" see Ref. 3.11).

Broadly, the principle states that the total potential for a system in equilibrium is stationary (actually a minimum) with respect to virtual changes in the displacements. In an elastic structure the total potential P consists of the net internal strain energy U stored in the structure, and V , the potential of the loads. The net strain energy includes the strain energy that

³Unless special additional nodes are established along their edges or interiors

occurs because of the loading and additional terms that can occur if there are initial stresses and strains, such as from preload and thermal effects. The potential of the loads is the negative (lost potential) of the work done by the external loads, which include concentrated exterior forces, body forces, and surface tractions. Omitting the effects of initial stresses and strains, and body forces and surface tractions, \mathcal{U} and \mathcal{V} , are given by

$$\mathcal{U} = \sum^m (\int_{\text{volume}} \frac{1}{2} e^t \mathbf{E} e \, dv), \quad m = \text{number of elements} \quad [3.39]$$

$$\mathcal{V} = \mathbf{U}^t \mathbf{P} \quad [3.40]$$

In the above, the strain energy is the sum of the strain energies of all the elements, e is the vector of element strains, \mathbf{E} is the material stiffness matrix (representing the stress-strain laws), and dv represents differential volume. (As defined previously, \mathbf{U} and \mathbf{P} are the structure displacement and loading matrices.)

The strain displacement equations can be used to represent the element strains in terms of the subset u of the structure displacements associated with the element. This provides

$$e = \mathbf{B} u \quad [3.41]$$

where the matrix \mathbf{B} is a matrix of differential operators. Using the above equation in Eq. [3.39], the strain energy can be expressed as

$$\mathcal{U} = \frac{1}{2} \sum^m \int u^t \mathbf{B}^t \mathbf{E} \mathbf{B} u \, dv \quad [3.42]$$

The element stiffness matrix k is defined from the above equation by

$$k = \int \mathbf{B}^t \mathbf{E} \mathbf{B} \, dv \quad [3.43]$$

Therefore, the strain energy is expressed in terms of the element stiffness matrix and nodal displacements

$$\mathcal{U} = \frac{1}{2} \sum u^t k u \quad [3.44]$$

The summation operator above can be removed by recognizing that \mathbf{U} , the structure displacements, is the union of all the element displacements u , and that \mathbf{K} , the structure stiffness matrix, is the union (and summation) of all the element stiffness matrices k . As the result we have

$$\mathcal{P} = \frac{1}{2} \mathbf{U}^t \mathbf{K} \mathbf{U} - \mathbf{U}^t \mathbf{P} \quad [3.45]$$

and the stationarity condition $\partial \mathcal{P} / \partial \mathbf{U} = 0$ provides the familiar

equation

$$KU = P \quad [3.20a]$$

The element stiffness matrices are obtained from the integrations in Eq. [3.43]. Quadrilateral plate elements are first projected onto a local x, y coordinate system in the plane of the plate. After the stiffness matrix is developed in this plane, it is transformed back into the original X, Y, Z global coordinate system of the structure.

The quadrilateral plate is developed in the local $x-y$ plane by means of an auxiliary ξ, η non-orthogonal, non-dimensional, quadrilateral coordinate system. The local coordinates of a point of the plate are expressed as

$$\begin{Bmatrix} x \\ y \end{Bmatrix} = \begin{bmatrix} N & 0 \\ 0 & N \end{bmatrix} \begin{Bmatrix} X \\ Y \end{Bmatrix} \quad [3.46]$$

in which X and Y are 4×1 vectors of the local coordinates at the four nodes and $N = [N_1 \ N_2 \ N_3 \ N_4]$ are shape functions.

The displacements within the plate are expressed in terms of the same shape functions as

$$\begin{Bmatrix} u \\ v \end{Bmatrix} = \begin{bmatrix} N & 0 \\ 0 & N \end{bmatrix} \begin{Bmatrix} U \\ V \end{Bmatrix} \quad [3.47]$$

and similarly, U and V are the 4×1 vectors of the displacements at the corner nodes of the plate.

An example of suitable shape functions has the form

$$N_i = \frac{1}{4}(1 \pm \xi)(1 \pm \eta) \quad i = 1, 2, 3, 4 \quad [3.48]$$

in which the signs are established so that each N_i has the value of unity at one specific corner of the plate. This is possible because the auxiliary coordinates are normalized so that ξ and η have the values ± 1 at the corners.

The differential operator matrices B in Eq. [3.41] are applied to the shape functions (as they appear in Eqs. [3.47]) in the ξ, η coordinate system. The Jacobian matrix J is established to provide the transformation from the ξ, η coordinates to the local x, y coordinates. The B matrix is then multiplied by the inverse of the Jacobian matrix to convert it from the ξ, η coordinates to the local x, y coordinates. The integrations in Eq. [3.43] are performed in the ξ, η coordinates, and this is accounted for by multiplying the integrand by the determinant of the Jacobian $|J|$. The plate thickness is assigned the symbol t

so that the integration, in place of Eq. [3.43], becomes

$$k = \int B^t E B \ t |J| \ d\xi \ d\eta \quad [3.49]$$

This integration is usually executed by from two- to four-point two-dimensional Gaussian quadrature. The stiffness matrix so obtained has order 8 because at each of four nodes it provides the correspondence of two force components (P_x , P_y) with two displacement components (u , v). After transformation to the global x , Y , z coordinates, it will be of order 12. The auxiliary ξ, η coordinate system is not needed for a rectangular plate because operations in the x , y coordinates are performed conveniently. In that case Eq. [3.43] can be applied directly.

3.4 ANTENNA BACKUP STRUCTURE COMPUTER MODEL

Antenna backup structures, which provide the immediate supports for the reflector panels, are typically systems of three-dimensional trusses. The trusses and associated bracing are composed of rod members such as those considered previously in the Three-Bar Truss problem. The structural configuration consists of a set of radial rib trusses interconnected by a set of circumferential hoop trusses. A top view of a typical radial rib-hoop truss system was shown previously in Figure 1.-18. The interior structure within the 360-degree aperture is an assembly of essentially repetitive modules.

Figure 3-11, reproduced from Ref. 3.19, shows the construction of 15-degree repetitive module of a typical antenna backup structure. All members of this module can be categorized as one of ten distinct types. Four of these occur in the rib truss (Figure 3-11d); they are the top rib chord, the bottom chord, the post from top to bottom chord, and the diagonal from the top of one ring to the bottom of an adjacent ring. The hoop truss (Figure 3-11,b,c) provides three more types; top, bottom, and diagonal (the post is supplied by the rib truss). The intermediate rib (Figure 3-ha) is actually only a top rib chord member supported by the hoop truss, as shown in Figure 3-11c. The three remaining member types are a diagonal connected between the top of one rib at one ring to the top of another rib at the next ring, a similar diagonal connecting nodes at the bottom of ribs, and an inclined diagonal connecting a rib top to a rib bottom at adjacent rings.

The layout in Figure 3-11 was proposed in a design study for 64-meter-diameter antennas. Although there are thousands of individual rod members in the backup structure, the repetitive character of the construction requires only 130 different rod detailing variations. The regularity of construction and the similarities in the structural format of many antennas make it

feasible to design software preprocessor programs to develop the input data for structural analysis. A half-section analytical model of this structure requires about 4000 data card records (such as those described in Figure 3-8). These records can be generated in a few seconds by a mainframe computer. A general-purpose antenna structure data generator needs only a few additional user parameters such as diameter, numbers of rings and their radii, focal length, and possibly five to ten more option-defining parameters.

The simplicity of ring and rib backup structure arrangement makes it both feasible and logical to use a readily interpreted numbering code. Specific entries in the input records can be identified with respect to location on the structure without the need to consult a drawing or other notes for the mathematical model. The schedule below shows a numbering code that will cover most backup structure situations.

BACKUP STRUCTURE NUMBERING SCHEDULE

NODE LABEL: $100 \times \text{Ring} + 2 \times \text{Rib}$ For Bottom Rib Nodes
 $100 \times \text{Ring} + 2 \times \text{Rib} - 1$ For Top Rib Nodes

ROD LABEL: $10,000 \times \text{Rib} + 100 \times \text{Ring} + \text{TYPE}$

TYPE

- 1 Rib Top
- 2 Rib Bottom
- 3 Rib Diagonal
- 4 Rib Post
- 5 Hoop Top
- 6 Hoop Bottom
- 7 Hoop Diagonal
- 8 Top Node Diagonal
- 9 Bottom Node Diagonal
- 10 Inclined Top to Bottom Diagonal
Between Adjacent Rings

PROPERTY LABEL: $100 \times \text{CLASS} + \text{DEL} + \text{SLAVE} + \text{TYPE}$

CLASS is an integer assigned to the ring
 DEL is a multiple of 20 to permit up to 4 variations
 within the ring annulus
 SLAVE is 10 only at the Y-Z plane of symmetry
 and zero otherwise

Figure 3-12 shows plan view sketches for symmetrical half models of antenna backup structures three different diameters. The sketches show support points at particular bottom nodes of the rib trusses. These supports are provided by the underlying elevation wheel structure, possibly with additional transition structures between wheels and rib trusses. (Some of the supporting construction variations can be seen in the first five figures of Chapter 1.) Backup structure support models for structural analysis tend to differ from installation to installation and do not emphasize repeatability. Consequently, the data input is prepared ad hoc without significant benefit of automation aids.

Surface accuracy and microwave precision for these antennas imposes requirements on the number of supports for the backup structure. The 15m antenna shown is adequately supported at three supports (at the corners of an equilateral triangle). The implied four supports (at the corners of a square) are considered to be sufficient for the 26m antenna. Eight supports are desirable for the 40m antenna, and these are assumed to be provided by a trussed ring girder. The ideal ring girder provides equal, or nearly equal, stiffness at the reflector attachments, and it is a design challenge to achieve this. The radii to the supports for the three antennas of the figure are about 40% of the maximum radii. An alternative concept for backup structure support is a compact central hub weldment. The rib trusses in this concept are essentially cantilevered from the hub.

An innovative concept for equal stiffness backup structure supports has been used successfully for the 100m radio telescope near Bonn, Germany (Ref. 3.20). This concept provides a series of supporting bars that are arranged on the generators of a cone. A similar arrangement is shown in Figure 3-13, which is taken from Ref. 3.21. There are 24 identical cone bars employed. The attachment points to the backup are indicated by the points marked "S" in the plan view of Figure 3-ha. Figure 3-13 shows views that define the transition structure from the elevation bearing to the backup structure and incorporate the cone bars. Unfortunately, this arrangement calls for structure below the antenna along the focal axis, and this structure blocks the clear passage through the vertex of the reflector that would be needed for a beam-waveguide antenna (Figure 1-8).

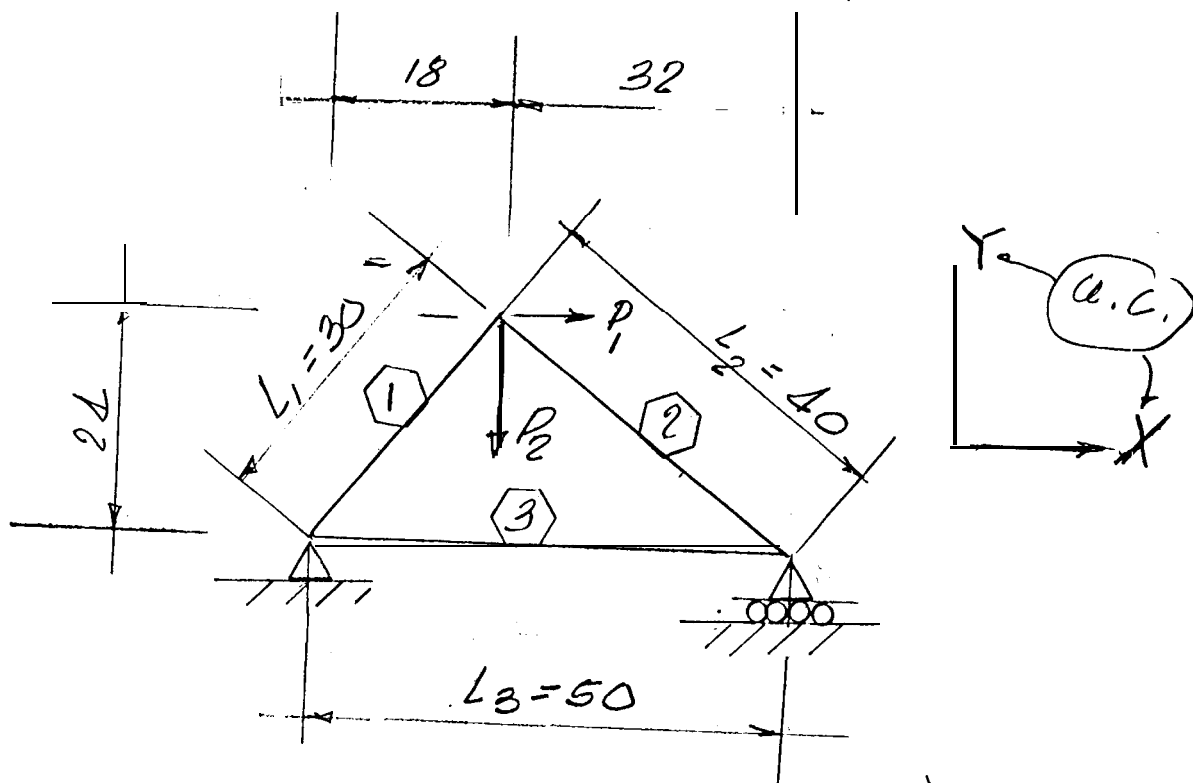
REFERENCES

- 3.1 Przemieniecki, J. S., Theory of Matrix Structural Analysis, NY: McGraw-Hill Book Co., 1968.
- 3.2 Cook, R. D., Malkus, D.S., and Plesha, M. E., Concepts and Applications of Finite Element Analysis, NY: John Wiley & Sons, 1989.
- 3.3 Wehle, Jr., L. B., and Lansing, W., "A Method for Reducing the Analysis of Complex Redundant Structures to a Routine Procedure," J. Aero. Sci., vol. 19, no. 10, October 1952.
- 3.4 Turner, M. J., Clough, R. W., Martin, H. C., and Topp, L. J., "Stiffness and Deflection Analysis Of Complex Structures," J. Aero. Sci., Vol. 23, no. 9, 1956, 805-823.
- 3.5 Clough, R. W., "The Finite Element Method in Plane Stress Analysis," presented at the 2nd Conference on Electronic Computation, American Society of Civil Engineers, Pittsburgh, PA, September 8-9, 1960.
- 3.6 Berman, F. R., "The Use of a Transformation Chain in Matrix Structural Analysis," presented at the ASCE Conference on Electronic Commutation, November 1958.
- 3.7 The NASTRAN User's Manual, Section 2.4, NASA SP-222(06), Athens, GA: COSMIC, September 1983.
- 3.8 STAIR (Structural Analysis Interpretive Routine) Instruction Manual, Lincoln Manual No. 48, Lexington, MA: MIT Lincoln Laboratory, March 1962.
- 3.9 IBM 7090/7094 FRAN (Framed Structures Analysis Program 7090-EC-01X), White Plains, NY: International Business Machines Corporation, September 1964.
- 3.10 Katow, M. S., "Techniques Used to Evaluate the Performance of the NASA/JPL 210-ft Reflector Structure Under Environmental Loads," in Mar, J. W., and Leibowitz, Eds., Structures Technology for Large Radio and Radar Telescope Systems, Cambridge, MA: The MIT Press, 1969.
- 3.11 Hoff, N.J., The Analysis of Structures, NY: John Wiley & Sons, 1956.
- 3.12 Robinson, J., Structural Matrix Analysis for the Engineer, NY: John Wiley & Sons, 1966.
- 3.13 Melosh, R. J., structural Engineering Analysis by Finite Elements, Englewood Cliffs, NJ: Prentice Hall, 1990.

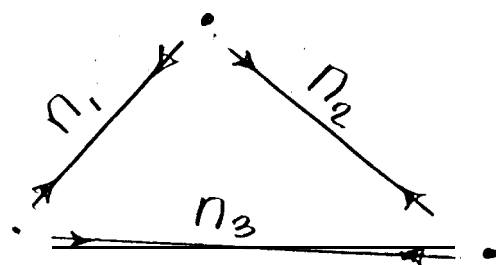
- 3.14 Melosh, R. J., and Bamford, R. M., "Efficient Solution of Load-Deflection Equations," J. Struct. Div., Vol. 95, no. ST4, ASCE, April 1969, pp. 661-676.
- 3.15 Bathe, K.J., Finite Element Procedures in Enaineering Analysis, Englewood Cliffs, NJ: Prentice Hall, 1982.
- 3.16 Levy, R. , "Resequencing of the Structural Stiffness Matrix to Improve Computational Efficiency," JPL Quarterly Technical Review, vol. 1, no. 2, Pasadena, CA: Jet Propulsion Laboratory, California Institute of Technology, July 1971, pp. 61-70.
- 3.17 Gibbs, N. E., Poole, W. G., and Stockmeyer, P. K., "An Algorithm for Reducing Bandwidth and Profile of a Sparse Matrix," SIAM J. Num. Anal., vol. 13, no. 2, 1976, pp. 236-250.
- 3.18 Everstine, G. C., "A Comparison of Three Resequencing Algoritms for the Reduction of Matrix Profile and Wavefront," Int. J. Num. Meth. Engng., vol. 23, no. 2, 1979, pp. 837-853.
- 3.19 Levy, R. , "Conceptual Studies for New Low-Cost 64-m Antennas," JPL Deep Space Network Progress Report 42-33 March and April 1976, Pasadena, CA: Jet Propulsion Laboratory, California Institute of Technology, July 1976, 55-67.
- 3.20 Hachenberg, O., Grahl, B., and Wielebinski, R., "The 100-meter Radio Telescope at Effelsburg," Proc. IEEE, vol. 61, September 1973, pp. 1288-1295.

FIGURES

- 3-1. Three-Bar Truss: a) Layout; b) Free Body
- 3-2. Deformed Truss
- 3-3. Redundant Truss: a) Redundant to Second Degree; b) Statically Determinate Conversion
- 3-4. Beam Element
- 3-5. Loaded Beam
- 3-6. Rod Extension
- 3-7. Global Components: a) Extensions; b) Forces
- 3-8. Input Data Matrices for Matlab Finite Element Program
- 3-9. Three-Bar Truss Problem Input Data
- 3-10. Connectivity Counting Example: a) Example Structure; b) Connectivity Matrix
- 3-11. Backup Structure Framing Matrices:
- 3-12. Backup Structure Support
- 3-13. Cone Support for Backup Structure
- Table 3-1. Data Preparation Notes for Finite Element Structure Analysis



a) Layout



b) Free body diagrams

Figure 3-1
Three Bar Truss

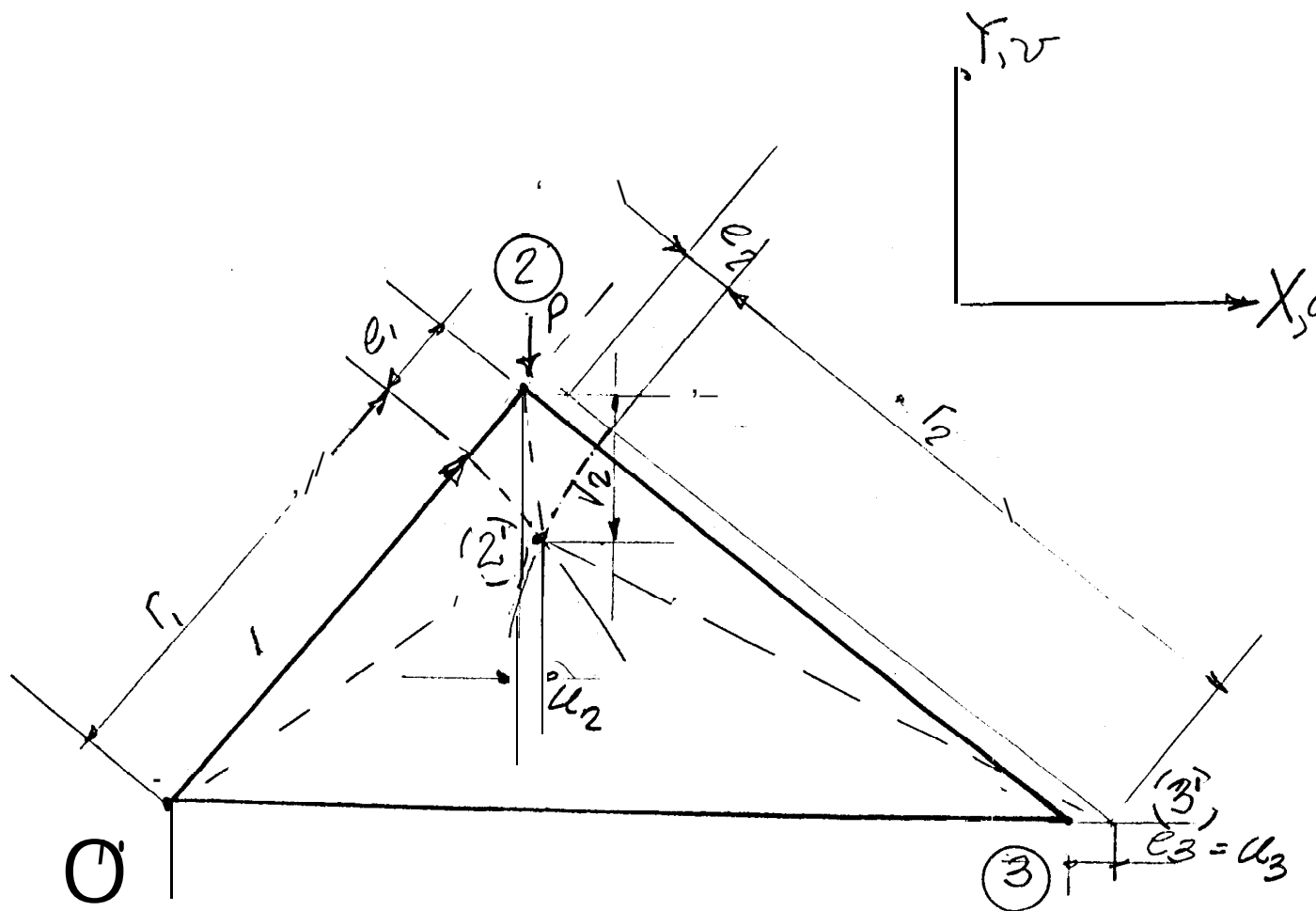


Figure 3-2
Deformed Truss

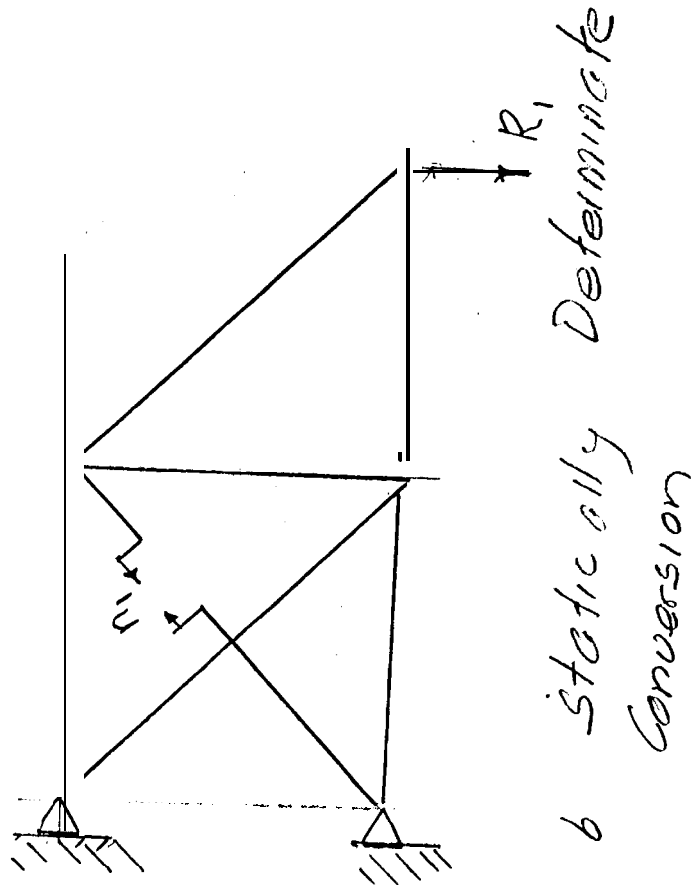
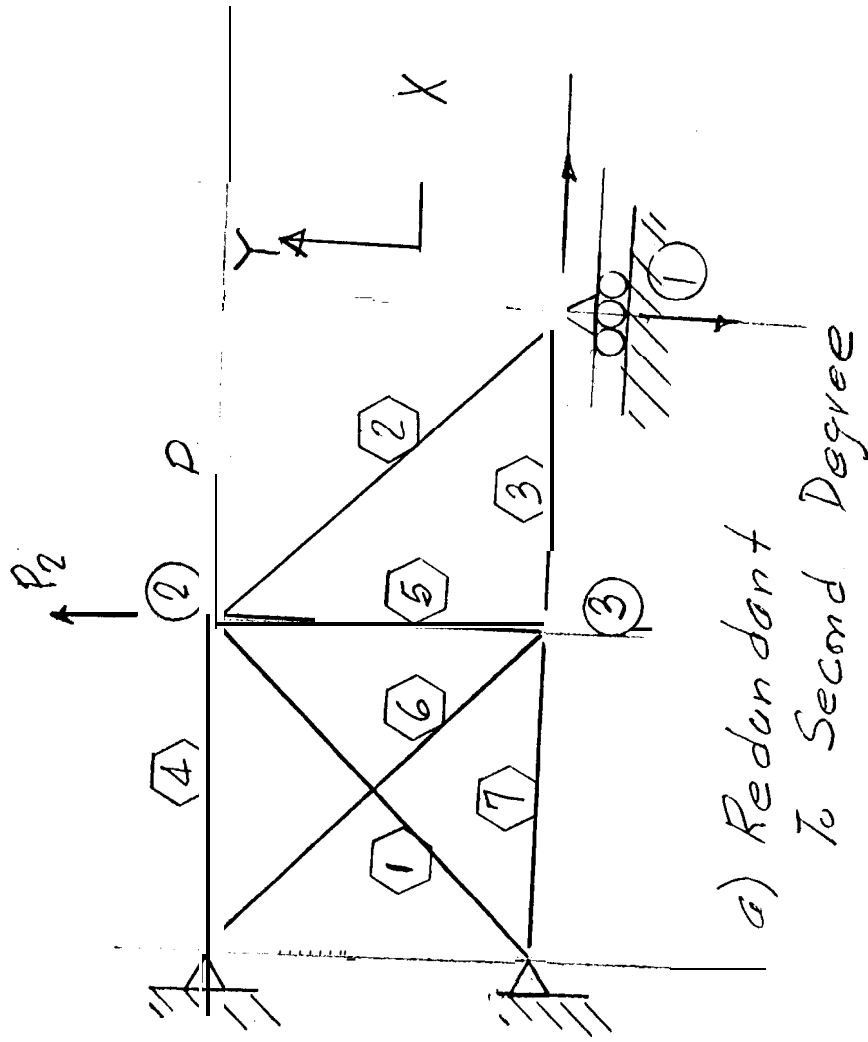
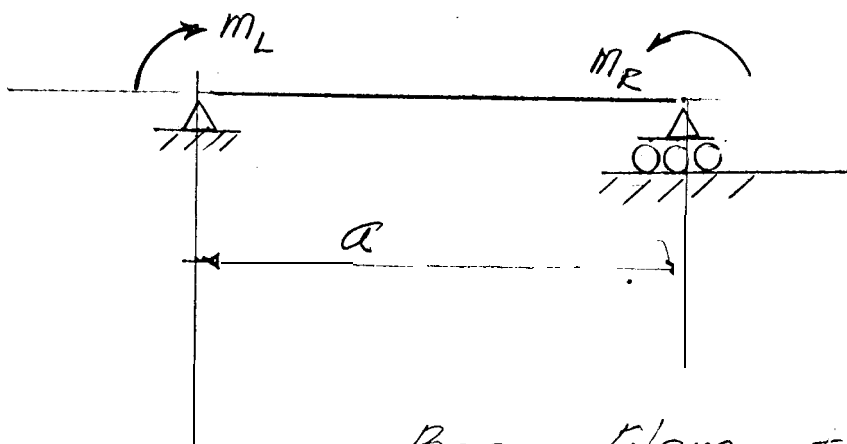
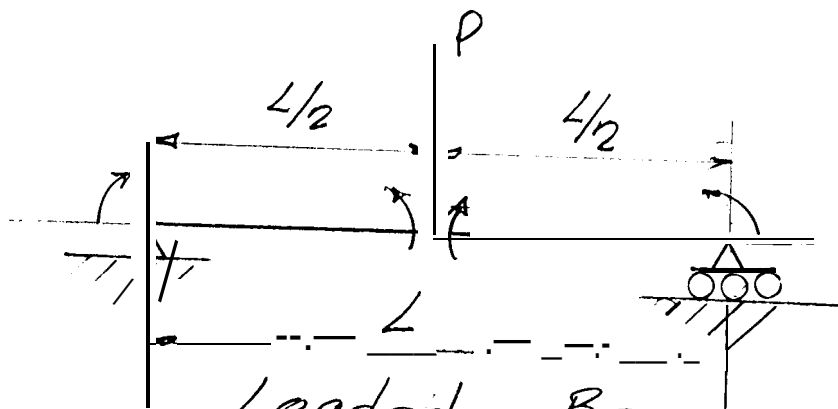


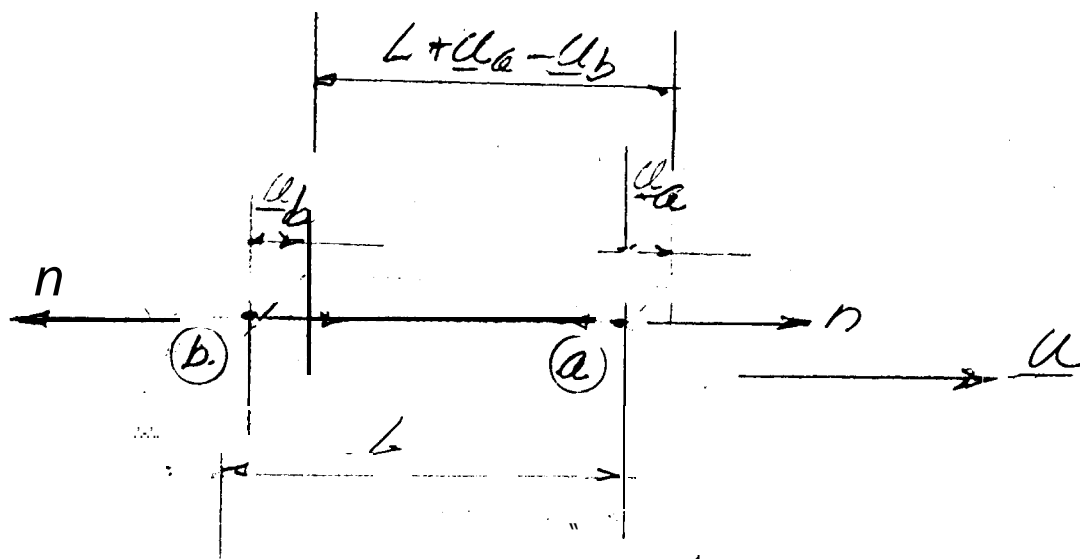
Figure 3-3
Redundant Truss



Beam Element
Figure 3-4

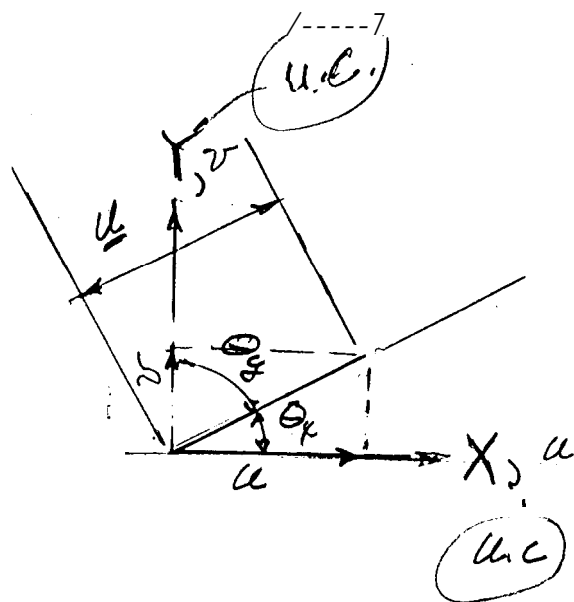


Loaded Beam
Figure 3-5

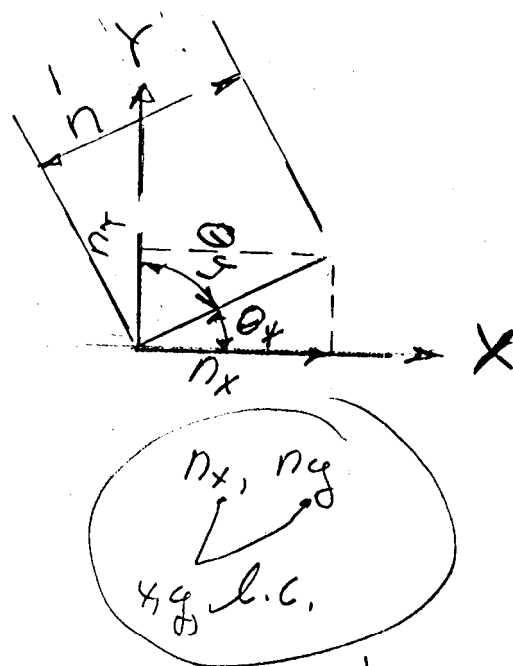


Rod Extension

Figure 3-6



a) Extensions



b) Forces

Figure 3-7

Global Components

Fig 3.8

This is \wpwin\mymemo\ feminch3

Input Data Matrices For MATLAB Finite Element Program

ESSENTIAL DATA

```

nodes      = [nid      1      2      3      4      (5)
               x        y        z        Permanent
               (Optional)
               ..... 1
restr       = [nid      1      2
               component
               (=1 or 2 or 3
               or any combination)
               .....]
rods        = [eid      1      1      3      4
               pid      nid_a  nid_b
               .....]
prop        = [pid      1      2      3      (5)      (6) (7)
               mid      area { amin  amax ex}
               ..... {option.for.des .})
mater       = [mid      1      2      3
               E^2      dens
               .....]
force       = [fid      1      2      3      4      5      6
               nid      factor  fx      fy      fz
               .....]
analyze     = [fid_1    fid_2 ..... fid_n]

```

OPTIONAL DATA

```

force1      = [fid      1      2      3      4      5
               .0.*... ..00.0. .... nid_a  nid_b
               ..... 1
grav        = [fid      1      2      3      4      5
               factor  wx  wy  wz
               (On weight)
               .....]
conwt       = [nid      1      2
               weight
               ..... 1
loadcomb    = [sid      1      2      3      4      (pairs)
               scale  f_1  f_2 ..... fid
               (must be rectangular, fill out with zeros to match largest row)
               ..... 1

```

% July 7, Updated to be in X-Y plane
 % July 9, took some license and replaced "bars" with "rods"
 % June 29, This is CH3BAR.M, 3 bar with sample params Ch:3
 % Jan 29, 1993 THIS IS THREEBAR.M

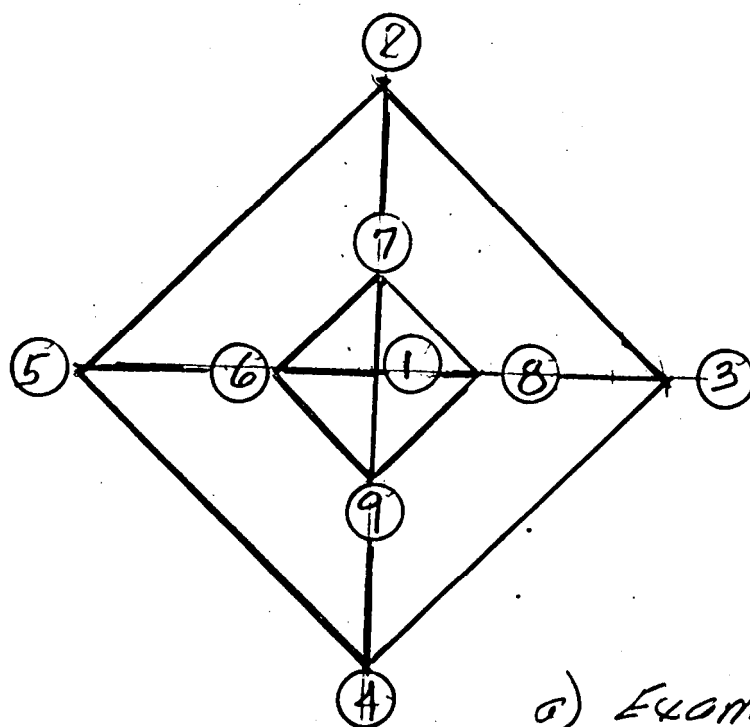
```

nodes=[ 1      0      0      0      3
        2      18     24      0      3
        3      50      0      0      3];
restr=[ 1      12
        3      2];
rods=[ 10      1      1      2
       20      2      2      3
       30      3      1      3];
prop=[ 1      10      2      1.2
       2      10      3.2    1.2
       3      10      4      1.2];
mater=[ 10      1.e+07  1];
force=[ 21      2      2.0e+04      1.      0      0
        23      2      -4.0e+04      0      1      0];
analyze=[21 23];

```

Figure 3-9

Three Bar Truss Problem Input Data



a) Example Structure

	1	2	3	4	5	6	7	8	9	WAVE	BAND
1						X	X	X	X	4	8
2			X		X		X			6	7
3		X		X				X		6	6
4			X		X				X	5	5
5		X		X		X				4	4
6	X				X		X			3	3
7	X	X				X		X		2	2
8	X		X				X		X	1	1
9	X			X		X					

b) Connectivity Matrix

Figure 3-10
Connectivity Counting Example

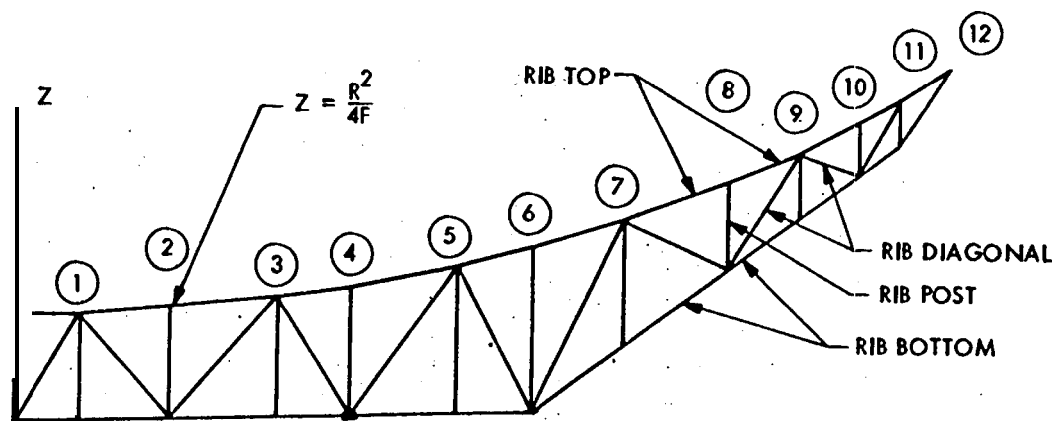
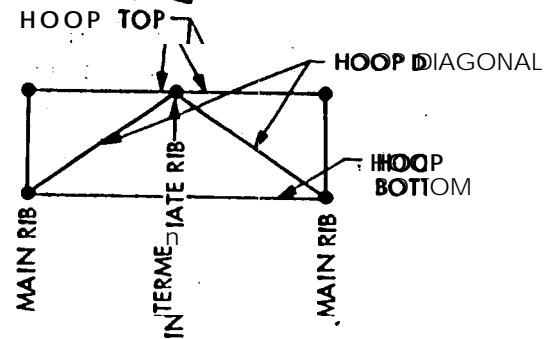
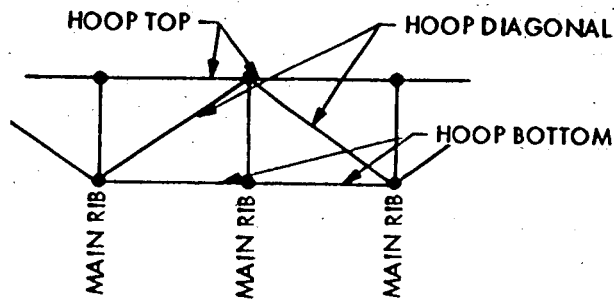
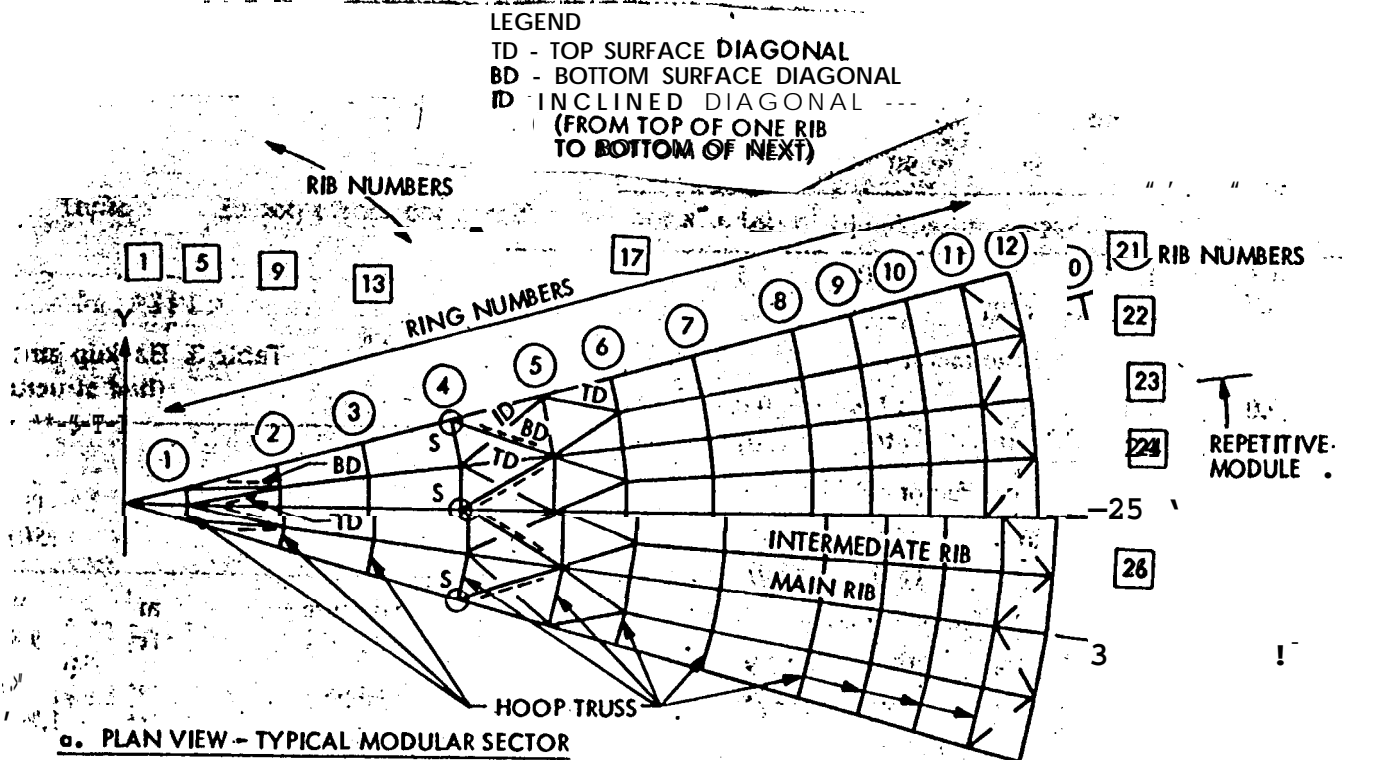


Figure 3-11

Backup structure framing members (Ref 3.19)

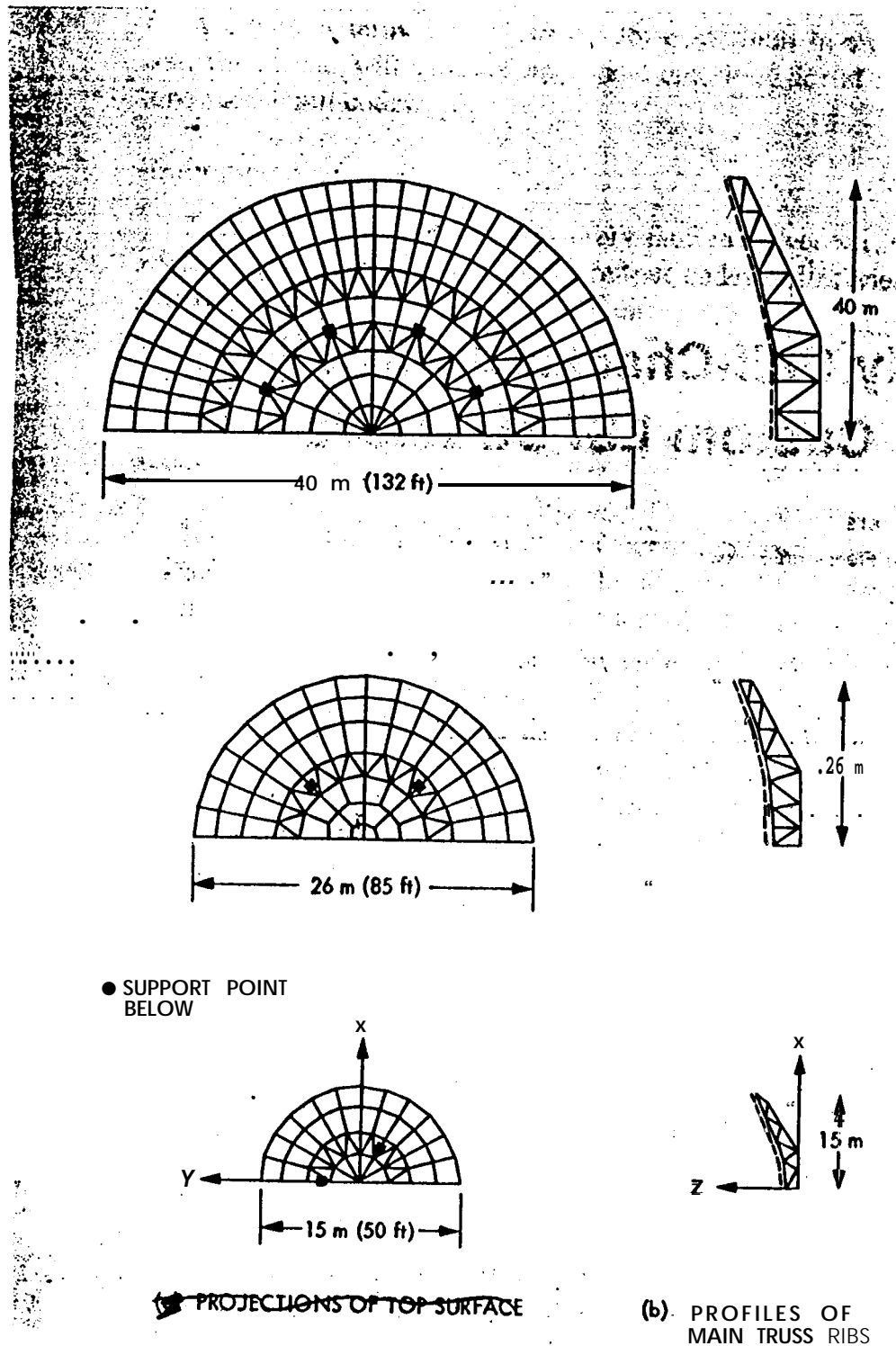
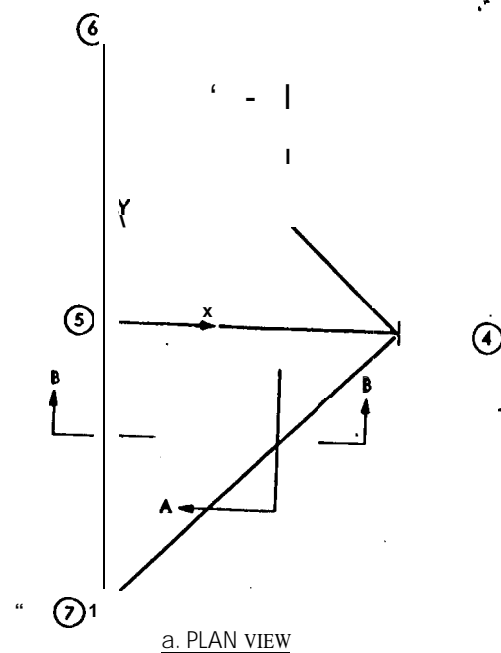
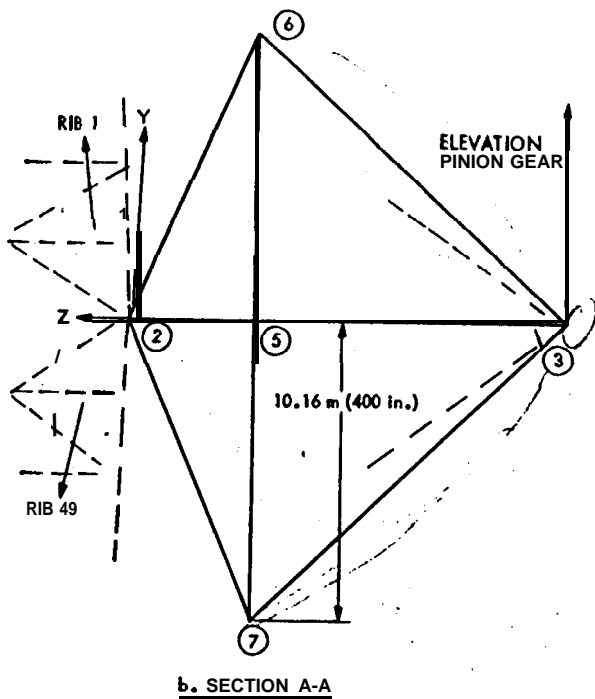
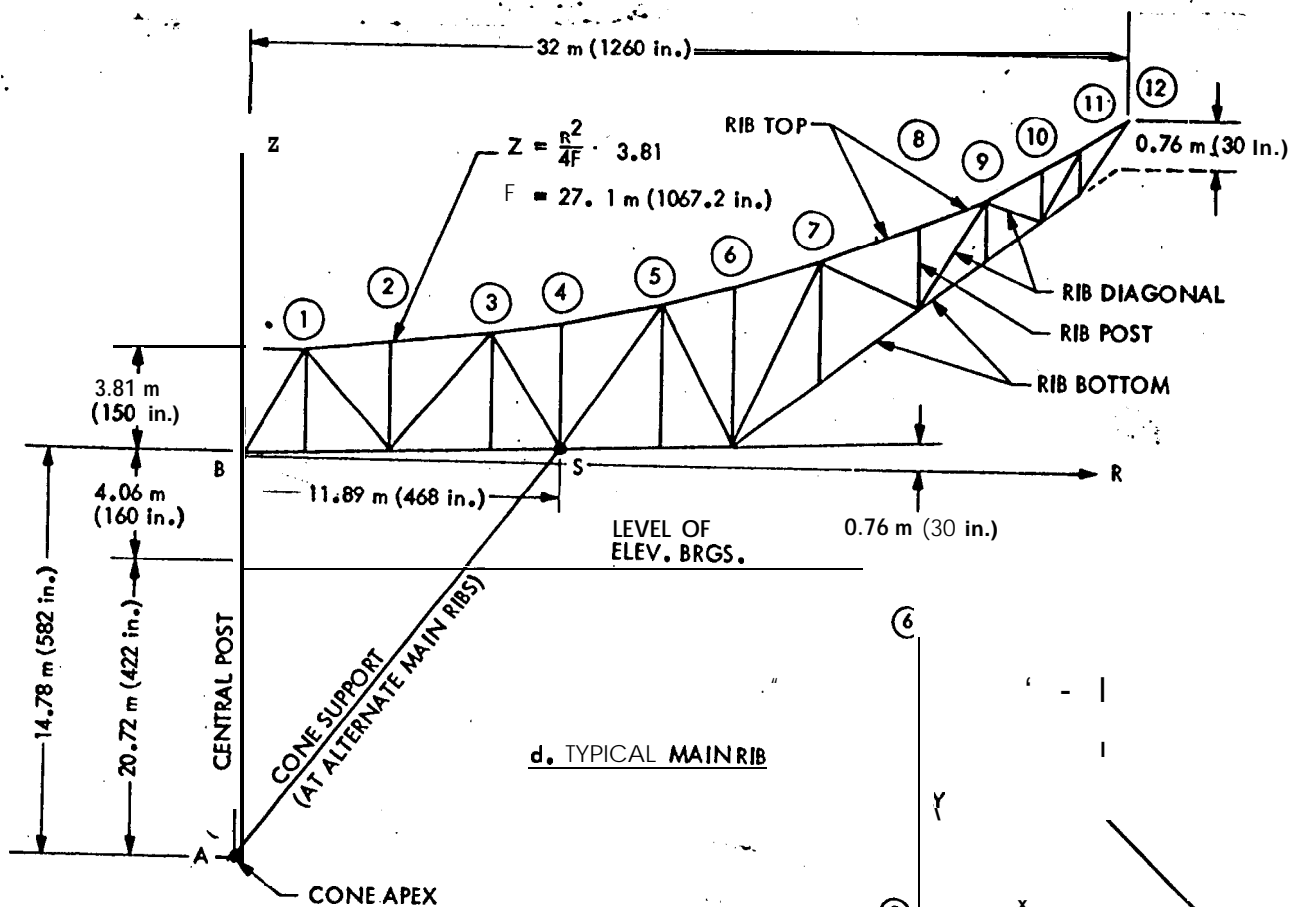


Figure 3-12
Backup Structure Support (Ref [3.19])
Point



SYMMETRICAL

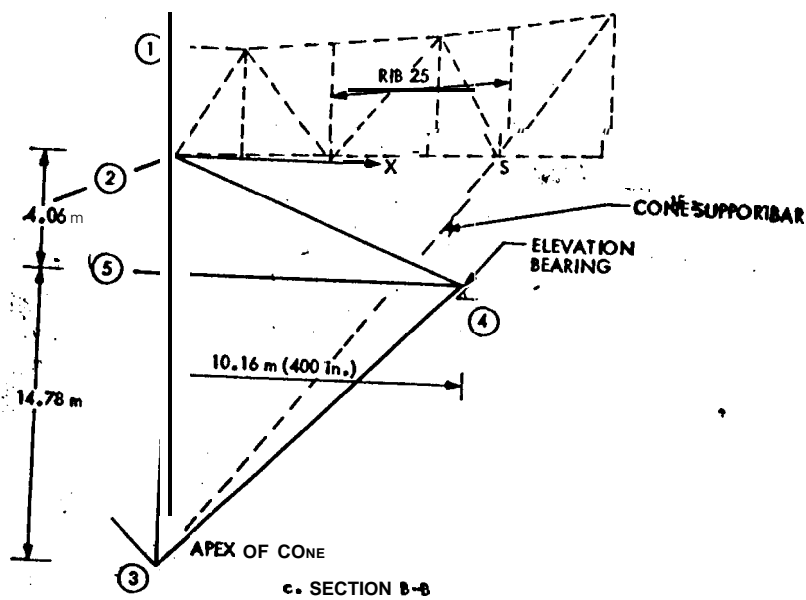


Figure 3-13
Cone Support
For Backup
Structure
(Ref. 2-19)

TABLE 3-1

Data Preparation Notes For Finite Element Structure Analysis

Matrix	Notes	Equivalent NASTRAN Mnemonic
nodes	c.1 nid is an arbitrary label for the node c.2-4 contain the coordinates c.5 any combination of the digits 1,2,or 3 to indicate a restraint in the X, Y, or Z directions(see also <u>restr</u> below)	GRID
restr	c.1 points to a c.1 in <u>nodes</u> c.2 similar to c.5 of <u>nodes</u>	SPC,SPC1 (similar)
rods	c.1 eid is an arbitrary label c.2 property identification, points to a <u>prop</u> matrix identifier c.3-4 the nodes to which the bar is connected,points to various c.1 of <u>nodes</u>	CROD CBAR
prop	c.1 matches a c.2 of <u>bars</u> c.2 points to a <u>mater</u> matrix identifier c.3 area of the rod c.5-7 optional, not used in analysis, but used subsequently in design optimization	PROD PBAR
mater	c.1 matches a c.2 of <u>prop</u> c.2 modulus of elasticity c.3 density, weight per unit volume	MAT1
force	c.1 arbitrary label for the force set c.2 points to a <u>nodes</u> c.1 c.3 multiplier to provide the magnitude of the force, operates on c.4-6 c.4-6 X,Y, and Z components of the force	FORCE
analyze	c.1,2,3, etc. fid's of , <u>force</u> , <u>forc1,grav</u> , or <u>loadcomb</u> set cases to be analyzed	see Case Control

Table 3-1 Cont'd

forcel	c.1 force set label c.2 points to a <u>nodes</u> c.1 c.3 magnitude of force c.4-5 the force is applied from the node of c.4 towards the node of c.5 (see c.1 of <u>nodes</u>)	FORCE1
g r a v	c.1 loading set label c.2 multiplier to provide the magnitude c.3-4 component of weight to be applied in the X,Y,or Z directions This matrix will generate a weight " loading matrix using the volumes of the bars and the densities from the <u>mater</u> matrix	GRAV
conwt	c.1 points to a <u>nodes</u> c.1 c.2 magnitude of a lumped weight at the node to be included with all grav loading sets	CONM2
loadcomb	c.1 loading set label c.2 scale factor to be applied to a loading combination c.3 and following odd columns are scale factors to be used in combining the set identified in the immediate next column c.4 and following even numbered columns are set labels that correspond with <u>analyze</u> matrix cases	LOAD

CHAPTER 4

REFLECTOR SURFACE LOADINGS

The mathematics of the surface pathlength error and the error of the best-fitting parabolic surface were defined in Chapter 2 in terms of the vector of surface deformations. Chapter 3 explained how finite element structural analysis of an analytical model of the structure is used to predict the surface deformations in response to arbitrary loading. This chapter considers the modelling of environmental loads that are applied to the actual structure.

The gravity loading effect is of primary importance because it is always present during the antenna operations. Additionally, the gravity loading is deterministic and can be predicted accurately. The magnitude of this loading, which consists of the weight of the structure and additionally supported parasitic components, is invariant during changes in antenna elevation. Nevertheless, the angle of the gravity loading vector relative to the antenna surface varies with the elevation. This change in the relative direction is responsible for a different set of gravity deformations at each elevation. However, it is possible to reduce the severity of the loading by aligning the surface panels accurately at some elevation angle intermediate between the horizon and zenith pointing directions. The angle chosen for panel setting is called the "rigging" angle (Ref. 4.1). Once the panels are aligned at the rigging angle the effective gravity loading at a particular antenna angle consists only of the change in loading from the rigging angle.

Other important environmental loads are from wind and thermal phenomena. These loads are random and are much harder to characterize than the gravity loading because their occurrence is statistical. Furthermore, although wind and thermal loading of postulated intensity might be considered to occur with some statistical regularity, the spatial distribution of the loading over the surface is not accurately predictable. Beyond this, there could also be significant transient components. Nevertheless, despite some uncertainties, wind tunnel test experiments make it possible to propose models of the "static" wind loading; this is a hypothetical average steady-state condition that has no time dependency. The current knowledge of thermal loading, unfortunately, is more uncertain than that of the wind loading. On the other hand, the transient components of the thermal loading may be less variable than for wind loading.

Additional significant loads to which the antenna can be subjected are from snow, ice, and seismic shock. Antennas are not expected to provide accurate microwave surfaces when

subjected to these environments. Hence the effects of these loadings are ordinarily considered from the standpoint of strength and safety rather than from the standpoint of surface deformations. Snow and ice loadings environments are customarily specified in terms of the layer thickness and weight density. Consequently the magnitude and distribution of these loads can be obtained by direct (although possibly, tedious) calculation. Seismic loading, on the other hand, is stochastic and much more difficult to characterize. Seismic effects will be considered later in the chapter on antenna dynamics.

4.1 Gravity Loading

4.1.1 Pathlength Error At Any Elevation

We are concerned With the computation of the pathlength error from gravity loading at any antenna elevation in the range $0 \leq \alpha \leq 90$. To do this we capitalize on the linearity of the structural response. The starting point is Eq. [2.35], which provides the best-fitting half-pathlength error vector p . The equation is repeated below:

$$p = A U + B H \quad [2.35]$$

However, from Eq. [2.39] the fitting parameters H can be expressed as a linear function of the displacement vector U . It follows then that the best-fitting pathlength error vector is also a constant linear function of the displacement vector, i.e. :

$$H = C u \quad [401a]$$

where the matrix C could be computed from the matrices B , W , and A , and

$$p = R U \quad [4.1b]$$

where $R = A + B C$.

The specific composition of R is shown in Ref. 4.1 (p. 74). It can be constructed, if desired, from matrices of geometry-dependent terms and weighting factors. It is important to note that this is an invariant matrix and is independent of the displacements. Equation [4.1b] also shows that the pathlength errors do not depend explicitly on the fitting parameters H , but rather that H is an explicit function of the displacements that are implicitly represented within R . Equation [4.1b] identifies a linear relationship that makes it possible to simplify all pathlength error computations from gravity and other loading combinations. The method of computation for gravity loading will be shown below. In a subsequent chapter it will also be shown

that the linear relationship between best-fitting pathlength errors and the displacement vector is pivotal to the procedure we have chosen for optimization of the structure design.

It was just shown that the best-fitting pathlength error p is a linear function of the displacement matrix U . The displacements in turn, on the basis of either the Force method (Eq. [3.14]) or the Displacement method (Eq. [3.20]), are linear functions of the external loading. It follows that the pathlength error vector is also a linear function of the loading as indicated below using the Force method for illustration:

$$p = R F P \quad [4.2]$$

where F is the flexibility matrix (adjusted if necessary to account for redundant effects according to Eqs. [3.17] and [3.18)).

It should be noted, however, that in practice it is not customary to form either the matrix R or the matrix F or their product. It is usually computationally more efficient to use the procedures described in Chapter 2 to compute the pathlength error by forming the associated A and B matrices by explicit summations and also by including the weighting factors explicitly. The displacements are almost never generated from a flexibility matrix, but rather are obtained from a finite element analysis that uses the displacement method (Eq. [3.20]) formulation.

Figure 4-1a shows an az-el antenna in the Y - Z plane at an arbitrary elevation. The elevation angle α is defined as the angle of the pointing (Z) axis above the horizon. The positive directions of the Y and Z coordinate axes, which we always take to be fixed to the antenna, are as shown in the figure.

The inset diagram shows that the vertical gravity load w has components of $-w \cos \alpha$ and $-w \sin \alpha$ parallel to the Y and Z axes. At some other reference elevation γ the loading components are $-w \cos \gamma$ and $-w \sin \gamma$. Figure 4-1b indicates the pathlength error curve over the elevation range and how the curve is influenced by a reference rigging angle γ at which there is no pathlength error. Options for rigging angle selection will be considered later in this chapter.

The symbols P_y and P_z are introduced to represent the loading vectors of the total weight (structure plus parasitic)

¹In contrast to the microwave engineering field, it is common for astronomers to refer to the "zenith angle", which is the complement of the elevation angle.

applied in the positive Y and Z axes directions, respectively. At any elevation α the change in loading P_α from the loading at the rigging elevation γ is

$$P_\alpha = [P_Y \quad P_Z] \begin{Bmatrix} \eta \\ \zeta \end{Bmatrix} \quad [4.3]$$

in which

$$\eta = \sin \gamma - \sin \alpha \quad [4.4a]$$

$$\zeta = \cos \gamma - \cos \alpha \quad [4.4b]$$

Substituting Eq. [4.3] in Eq. [4.2] provides the change in pathlength error ρ_α from the pathlength error at the rigging angle as

$$\rho_\alpha = R F [P_Y \quad P_Z] \begin{Bmatrix} \eta \\ \zeta \end{Bmatrix} \quad [4.5]$$

In view of Eq. [4.1b], Eq. [4.5] can be reinterpreted as

$$\rho_\alpha = [\rho_Y \quad \rho_Z] \begin{Bmatrix} \eta \\ \zeta \end{Bmatrix} \quad [4.6]$$

where ρ_Y and ρ_Z are the pathlength errors in response to the loadings P_Y and P_Z .

The change in mean square pathlength error SS_α at elevation α can be computed according to Eq. [2.37] as

$$SS_\alpha = [\eta^t \quad \zeta^t] \begin{bmatrix} \rho_Y^t W \rho_Y / \sum w_i & \rho_Y^t W \rho_Z / \sum w_i \\ \rho_Z^t W \rho_Y / \sum w_i & \rho_Z^t W \rho_Z / \sum w_i \end{bmatrix} \begin{Bmatrix} \eta \\ \zeta \end{Bmatrix} \quad [4.7]$$

The mean square errors for the independent loadings P_Y and P_Z can be recognized in the above equation and identified as SS_Y and SS_Z , respectively. The off-diagonal cross-product term is a covariance and is denoted as S_{YZ} . Therefore Eq. [4.7] can be rewritten as

$$SS_\alpha = [\eta^t \quad \zeta^t] \begin{bmatrix} SS_Y & S_{YZ} \\ S_{YZ} & SS_Z \end{bmatrix} \begin{Bmatrix} \eta \\ \zeta \end{Bmatrix} \quad [4.8]$$

Equation [4.8] provides the mean square error from the gravity loading effect. Ordinarily, we assume that the pathlength error at the rigging angle γ is inconsequential in comparison to the pathlength error effect from the change in loading. If this is the case, then SS_α is the mean square (half) pathlength error at elevation α . A method to include the effect

of the pathlength error at the rigging angle, if necessary, will be discussed later.

Carrying out the multiplications indicated in Eq. [4.8] provides the mean square pathlength error in the form below:

$$SS_{\alpha} = \eta^2 SS_Y + \zeta^2 SS_Z + 2\eta\zeta S_{YZ} \quad [4.9]$$

This equation is of primary importance because it permits calculation of the pathlength error at any elevation in terms of only two pathlength error analyses: the pathlength analyses for the particular loadings P_Y and P_Z .

It is more common practice in the antenna industry to refer to the rms (root mean square "half") pathlength error, which is the square root of the mean square error that has been considered so far in this chapter. The best-fitting procedures provide that the mean pathlength error will ordinarily be either zero or close enough to zero to be ignored. If this is not the case, the weighted mean should be subtracted as discussed in Section 2.4.1. Consequently, the root mean square and the standard deviation will be numerically indistinguishable. Therefore, in the Ruze equation for antenna gain reduction (Eq. [2.3] or [2.4]), the standard deviation symbol σ was used to represent the root mean square. Here, we will assume that the notations " σ " and "rms" are interchangeable in the context of the best-fitting pathlength error vector. Therefore, for the loadings P_Y and P_Z the rms terms are

$$\sigma_Y = \text{rms}_Y = SS_Y^{1/2} \quad [4.10a]$$

$$\sigma_Z = \text{rms}_Z = SS_Z^{1/2} \quad [4.10b]$$

Also, the correlation coefficient CR_{YZ} is defined as

$$CR_{YZ} = S_{YZ}/(\text{rms}_Y \text{rms}_Z) \quad [4.11]$$

Therefore, in terms of the rms pathlength errors for the loadings P_Y and P_Z , Eq. [4.9] can be written as

$$\text{rms}_{\alpha} = (\eta^2 \text{rms}_Y^2 + \zeta^2 \text{rms}_Z^2 + 2\eta\zeta CR_{YZ} \text{rms}_Y \text{rms}_Z)^{1/2} \quad [4.12]$$

The correlation coefficient in the above expression is usually so small that the third term on the right-hand side could be insignificant. In fact, physical reasoning shows that this correlation coefficient is expected to be exactly zero for an antenna that is perfectly symmetrical in construction and weight distribution about the X-Z and Y-Z planes.

The effective loading at any elevation is the net loading shown in Eq. [4.3]. Since displacements are linear functions of the loading, it follows that the fitting parameters at any

elevation H_α can be computed as

$$H_\alpha = [H_Y \quad H_Z] \begin{Bmatrix} \eta \\ \zeta \end{Bmatrix} \quad [4.13]$$

where H_Y and H_Z are the fitting parameters computed for the loadings P_Y and P_Z .

It is important to note that these two loadings in themselves have no real physical significance. Rather, they are mathematical loadings convenient to the foregoing development. They are aligned along positive coordinate axes in accordance with a consistent algebraic sign convention. The inset in Figure 4-1a shows that any real external gravity loading is a negative combination of components of these loads. Furthermore, although it is not difficult to visualize the antenna deformation patterns that could result from the loadings applied in either the Y or Z directions, it is more difficult to visualize the deformation pattern caused by the change in loading (as given in Eq. [4.3]), and it is even more difficult to visualize the net pathlength error vectors after the best-fitting operations (Eq. [2.35]). Attempts to visualize these patterns without taking into account the subtractions with respect to the rigging angle and the effects of the best fitting have occasionally led to confusion.

4.1.2 Rigging Angle Selection

TWO criteria possible for choosing rigging angle are: (a) minimize the maximum rms pathlength error over the elevation range of interest, and (b) minimize the expected average rms pathlength error over the elevation range.

Criterion a:

From Figure 4-1b it can be seen that an intuitive way to minimize the maximum pathlength error is to make the errors at the extreme elevation ranges equal to each other. Then the errors at the extreme elevations become the maximum, and these maxima are smallest when they are equal. It was shown in Ref. 4.1 that for the extreme elevations of 0 and 90 degrees the equalizing rigging angle is

$$Y = \phi - \epsilon \quad [4.14]$$

where

$$\epsilon = \tan^{-1} (B/A) \quad [4.15a]$$

$$\phi = \cos^{-1} (C / (A^2 + B^2)^{1/2}) \quad [4.15b]$$

and

$$A = 2SS_Y - 2S_{YZ} \quad [4.16a]$$

$$B = 2SS_Z - 2S_{YZ} \quad [4.16b]$$

$$C = S_{sy} - SS_z \quad [4.16c]$$

The foregoing procedure will not necessarily minimize the maximum pathlength error. A slightly lower maximum error can be achieved by biasing the error at the rigging angle so that there is a non-zero pathlength error at this elevation. However, in calculations for practical antenna designs the reduction in the maximum error was insignificant. There also was the disadvantage of a finite error in the vicinity of the rigging angle. Consequently, the approach above is recommended as the simplest and most practical.

Criterion b:

We assume that a set of weighting factors H_α represent the probability of the antenna operating at each elevation. Then the rigging angle can be chosen to minimizing the H_α -weighted average pathlength error over the elevation range. It can be shown (Ref. 4.2) that the objective to be minimized is

$$OBJ = a^2 SS_y + b^2 SS_z + 2c S_{yz} \quad [4.17]$$

in which

$$a' = \cos^2 \gamma + \sum H_\alpha \cos^2 \alpha - 2 \cos \gamma \sum H_\alpha \cos \alpha \quad [4.18a]$$

$$b' = \sin^2 \gamma + \sum H_\alpha \sin^2 \alpha - 2 \sin \gamma \sum H_\alpha \sin \alpha \quad [4.18b]$$

$$c = \sin \gamma \cos \gamma + \sum H_\alpha \sin \alpha \cos \alpha - \cos \gamma \sum H_\alpha \sin \alpha - \sin \gamma \sum H_\alpha \cos \alpha \quad [4.18c]$$

and H_α is normalized so that $\sum H_\alpha = 1$.

The expressions for a , b , and c are developed from Eqs. [4.4], [4.9], and [4.17].

For the antenna observations equally distributed over the hemisphere from the horizon to the zenith the weighting is the cosine of the elevation angle. Consequently, the rigging angle could be chosen to minimize the cosine weighted average pathlength error. Observation targets equally distributed over the hemisphere represent a restricted special case, so that the cosine weighted average error is not generally useful..

On the other hand, when antennas are used for specific classes of missions, such as for spacecraft communications, it is possible to derive statistics for typical missions and develop weighting factors for the associated elevation angle range. One study of a set of about 15 planetary spacecraft missions during an 8-year period was described in Ref. 4.2. A set of average declination angles from the spacecraft missions was assembled and a set of declination angle weighting factors was computed on the basis of the time spent at these declinations. The declination

angle weighting factors were used to compute elevation angle weighting functions (probability densities) by means of the HA-dec to az-el conversion equations described in Chapter 1, section 1.4.1.

It was also suggested that these spacecraft missions traveled in orbits similar to an ecliptic orbit. A set of elevation angle statistics was developed for a sun-tracking orbit to test this suggestion. As suspected, it was found that the elevation angle probability statistics of both types of missions were similar. Consequently, the simplicity of the analysis for the solar mission made this a convenient way to estimate the weighting factors. The solar mission weighting factors are shown in Table 4-1. Figure 4-2 shows the probability density function of elevation angles for solar missions as determined from the weighting factors, and Figure 4-3 shows the cumulative probability distribution functions. The latitude of the ground antenna for these figures was 35.4 degrees. Figure 4-2 shows that the elevation of about 32 degrees predominates and Figure 4-3 shows that the antenna elevation is less than this about 50% of the time.

The weighting factors are substituted into Eqs. [4.18] to form the objective of Eq. [4.17]. Then γ can be chosen by a numerical search method to minimize the objective such as by the method of false position, binary search, golden section search, or trial and error search. As a specific example, analysis for the Deep Space Network 64-m Mars antenna at Goldstone, California via the golden section method provided an optimum rigging angle of about 35 degrees. Figure 4-4 shows the elevation angle range performance for the Mars antenna at 8.45-GHz frequency for the optimum and the 45-degree rigging angles. The weighted average gain reduction (Eq. [2.4]) over the elevation range is improved by about 20% with optimum rigging. Specifically, the optimum *rigging* angle improves the performance at low elevations and degrades the performance at the higher elevations, which is consistent with the probability functions of Figures 4-2 and 4-3.

4.2 Wind Loading

The surface wind loading on each region of a structure is equal to the product of the surface pressure, the area of surface exposed to the pressure, and one or more coefficients that depend upon both air flow characteristics of the surface and directional coefficients of forces acting on the surface. The pressure is usually taken to be the stagnation pressure, which is the pressure developed when the wind speed is reduced to zero. The flow characteristic coefficients, although theoretically computable from complex fluid mechanics relationships (Ref. 4.3) , are more practically obtainable by wind tunnel model tests

(Ref. 4.4).

There is widely available literature (Refs. 4.5, 4.6) that considers practical aspects of the static wind loading, predominantly upon on building, rather than antenna, structures. The emphasis is usually on overall loading coefficients for the entire configuration. For example the drag force on a structure is computed as the product of a drag coefficient, the stagnation pressure, and the frontal area of the entire surface exposed to the wind. Lift forces, side forces, and moments are computed for the entire structure similarly from lift force, side force, and moment coefficients. These coefficients are useful in determining the loading at particular story levels or at the foundations of Civil Engineering structures, for example. They are also useful in obtaining the forces and moments at the axes of antennas for the design of drive train motors, bearings, and gears.

Nevertheless, the analysis of the microwave accuracy of the antenna surface depends upon the spatial distribution of surface wind pressure coefficients. Pressure coefficients vary significantly over the surface. They usually are applied to small individual areas (typically the size of each reflecting surface panel). Products of tributary surface areas, wind pressures, and pressure coefficients provide the means to compute the forces at nodes of the finite element model. These forces are the inputs for the processes of deformation analysis, pathlength error computations, and least-squares best-fitting as described in Chapters 2 and 3. In a sense, surface pressure coefficients can be viewed as micro-scale phenomena, while the overall drag, lift, side force, and moment coefficients can be viewed as macro-scale phenomena. Of course, the macro-scale coefficients could ideally be obtained through integrations that employ the micro-scale components.

4.2.1 Stagnation Pressure Relationships

The Bernoulli model for the stagnation wind pressure q on an exposed surface is

$$q = \frac{1}{2} \rho v^2 \quad [4.19]$$

in which ρ is the air mass density and v is the wind speed. This stagnation pressure is the differential pressure above the ambient. It balances the kinetic energy lost by arresting the motion of a unit volume of the air fluid.

In conventional English units and under standard atmospheric conditions of 60°F and of 14.7 lbs/inch² (psi) atmospheric pressure, the air density is 0.002378 slug/ft³. Equation [4.19]

applies with v expressed in feet/s. In practice, it is conventional to express the speed in miles/hour (mph) as V . Therefore

$$v(\text{ft/s}) = (5280/3600)V \text{ (mph)} \quad [4.20]$$

Then

$$q = .00256 V^2 \quad [4.21]$$

and here q is in lbs/ft^2 (psf).

The following factors can be used to convert to SI units:

1 lb force (lbf)	=	4.448 newtons (n)
1 foot (ft)	=	0.3048 meters (m)
1 slug	=	14.593 kilograms (kg)

Then the air density ρ_{SI} in kg/m^3 is

$$\rho_{SI} = 0.002378 \times 14.593 / (0.3048)^3 = 1.2255 \text{ kg/m}^3$$

and Eq. [4.19] will give the pressure in newtons/m^2 with this value of the air density and with the speed in meters/second.

The air density can vary significantly with the site altitude. For example, a specific computation in Ref. 4.7 shows the density at elevation 3500 feet (1070 m) is only 8.7% of the density at sea level. The procedure in this reference can be extended to provide a generalized, rational algorithm to estimate the variation of air density with altitude. To make the estimate, we have the equation of state for a perfect gas which implies a constant relationship between pressure, volume, and temperature. The relationship is

$$PV/T = R = \text{constant} \quad [4.22]$$

P is the atmospheric pressure, V is the specific volume (volume of a unit of mass), and T is the absolute temperature (degrees rankine in English units, degrees kelvin in SI units). Letting P_0 , V_0 , and T_0 represent the reference pressure, volume, and temperature at the standard conditions, the volume at some other condition can be found from

$$v = (P_0/P) (T/T_0) V_0 \quad [4.23]$$

The weight density γ is inversely proportional to the specific volume so that Eq. [4.23] can be converted to

$$\gamma = (P/P_0) (T_0/T) \gamma_0 \quad [4.24]$$

where γ_0 for air at standard conditions is $0.002378 \times 32.17 = 0.0765 \text{ lbs/ft}^3$. A temperature-elevation gradient (Ref. 4.7) can be estimated as

$$T = T_0 - \beta Z \quad [4.25]$$

in which β is equal to 0.0035°F per foot of height (above sea level) and Z is the height in feet. A rational estimate for the atmospheric pressure at height Z is to assume that the change in pressure depends approximately upon the weight of the column of air from height $Z=0$ to height Z . This change in weight can be computed as the product of the average of the density at sea level and the density at the height Z and the height itself. Then the pressure P_0 in lbs/in^2 at height Z can be estimated as

$$P = P_0 - Z (\gamma + \gamma_0) / 2 / 144 \quad [4.26]$$

Substituting Eqs. [4.25] and [4.26] in Eq. [4.24] provides the ratio of the air density at height Z to the density at sea level in the form

$$\gamma/\gamma_0 = N/D \quad [4.27]$$

where $N \approx 1 - \gamma_0 Z / (288 P_0)$

and

$$D = 1 - \beta Z / T_0 + \gamma_0 Z / (288 P_0) \quad [4.27b]$$

Figure 4-5 shows a plot of Eq. [4.27] for elevations up to 25,000 (7,620-m) feet above sea level. The points marked by asterisks are from the Dept. of Commerce U.S. Standard Atmosphere as reported in Ref. 4.8. The agreement of the curve with the Standard Atmosphere is close enough to suggest that similar methods of computation may have been used.

4.2.2 Surface Pressure Coefficients

Reference 4.9 is one of only a few substantive reports on the wind tunnel determination of antenna surface pressure coefficients. This report provides the data from pressure transducers that were applied at 22 locations distributed over the surface of thin half-meter-diameter paraboloidal shells. The focal length-to-diameter ratio of the shells was 0.33. Several shells of different porosities were tested. Here, we will consider only the shell with solid surface. The porous shells had specific porosity and hole size factors that restrict generalization to other porosity configurations.

Five sets of data from the reference are provided in Figure 4-6. These simulate antennas with solid surfaces at elevations of 0, 60, 90, 120, and 180 degrees. The first three cases represent wind into the front of the antenna. The second two are equivalent to the elevations of 60 and zero degrees with the wind from the back. No side winds are considered, although symmetry at the 90-degree elevation would allow this case to apply to every wind azimuth. The radii are normalized to a unit diameter. The column heading angles are measured from the top (Y axis) of the antenna. These angles cover only the half of the antenna to one side of the Y-Z plane. Symmetry can be used to derive the other half because the wind is always either directly from the front or the back.

Contour maps determined from the data are shown in Figure 4-7. The appearance of symmetry about the vertical axis is really an artifice of the procedure invoked to produce the contours. That is, contours for the full antenna were developed by reflecting one side of the antenna about the Y-Z plane. A 40-by-40 X-Y grid was established as a basis for bilinear interpolation from the original wind tunnel measurement data. When evaluating the appearance of these contours (or in fact, any other data derived from the wind tunnel data), it should be recognized that there were only 22 measurements points in each wind tunnel configuration. Furthermore, fine details of contour maps depend upon the interpolation algorithms employed.

4.2.3 Wind Force Data For Computer Analysis

The data in Figure 4-6 has been used as the basis of interpolation to provide wind force loading data for the finite element analysis of antenna structure models. Appendix 4A contains a MATLAB program, WINDTUNL.M, that will provide a file of force-loading FORCE card image records (Table 3-1) that can be input to the NASTRAN program (Ref. 3.7). The user is required to supply basic antenna parameters of diameter and focal length. The particular antenna surface is described in an 8-column input matrix. The rows contains the node labels, a coordinate system flag, the X, Y, and Z coordinates of the node, and a weighting factor that represents the relative surface area tributary to the node.

The coordinate system flag provides the option of representing the antenna in a cylindrical coordinate system as an alternative to providing the X and Y coordinates in the standard antenna coordinate system (defined previously in Chapters 1 and 2). A pre-defined cylindrical system is employed in which angles are measured clockwise from the Cartesian Y axis, the X coordinate in the input matrix is replaced by the radius, and the Y coordinate is replaced by the angle (in degrees). The input Z coordinates are not used, but instead are recomputed by the

program from the parabolic equation so that the Z coordinate at the vertex is zero.

The program prompts the user for input and contains default values as well as comments for clarification. The output, in addition to a file of FORCE cards, includes the sum of the forces in the X, Y, and Z coordinate directions and the moment about the X axis at the vertex.

The algorithms consist of interpolating the pressure coefficients to the nodes of the structure, computing the wind pressure from the speed (Eq. [4.19]) to obtain the force per unit area, and then determining the area tributary to the nodes by means of the weighting factor and the diameter. The surface force magnitude at the node is then the product of the tributary area, the pressure coefficient, and the stagnation pressure. The direction cosines at the surface are developed (Eqs. [2.19]) to provide the orientation of the force vector. The total surface and projected areas are byproducts available from these computations.

4.2.4 Wind Speed Profile

A well-known characteristic of wind is the variation of the speed with the height above the ground. This variation is called the velocity profile. Speeds are lowest near the ground and increase with height within the boundary layer. The boundary layer is several hundreds of meters above the surface, so that ground-based antennas will normally be within the boundary layer. The speed becomes constant above this height.

The speed-height relationship conventionally adopted in civil engineering practice provides a power law function to express the speed V_A at height Z_A in terms of the speed V_0 at a reference height Z_0 as follows:

$$V_A/V_0 = (Z/Z_0)^\alpha \quad [4.28]$$

The power law exponent α is usually taken as 1/7 for open terrain, 1/10 over water, 1/4.5 in suburban areas, and 1/3 in cities. The value of 1/7 is likely to predominate for ground antenna sites. The boundary layer height in which Eq. [4.28] can be used is 275 m for $\alpha = 1/7$ and 210m for $\alpha = 1/10$. The boundary layer is higher for the other two categories. The reference height is often taken as 10 m or 33 feet.

The logarithmic law (Refs. 4.3, 4.5, 4.6) provides another expression for the wind speed profile. It invokes three parameters to describe the speed variation and is developed from micro-meteorological theory. Nevertheless, both the power law

and logarithmic law provide similar--actually almost indistinguishable--profiles at the usual antenna heights. Since neither law provides an exact representation for every physical situation, the power law is preferred because, in the absence of site data, the single parameter α can be estimated according to the rules of the preceding paragraph.

Reference 4.7 tabulates several months of wind speed data for three different heights recorded at hourly intervals at Goldstone, California in 1966-67. An instrumented tower had anemometers at the 50-, 150-, and 300-foot levels. Triplets of data for the three levels were averaged for 5-minute periods taken on the hour. The data triplets were closely indicative of the speeds at simultaneous times for the three heights. Ten months of data were available to provide comparisons for the three heights and the data was pooled into monthly averages; thus 10 months of average speed data and three heights provide thirty monthly averages. There were a total of about 4000 hourly samples for each height. The value of α found by regression was 0.1405 and the standard deviation was 0.0193. Figure 4-8 shows a plot of the ratios of the individual monthly average speeds at the 150- and 300-foot heights to the speeds at the 50-foot height. The speed ratios are plotted on a semi-log scale. The power law line is plotted using the regression value of α . The evident scatter of the data with respect to the regression line makes the choice of power law or logarithmic law seem to be immaterial.

4.2.5 Extension of Wind Tunnel Data to Other Wind Attitudes

If the wind tunnel tests that produced the data of Figures 4-6 and 4-7 were free of tunnel wall and boundary effects, the data would have been homogeneous and could have been extrapolated to provide data for variations in wind azimuth (yaw) in addition to antenna elevation. In that case the wind tunnel data would apply to the compound azimuth-elevation wind angle with respect to the antenna axis. To be specific, if we now let α represent the antenna elevation angle, and A represent the wind azimuth relative to the antenna, the antenna Z axis can be represented by the vector \mathbf{Z}_a as

$$\mathbf{Z}_a = [0 \quad -\cos \alpha \quad \sin \alpha] \quad [4.29a]$$

The wind vector \mathbf{W} impinging on the antenna can be represented by

$$\mathbf{w} = [-\sin A \quad \cos A \quad 0] \quad [4.29b]$$

The cosine of the compound angle ϕ between the wind and the antenna is the inner product of \mathbf{Z}_a and \mathbf{W} :

$$\phi = \cos^{-1} (\cos \alpha \cos A)$$

[4.30]

Figure 4-9 shows contour lines of the magnitude of the compound angles that occur for various combinations of antenna elevation and wind azimuth. Depending upon the validity of two assumptions, contours such as these would make it possible to determine wind pressures for the full spectrum of elevation and wind azimuth angles. The assumptions are:

- (1) The wall and boundary effects of the wind tunnel did not interfere significantly with homogeneous air flow.
- (2) It is reasonable to interpolate the wind tunnel pressure data for elevations intermediate to those at which the wind tunnel measurements were taken.

Neither of these assumptions can be strictly justified. The first assumption can be seen to be inaccurate in view of Figure 4-7a. Here, it is evident that the pressure lines are not symmetrical about a horizontal diameter. In fact, it has been suggested that the particular wind tunnel setup may have employed unsymmetrical screens to produce a velocity profile as in Eq. [4.28] with $\alpha = 0.14$. The second assumption has yet to be tested. We once attempted the drastic interpolation between the 0-degree and 90-degree elevation data to see if there was agreement with the measured 60-degree data. The results of the interpolation were not encouraging. Nevertheless, if it is essential to have wind pressure distribution data in addition to the five cases of Figure 4-7, the analyst may have no other choice than to interpolate for the needed data and to accept the consequences of the weaknesses of the above two assumptions.

4.2.6 Integration of Pressure Coefficients

The wind forces determined by summing the finite element nodal loading generated (as described, for example, in Section 4.2.3) can be compared with wind tunnel force-balance data from a number of independent wind tunnel antenna model tests. The force-balance data usually provides the six generalized forces (the three forces and the three moments with respect to the three orthogonal axes) for the complete structure model that is being tested. Force-balance data is more easily obtained than the pressure distribution data and hence there is much more data available, and it is usually much more detailed with respect to the antenna elevation-wind azimuth spectrum. The data is used to design the mechanical system of pinions, gears, and drive motors, and to establish the loadings on the antenna pedestals, mounts, and foundations. Depending on the coordinate system in which the data is collected, the data can be used to derive the conventional lift, drag, and side force coefficients and the

pitch, roll, and yaw moments.

Reference 4.10 provides tables of force-balance data assembled as the compilation of a number of wind tunnel testing programs. There are four sets of data that cover several surface porosity and focal length-to-diameter ratios. The antenna elevation and wind azimuths are tabulated from 0 to 180 degrees at 5-degree increments. A condensed set of data for the solid surface with a focal length-to-diameter ratio of 0.313 is reproduced in Appendix 4B. The coordinate system for this set of data is shown in Figure 4-10. The antenna forces are computed as the product of the tabulated force coefficients, the aperture area, and dynamic pressure. The moments are computed as the product of the moment coefficients with the aperture area and diameter and dynamic pressure. That is:

$$\begin{aligned}\text{force} &= c_f A q \\ \text{moment} &= c_m A D q\end{aligned}$$

where c_f and c_m are the tabulated force or the moment coefficients, A is the reflector area, D is the diameter, and q is the stagnation pressure.

Reference 4.11 provides an additional compilation of wind tunnel force-balance data from a number of sources. This reference shows agreement in some cases and scatter in others when data from differing sources are plotted for comparison.

Figure 4-11 shows a plan view of the right-half top surface nodes of a hypothetical 30-foot-diameter antenna. The normal, axial, and pitching moments were computed from the coefficients in Appendix 4B and the computations outlined in Table 4-2. Wind force loading data was also generated for this antenna by the procedure and program described in Section 4.2.3, and the normal, axial, and pitching moments obtained by summing the data of the FORCE loading records are also recorded in the table for comparison. Table 4-3 shows the same type of information for a 132-foot-diameter (40-m) antenna.

Tables 4-2 and 4-3 show that agreement of the forces from the two computational approaches is best when the force magnitudes are the largest. When the magnitudes are small, the forces do not even always agree in sign. The pitch moment agreement is also irregular, and there is also disagreement in some of these signs. When proceeding below the vertex of the antenna downwards towards the foundation, the disagreement in moments is likely to become smaller because the effect of the vertex forces will predominate at these distances. Disagreements of the integration method with the force-balance method is not surprising in view of the independent wind tunnel tests, possible differences in wall and boundary layer effect differences, speed-height profiles, differences in the focal length-to-diameter

ratios of the models, and the limitations of interpolating over the surface from only 22 pressure tap locations.

4.3 Thermal Loading

The distribution of temperature over the structural members of the antenna causes thermal distortions of the members and changes the shape of the surface. If the temperatures at the nodes of the model or the average temperatures of members of the model are known, finite element computer models can predict the deformations, and hence the surface errors. Unfortunately, there are almost no successful measurement data available to establish the actual temperature distributions for an antenna structure. In the absence of substantive data, it has been the practice to perform a few rudimentary estimates of temperatures and extrapolate these into arbitrary distributions for computer analysis. As an alternative, an accurate and practical analytical procedure that would incorporate thermal conductivity, convection, radiation, and re-radiation appears to be out of the reach of current technology because of overwhelming complexity, uncertainty in physical parameters, and requirements for computer resources.

A few infrared camera measurements (Ref. 4.12) made in the 1980s provide an exception to the lack of actual field data. A 34-m antenna was monitored in the field by an imaging infrared camera during a tracking mission. A spacecraft was tracked in a sidereal orbit so that a sun angle of about 25 degrees with the antenna axis was approximately constant during the experiment. Colors recorded by the camera were processed to provide a close estimate of the actual temperatures of the structure. Figure 4-12 is a black and white reproduction of the color photograph camera record. Celsius temperatures obtained through processing the camera record are printed in white ink. The darker regions near the rim of the dish are attributed to the cold temperature of the sky that appeared because the outer surface panels were perforated. The relatively small range of temperatures that were recorded are attributed to high-reflectance white paint that controls temperatures of antenna metals exposed to direct sunlight. Unfortunately, the resources were not available to continue this measurement program.

Infrared camera measurements could be automated to provide spectra of distributions of actual antenna temperatures for various environmental conditions. These distributions could be used for finite element analysis of surface accuracy. Field camera measurements are more authentic than wind tunnel experiments because measurements are obtained for the full-sized prototype under service conditions, rather than for scale models under simulated conditions. It is also feasible to measure temperatures at many more points than are practical for wind

tunnel pressure instrumentation.

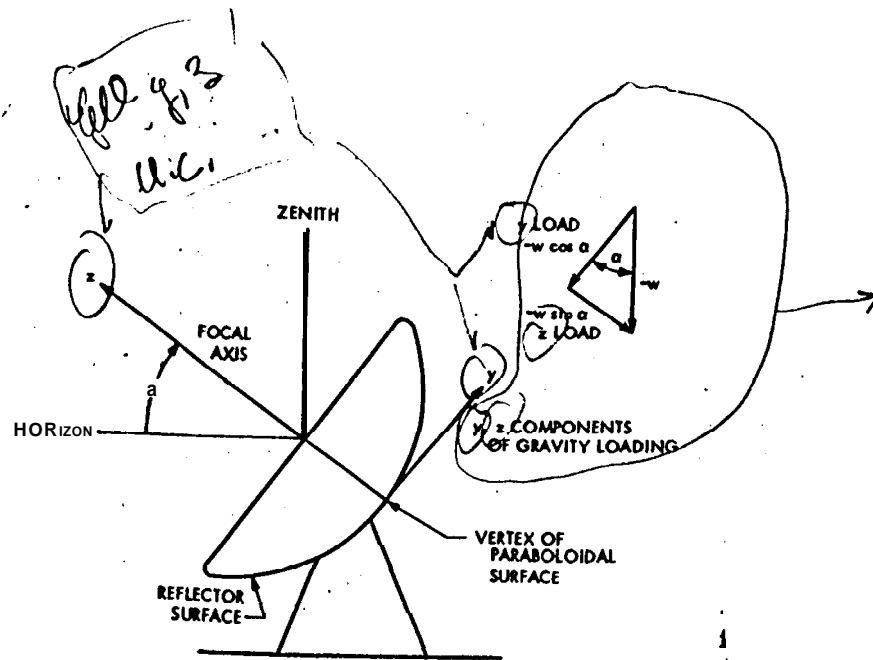
REFERENCES

- 4*1 Levy, R., "A Method of Selecting Antenna Rigging Angles to Improve Performance," Space Programs Summary 37-65, Vol. II, Pasadena, CA: Jet Propulsion Laboratory, California Institute of Technology, Sept. 30, 1970, pp. 72-76.
- 4.2 Levy, R. , "Antenna Bias Rigging for Performance Objective," presented at the IEEE 1977 Mechanical Engineering in Radar Symposium," Arlington, VA, Nov. 8-10, 1977.
- 4.3 Simui, E., and Scanlan, R. H., Wind Effects on Structures: An Introduction to Wind Enaineering, 2nd Edition, NY: Wiley Interscience Publication, John Wiley & Sons, 1986.
- 4.4 ASCE Task Committee, Wind Tunnel Model Studies of Buildings and Structures, NY: American Society of Civil Engineers, 1987.
- 4.5 ASCE Task Committee, Wind Loading and Wind-Induced Structural Response, NY: American Society of Civil Engineers, 1987.
- 4.6 Liu, H., Wind Enaineerina: A Handbook for Structural Engineers, Englewook Cliffs, NJ: Prentice Hall, 1991.
- 4.7 Levy, R., and McGinness, H., "Wind power prediction Models," Technical Memorandum 33-802, Pasadena, CA: Jet Propulsion Laboratory, California Institute of Technology, Nov. 15, 1976.
- 4.8 Marks' Standard Handbook for Mechanical Engineers, Eighth Edition, Baumeister, T, and Avallone, E. A. , Eds. , NY: McGraw-Hill Book Company, 1979.
- 4.9 Fox, N., L., "Load Distributions on the Surface of Paraboloidal Reflector Antennas," Internal Memorandum CP-4, Reorder No. 62-710, Pasadena, CA: Jet Propulsion Laboratory California Institute of Technology, July 1962.
- 4.10 Levy, R., and Kurtz, D., Compilation of Wind Tunnel Coefficients for Parabolic Reflectors, JPL Publication 78-16, Pasadena, CA: Jet Propulsion Laboratory, California Institute of Technology, April 15, 1978.
- 4.11 Sheard, W. B., and Winters, J. L., Final R&D Report on Wind Loading of Parabolic Antenna, Contract No. 8902, E-Systems, Inc. , Jan. 10, 1972.
- 4.12 Glazer, S., and Gale, G., "Thermal Measurement Technique of Rib Elements on DSN Antenna Structure," TDA Proaress Report 42-66: September and October 1981, Pasadena, CA: Jet

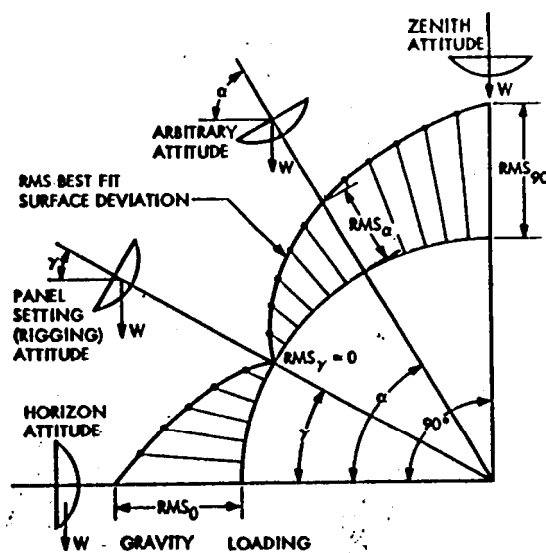
Propulsion Laboratory, California Institute of Technology,
Dec. 15, 1981, pp. 67-79.

FIGURES

- 4-1 Gravity Loading on Antenna: a) Loading Components; b) Pathlength Error vs Elevation
- 4-2 Density Function, 34.4°N Latitude
- 4-3 Distribution Function, 35.4°N Latitude
- 4-4 Mars Antenna Rigging Angle Performance Alternatives
- 4-5 Variation of Air Density with Height
- 4-6 Antenna Surface Pressure Coefficients
- 4-7 Antenna Wind Pressure Contours: a) 0-deg elevation; b) 60-deg elevation; c) 90-deg elevation; d) 120-deg elevation; e) 180-deg elevation
- 4-8 Wind Speed vs height
- 4-9 Elevation and Azimuth to Produce Compound Angles
- 4-10 Wind Tunnel Force-Balance Coordinates
- 4-11 Top Surface Pads, 30-ft-diameter (Half) Aperture
- 4-12 Infrared Camera Measurements



a) Loading Components



b) Pathlength Error Vs Elevation

Figure 4-1
Gravity Loading on Antenna

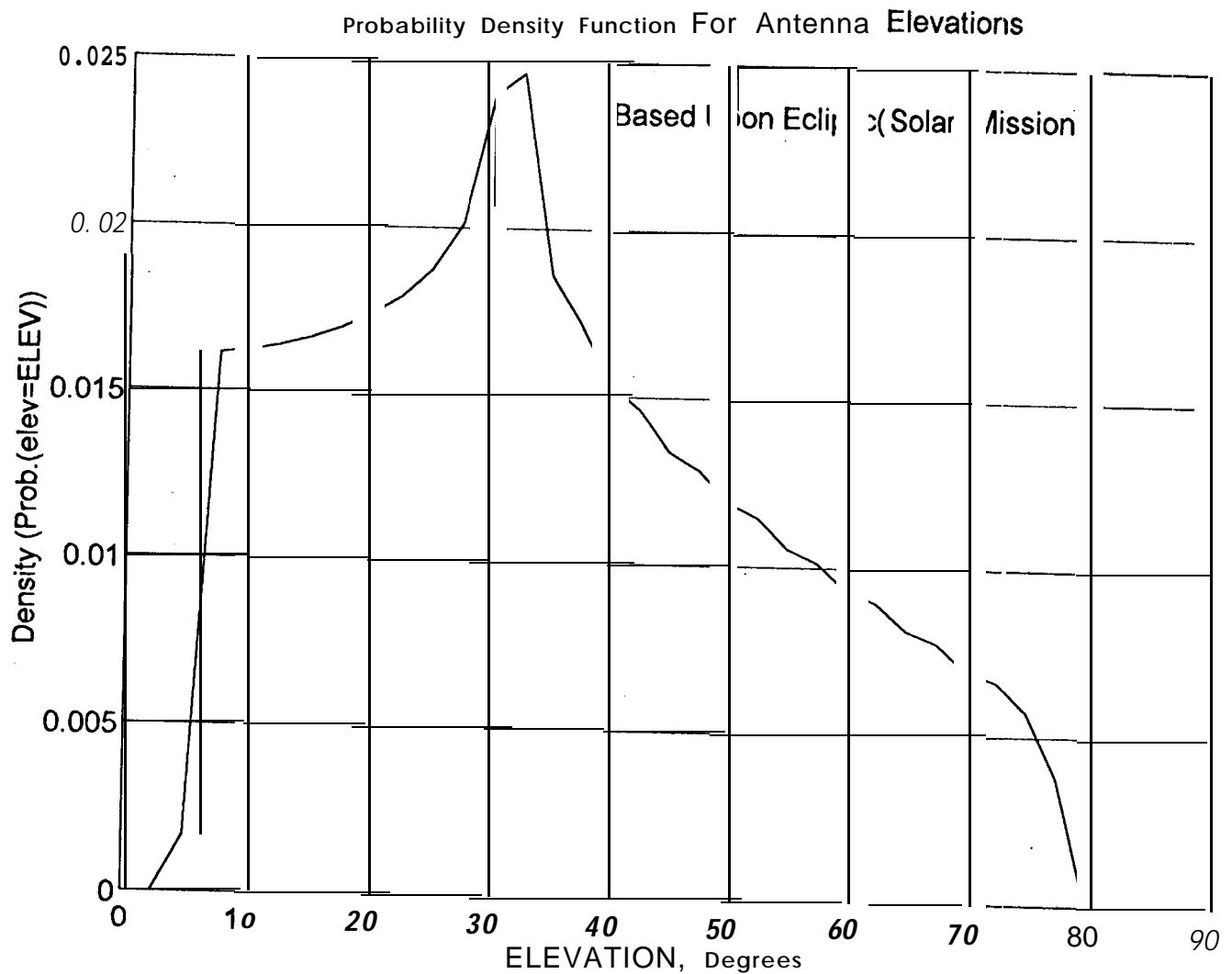


Figure 4-2
Density Function
34.4 Degree N. Latitude

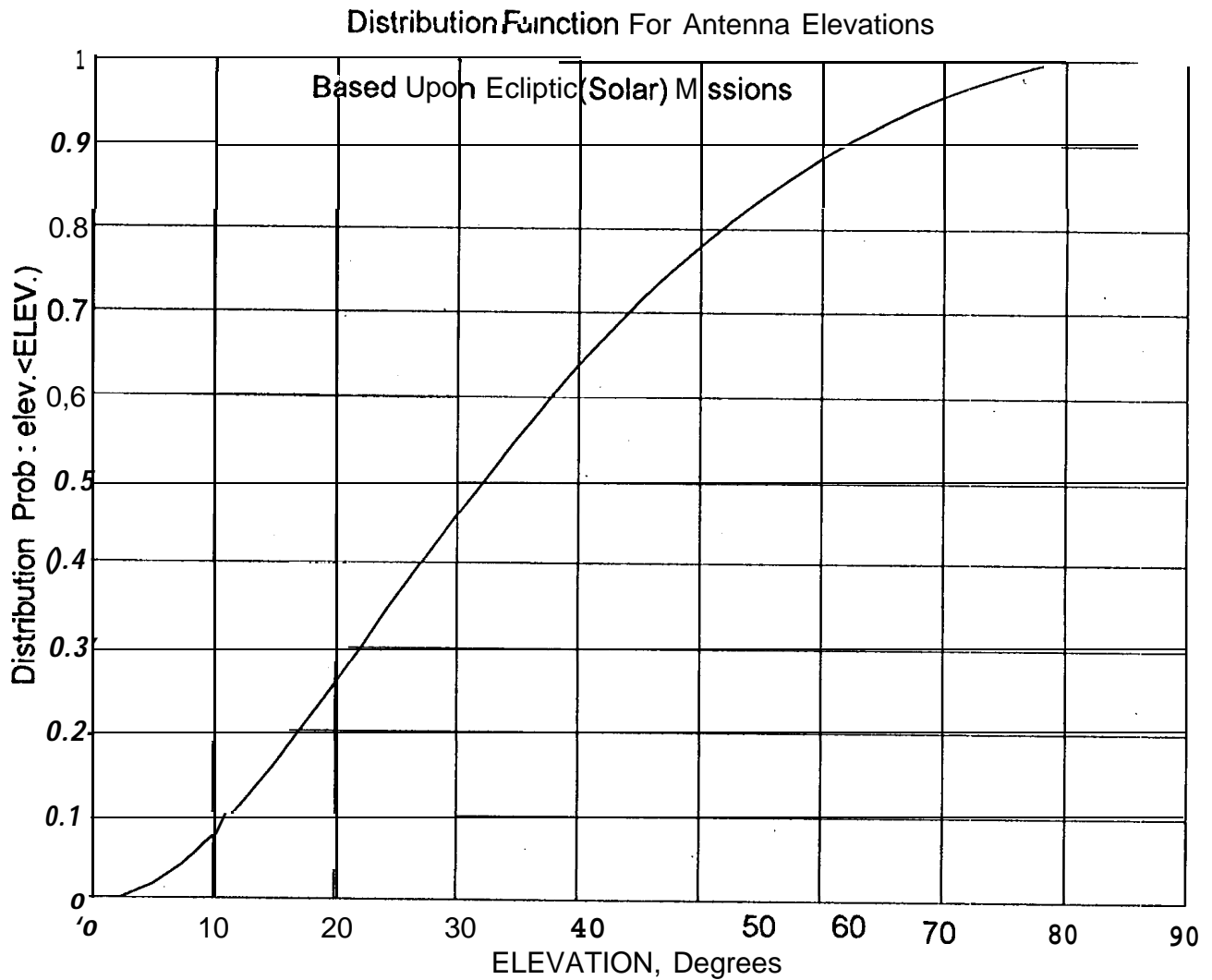


Figure 4-3
Distribution Function
35.4 Degree N. Latitude

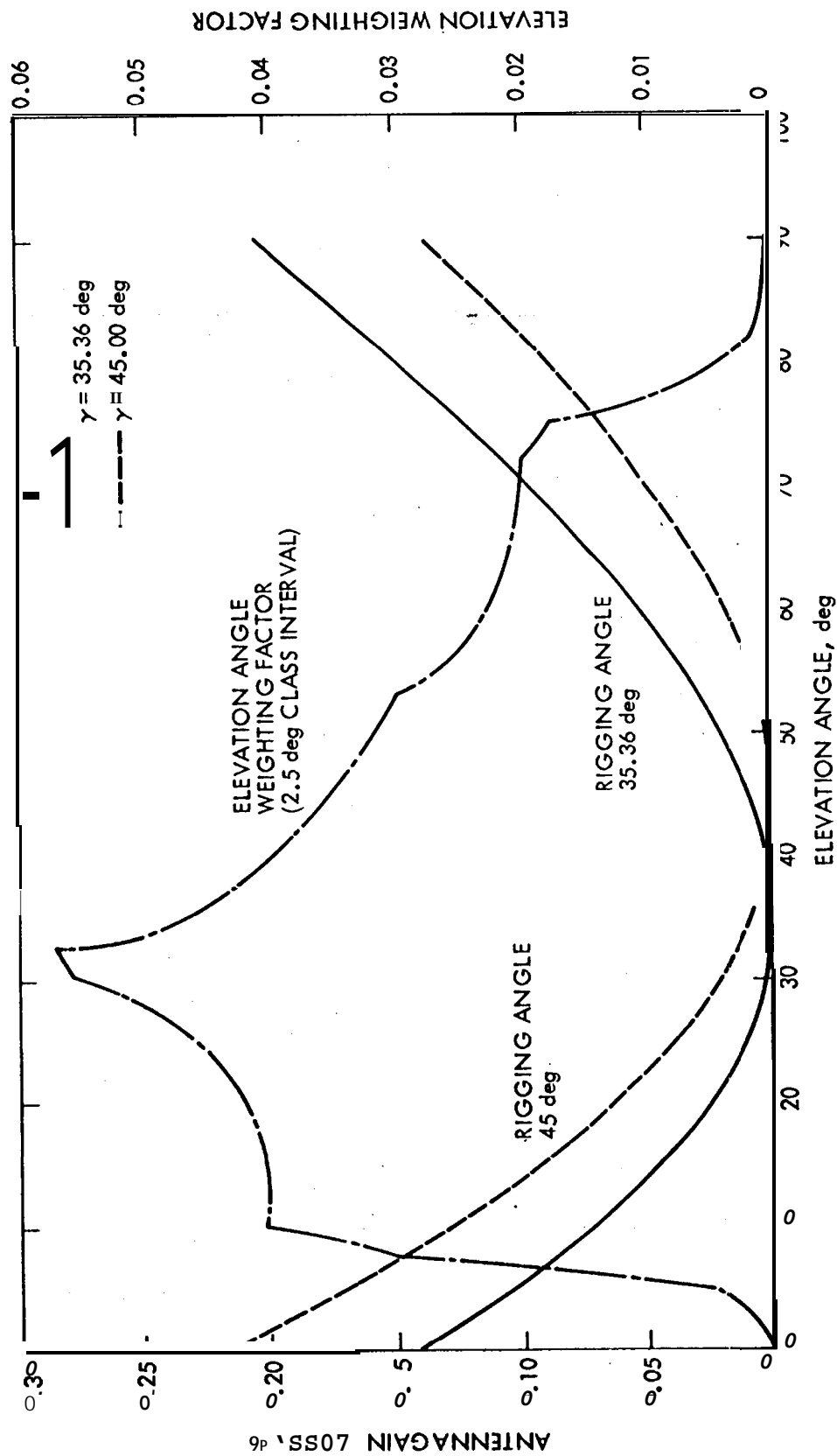
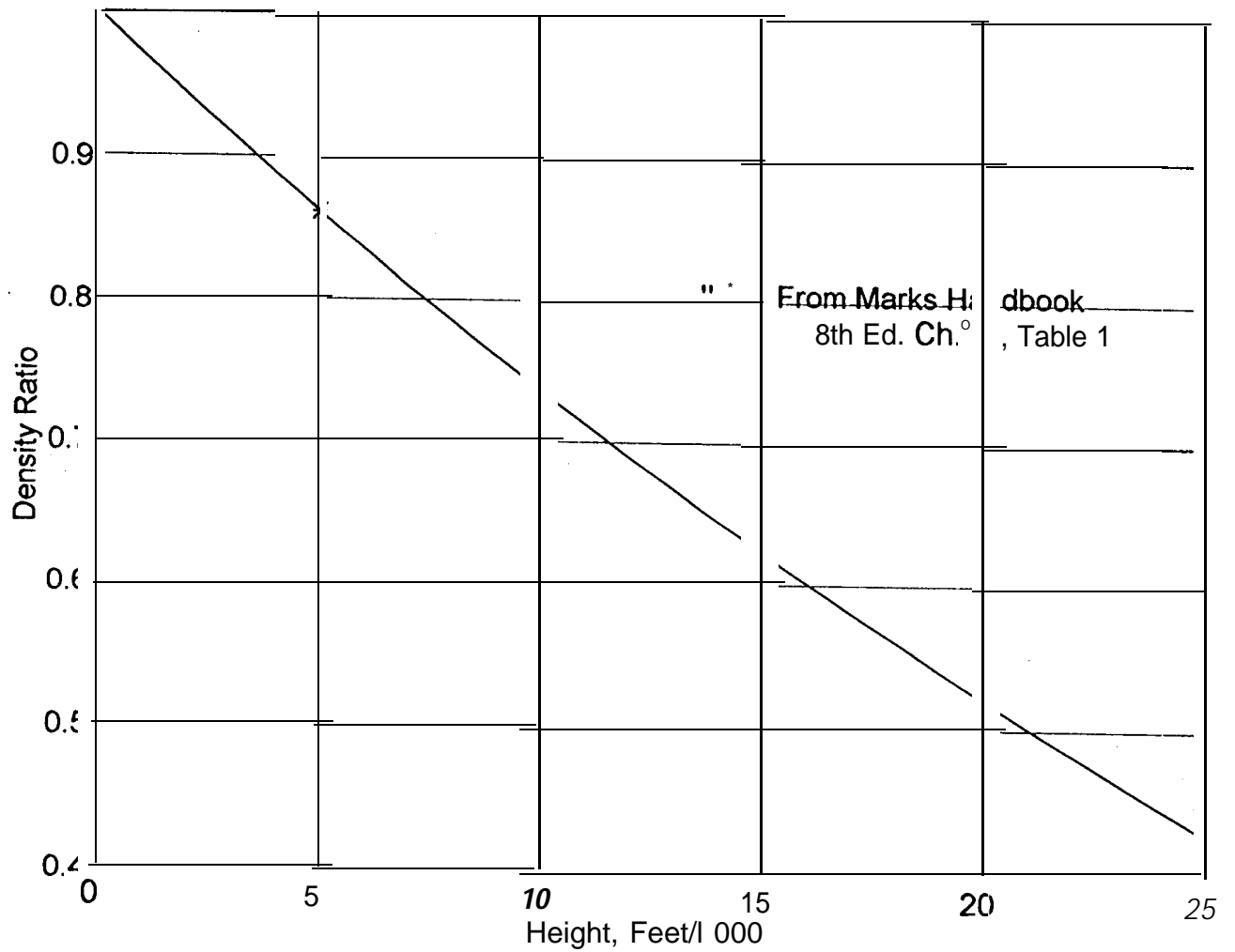


Fig. 5
 Figure 4-4 MARS Antennas Rigging Angle

45-

Variation Of Air Density With Height



See Figures. dcf
(File)

FIGURE 4-6

ANTENNA SURFACE PRESSURE COEFFICIENTS

ELEVATION = 0

RADIUS	DEGREES FROM TOP					
	15	45	75	105	135	165
.50	1.00	1.05	1.05	1.05	1.05	1.30
.45	1.39	1.42	1.42	1.045	1.50	1.059
.40	1.48	1.49	1.52	1.51	1.62	1.65
.35	1.51	1.51	1.55	1.59	1.64	1.66
.30	1.53	1.53	1.56	1.60	1.64	1.66
.25	1.53	1.53	1.57	1.60	1.64	1.65
.20	1.54	1.55	1.58	1.61	1.64	1.64
.15	1.55	1.57	1.58	1.61	1.63	1.63
.10	1.56	1.58	1.59	1.61	1.62	1.62
.05	1.58	1.59	1.60	1.61	1.61	1.61

ELEVATION = 60

RADIUS	DEGREES FROM TOP					
	15	45	75	105	135	165
.50	0.68	0.80	2.60	4.30	3.15	2.50
.45	1.00	1.09	2.30	3.30	1.80	1.42
.40	1.19	1.27	1.95	2.36	1.43	1.19
.35	1.29	1.36	1.75	1.80	1.39	1.17
.30	1.38	1.43	1.66	1.60	1.37	1.14
.25	1.47	1.47	1.63	1.53	1.39	1.11
.20	1.53	1.50	1.62	1.51	1.41	1.09
.15	1.56	1.52	1.58	1.51	1.45	1.12
.10	1.57	1.53	1.58	1.50	1.47	1.24
.05	1.56	1.53	1.55	1.52	1.50	1.41

ELEVATION = 90 (STOW)

RADIUS	DEGREES FROM TOP					
	15	45	75	105	135	165
.50	0.30	-0.03	0.01	-0.23	-0.63	-1.20
.45	0.57	0.29	0.02	-0.10	-0.53	-0.90
.40	0.50	0.30	0.04	-0.08	-0.45	-0.75
.35	0.47	0.20	0.05	-0.06	-0.37	-0.64
.30	0.26	0.09	0.07	-0.06	-0.30	-0.54
.25	0.17	0.05	0.08	-0.05	-0.22	-0.53
.20	0.12	0.03	0.06	-0.03	-0.15	-0.32
.15	0.09	0.02	0.05	-0.02	-0.09	-0.20
.10	0.07	0.02	0.04	-0.01	-0.04	-0.12
.05	0.04	0.02	0.03	0.00	-0.01	-0.05

ELEVATION = 120

DEGREES FROM TOP

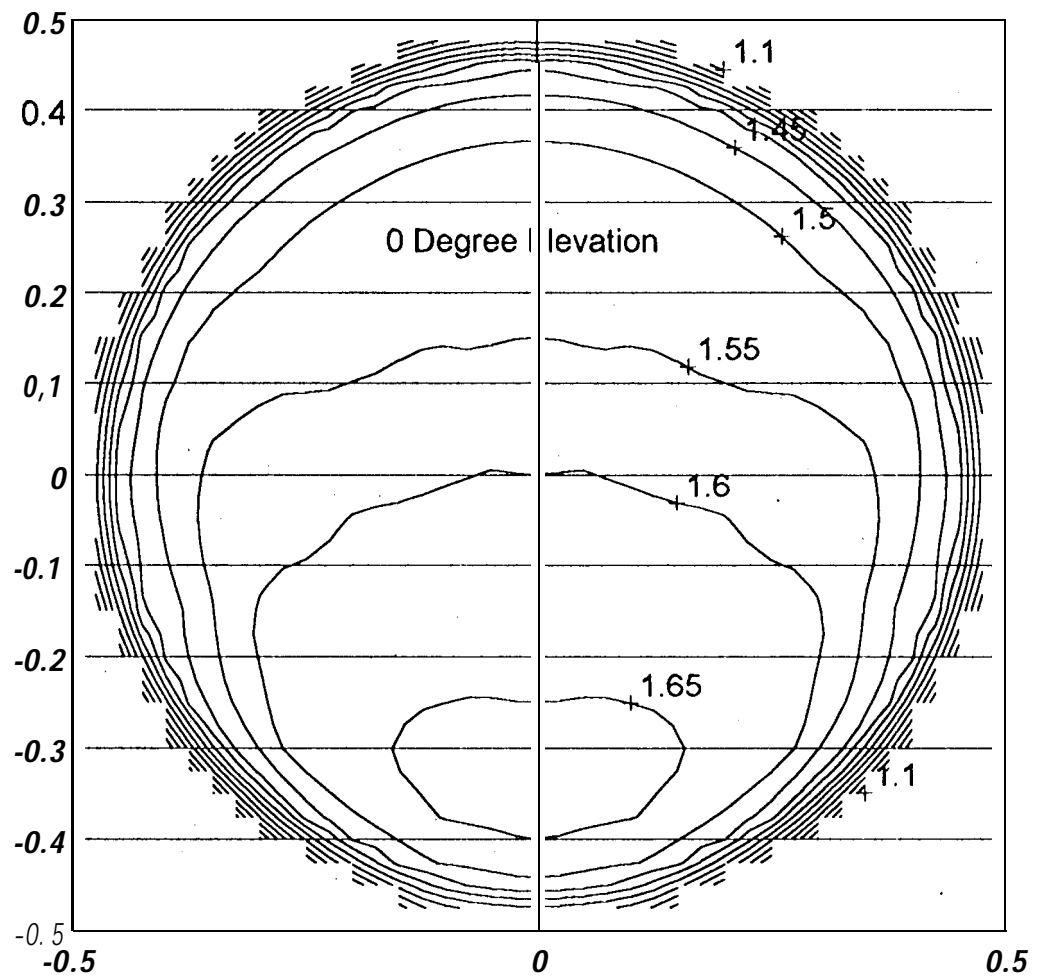
Fig 4-6 Cont'd

	15	45	75	105	135	165
RADIUS						
.50	-1.24	-0.72	-0.22	-0.05	-0.10	-0.08
.45	-1.28	-0.86	-0.27	0.02	0.07	0.05
.40	-1.25	-0.89	-0.31	0.07	0.16	0.10
.35	-1.18	-0.84	-0.30	0.10	0.21	0.13
.30	-1.10	-0.76	-0.28	0.12	0.24	0.17
.25	-1.03	-0.66	-0.23	0.12	0.25	0.20
.20	-0.93	-0.54	-0.18	0.11	0.24	0.24
.15	-0.78	-0.40	-0.13	0.09	0.21	0.25
.10	-0.55	-0.24	-0.08	0.07	0.16	0.22
.05	-0.22	-0.10	-0.03	0.04	0.10	0.14

ELEVATION = 180

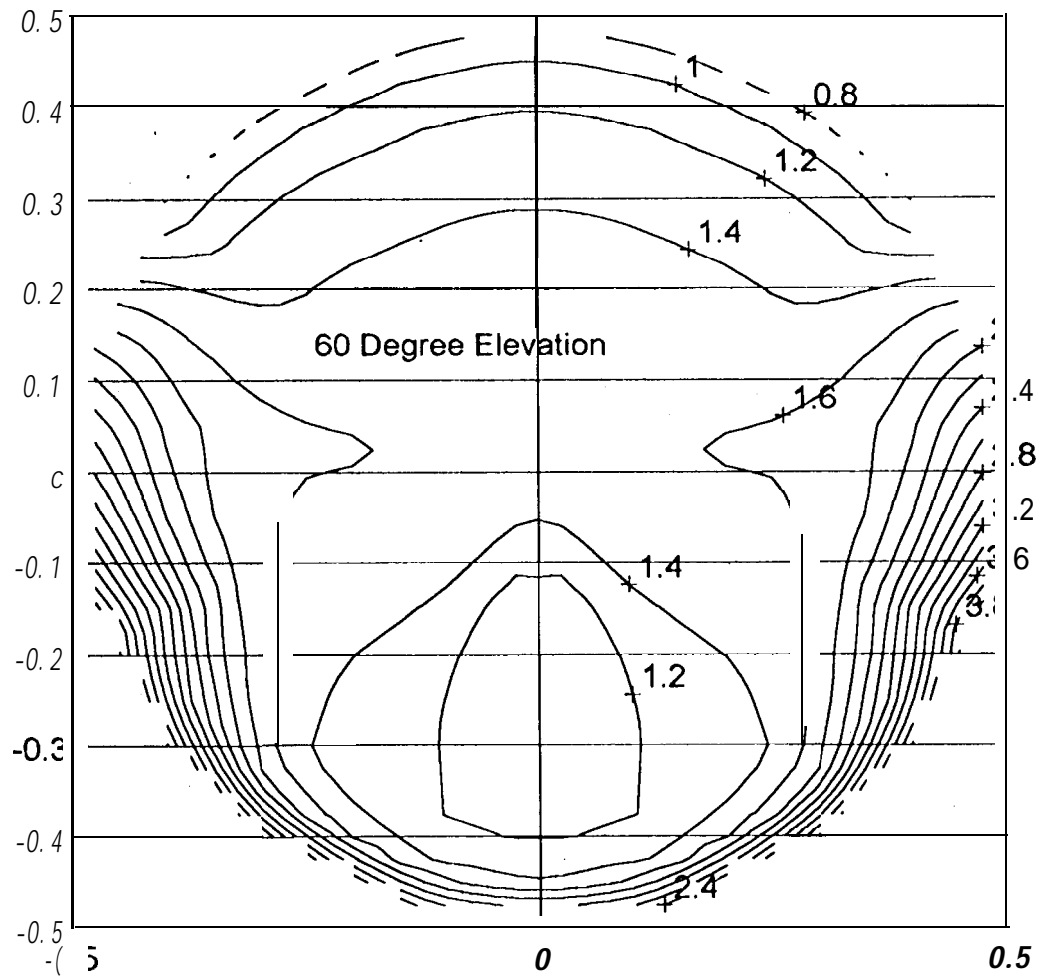
	DEGREES FROM TOP					
	15	45	75	105	135	165
RADIUS						
.50	-0.45	-0.37	-0.47	-0.49	-0.51	-0.88
.45	-0.68	-0.65	-0.70	-0.73	-0.87	-1.00
.40	-0.85	-0.85	-0.90	-0.90	-1.03	-1.14
.35	-1.00	-1.02	-1.04	-1.06	-1.11	-1.25
.30	-1.13	-1.16	-1.16	-1.18	-1.18	-1.31
.25	-1.24	-1.24	-1.24	-1.27	-1.24	-1.33
.20	-1.34	-1.32	-1.32	-1.35	-1.30	-1.36
.15	-1.39	-1.36	-1.36	-1.39	-1.34	-1.37
.10	-1.41	-1.39	-1.39	-1.41	-1.38	-1.40
.05	-1.42	-1.41	-1.41	-1.42	-1.41	-1.42

Antenna Wind Pressure Contours



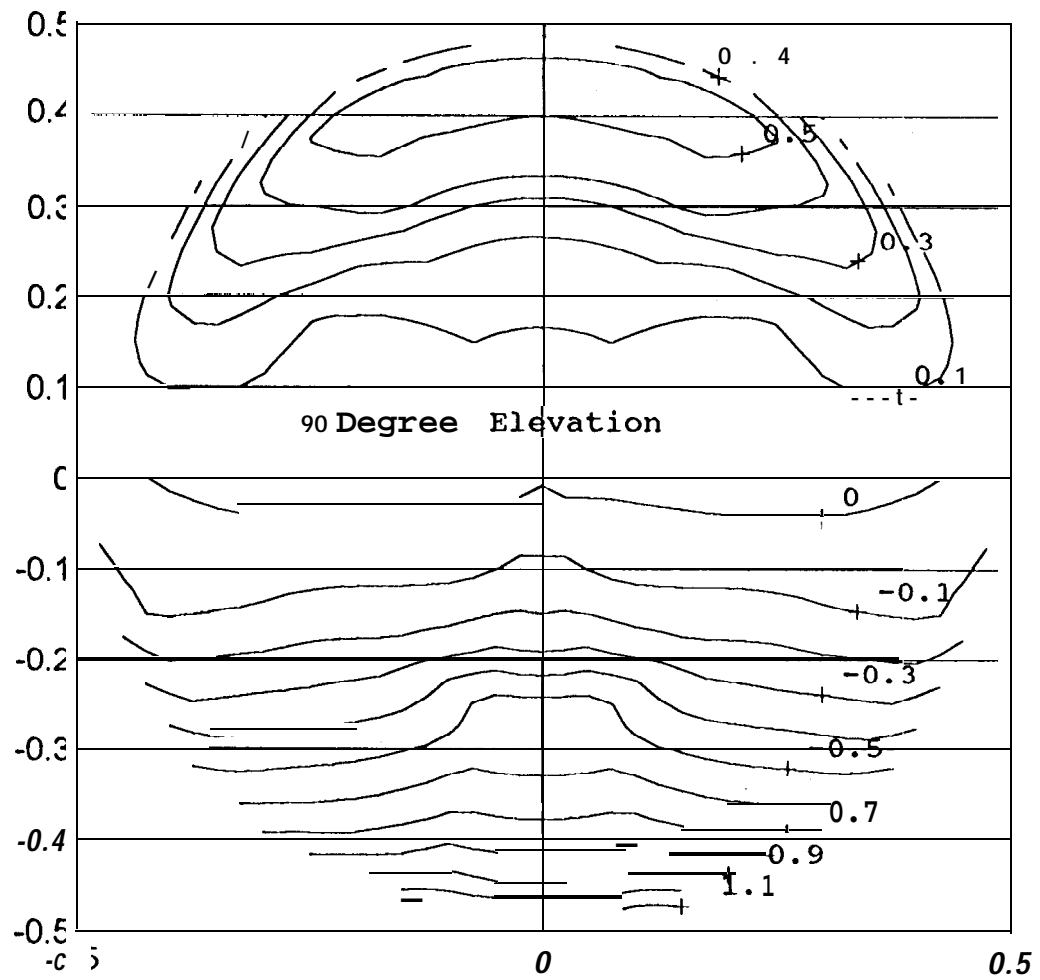
A-7a

Antenna Wind Pressure Contours



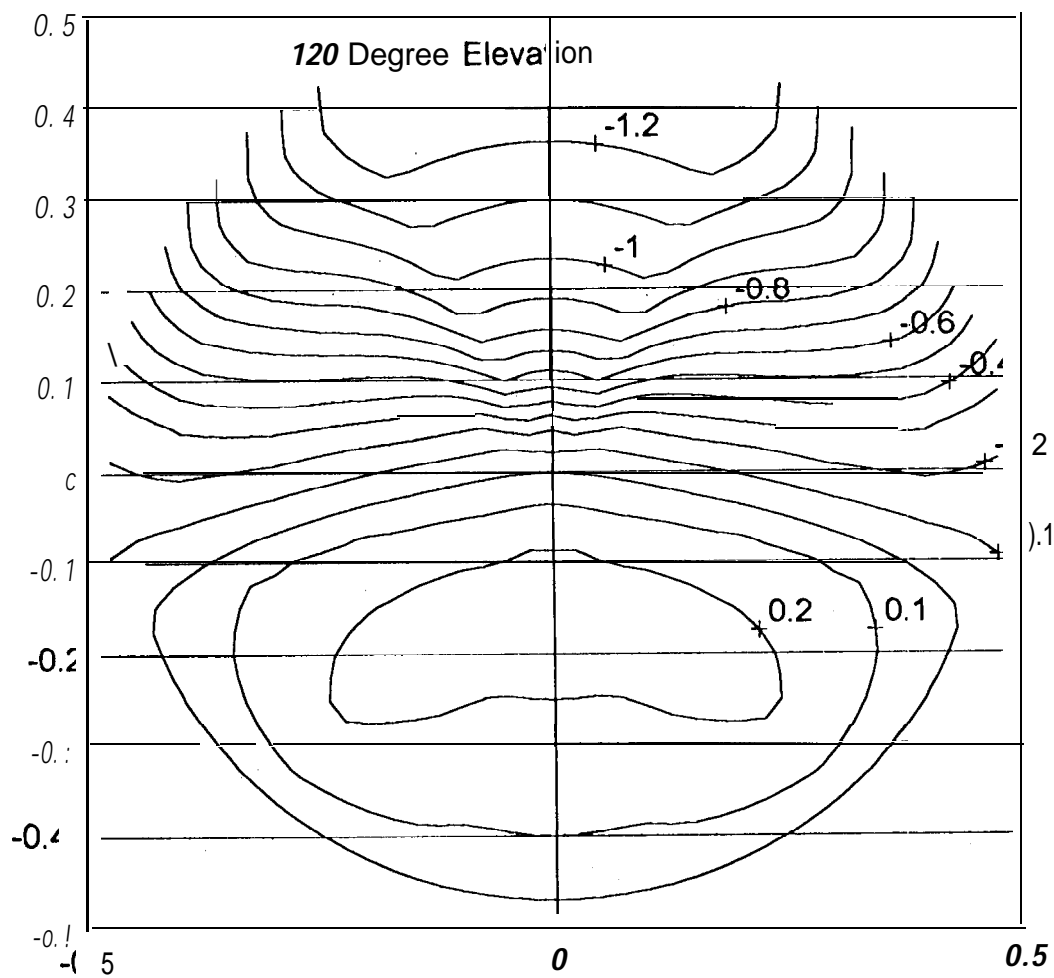
4-7 b

Antenna Wind Pressure Contours



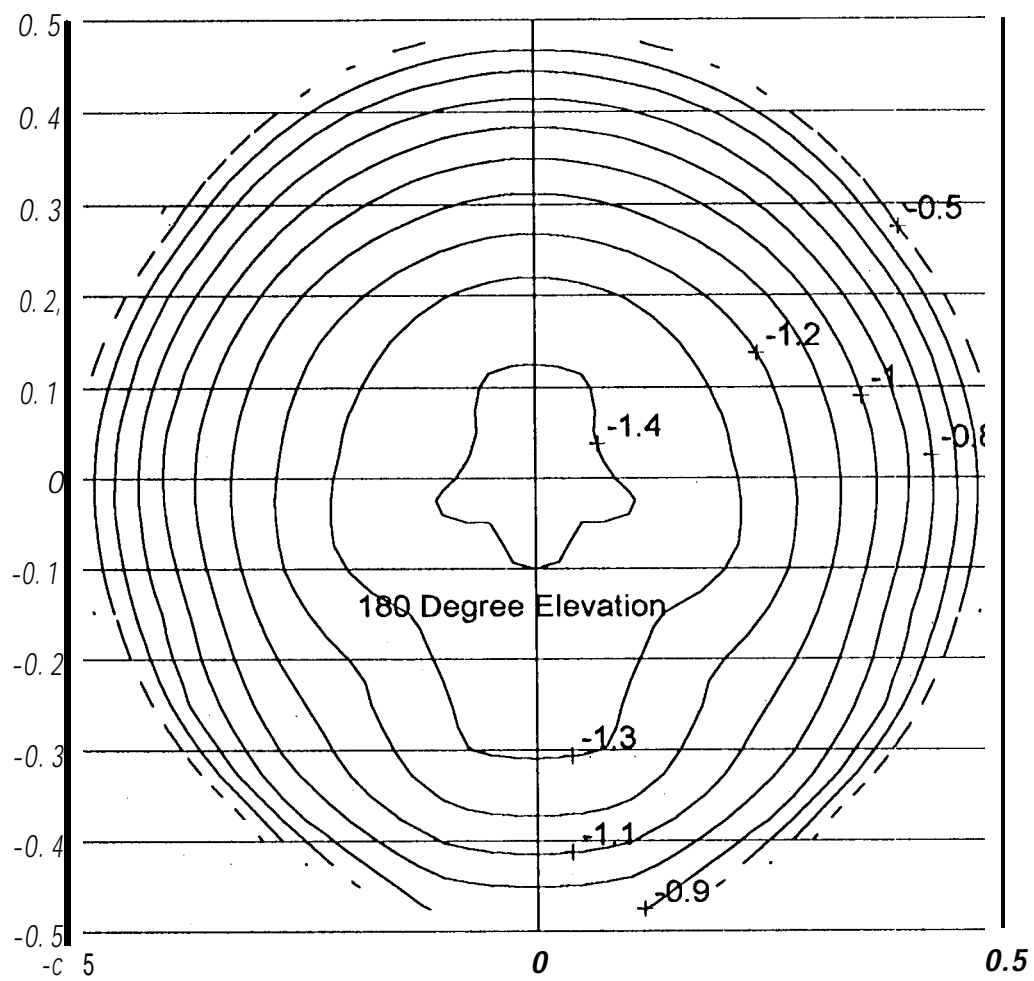
4-7c

Antenna Wind Pressure Contours



4-7d

Antenna Wind Pressure Contours



47e

8

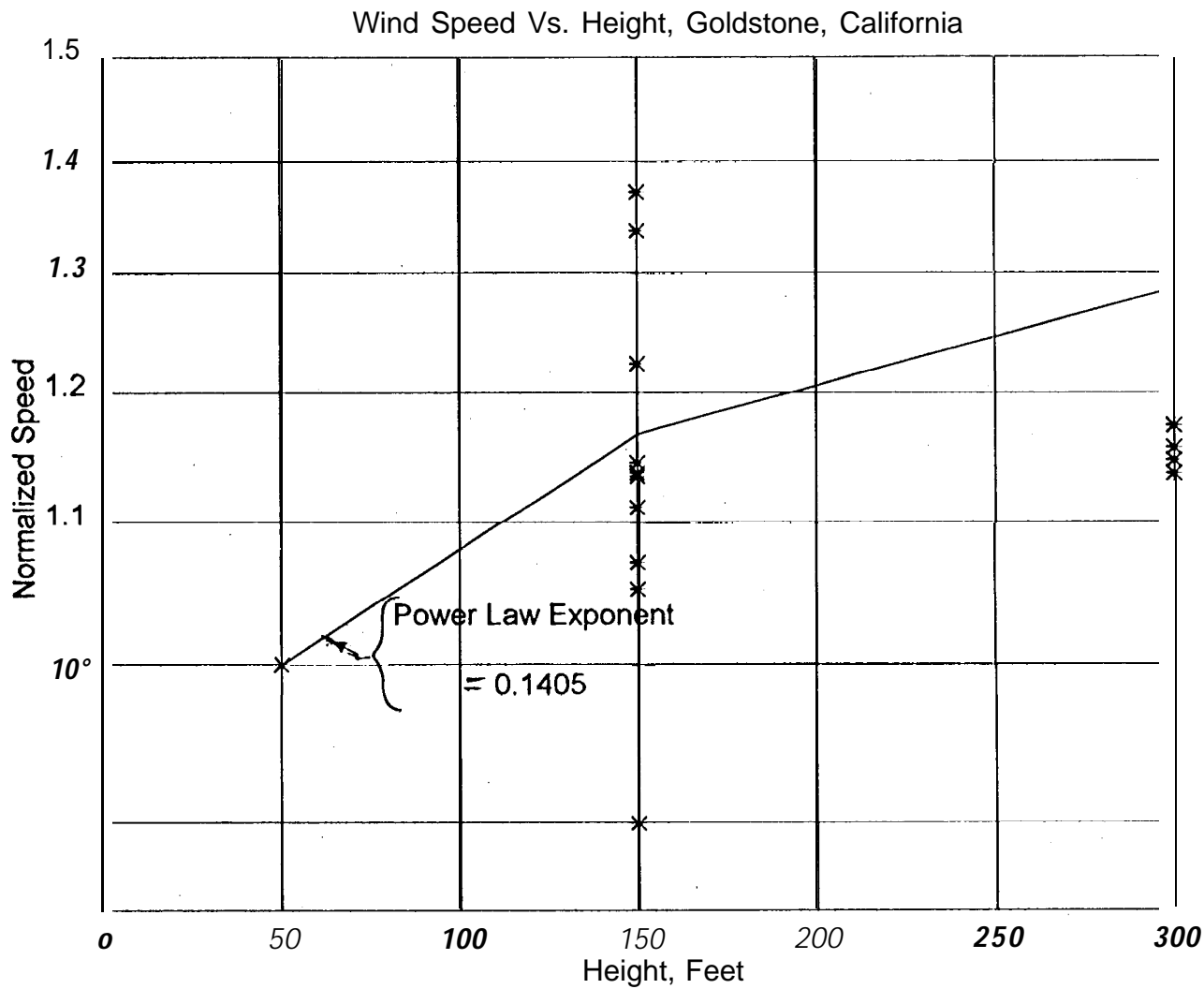
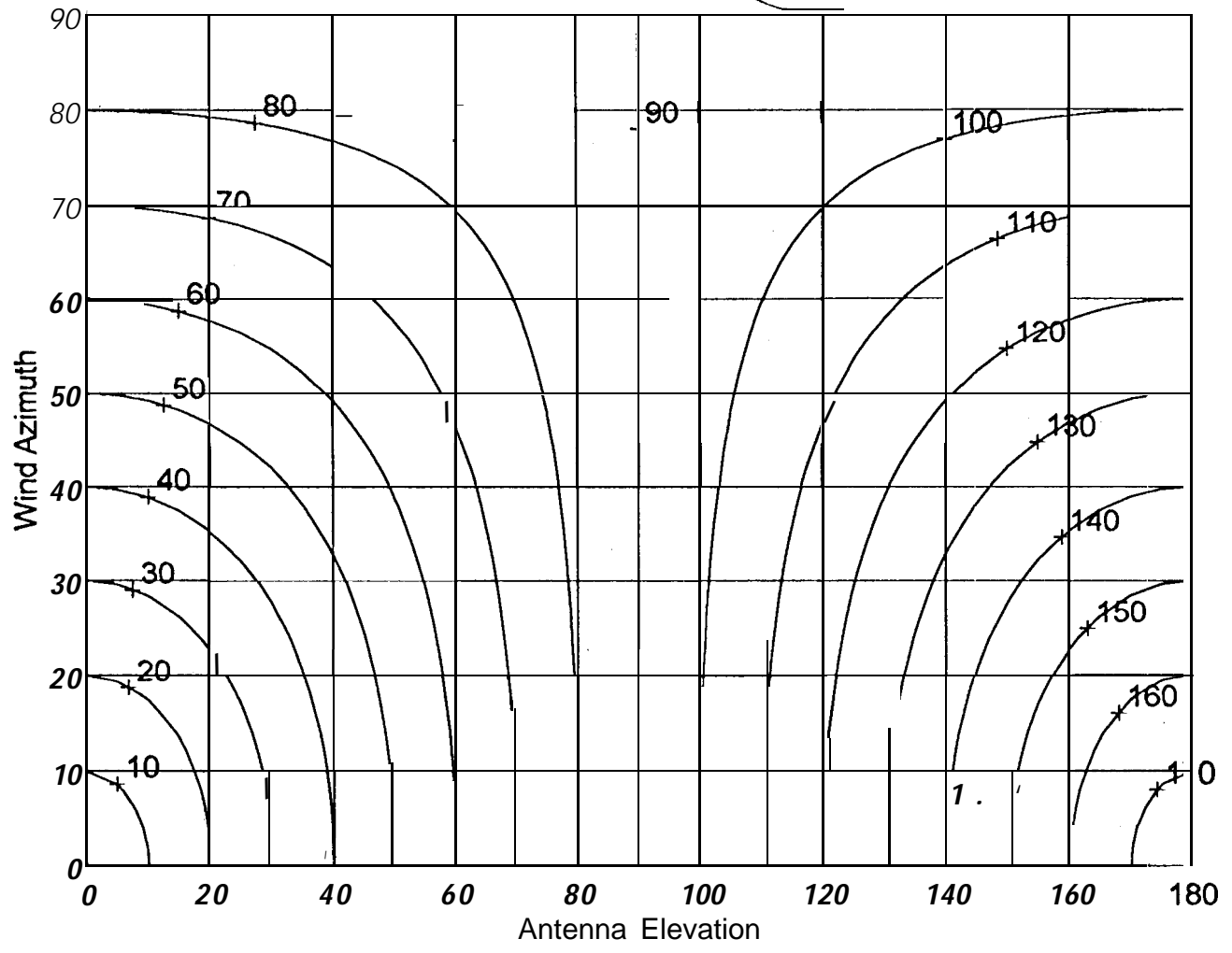


Fig 4-9

Compound

Elevation and Azimuth To Produce Compound Angles



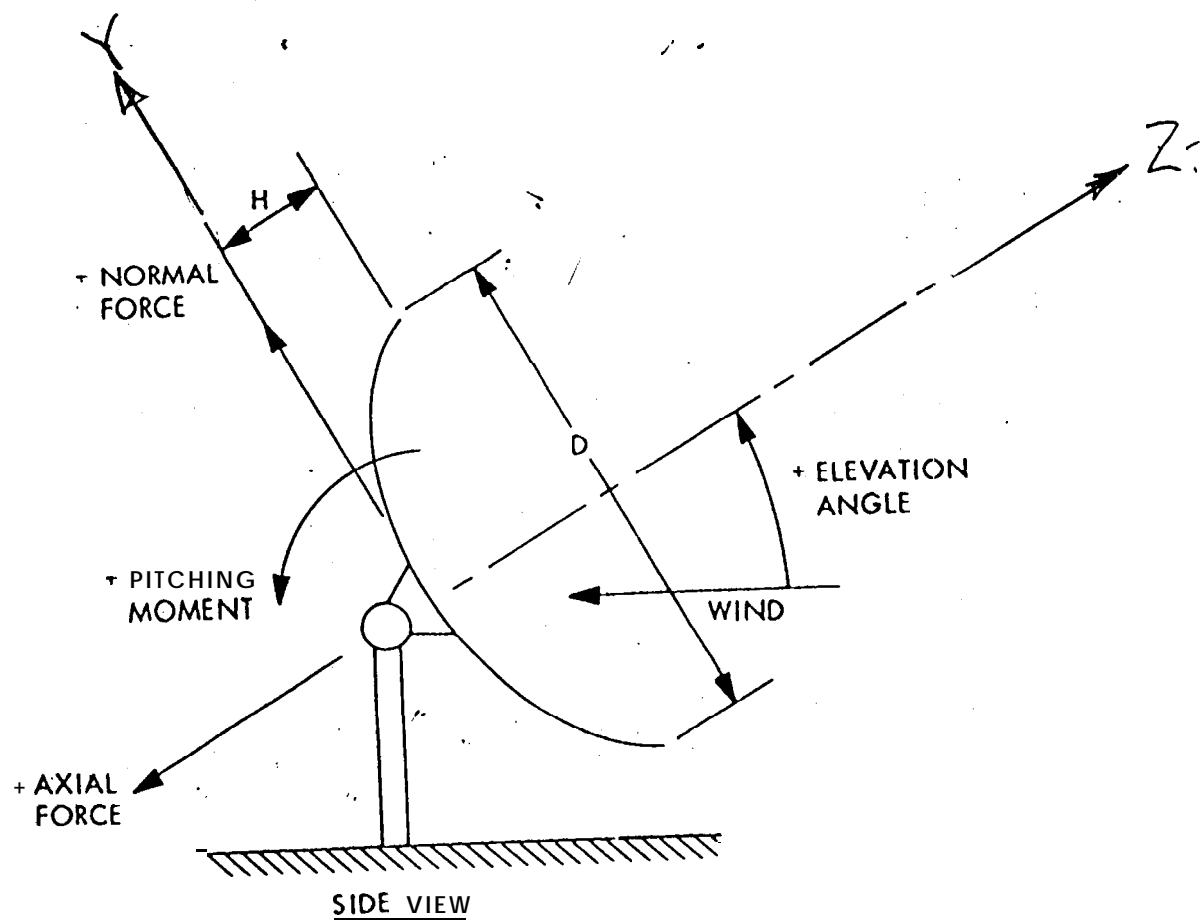


FIG 4-10

WIND TUNNEL FORCE
BALANCE COORDINATES

Fig 4-11

Top Surface Nodes, 30 Foot Diameter (Half) Aperture

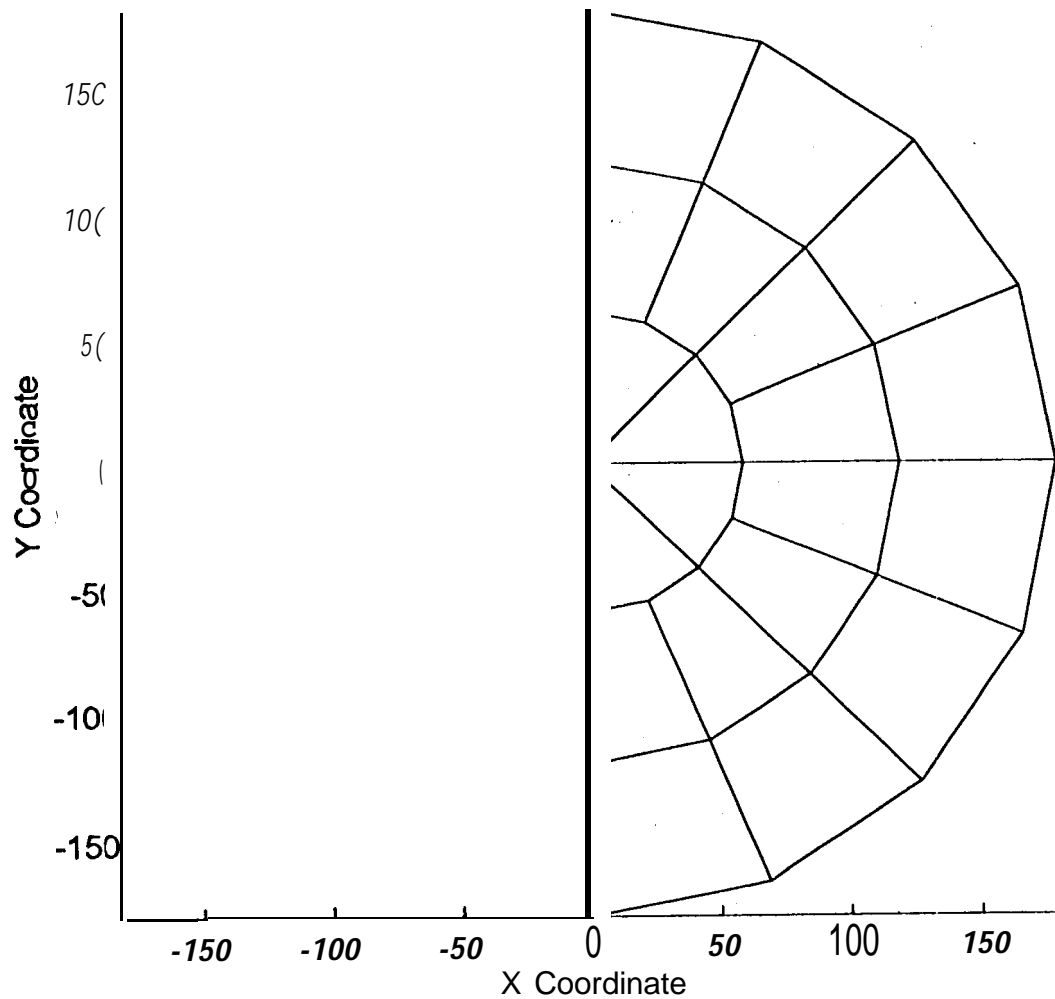
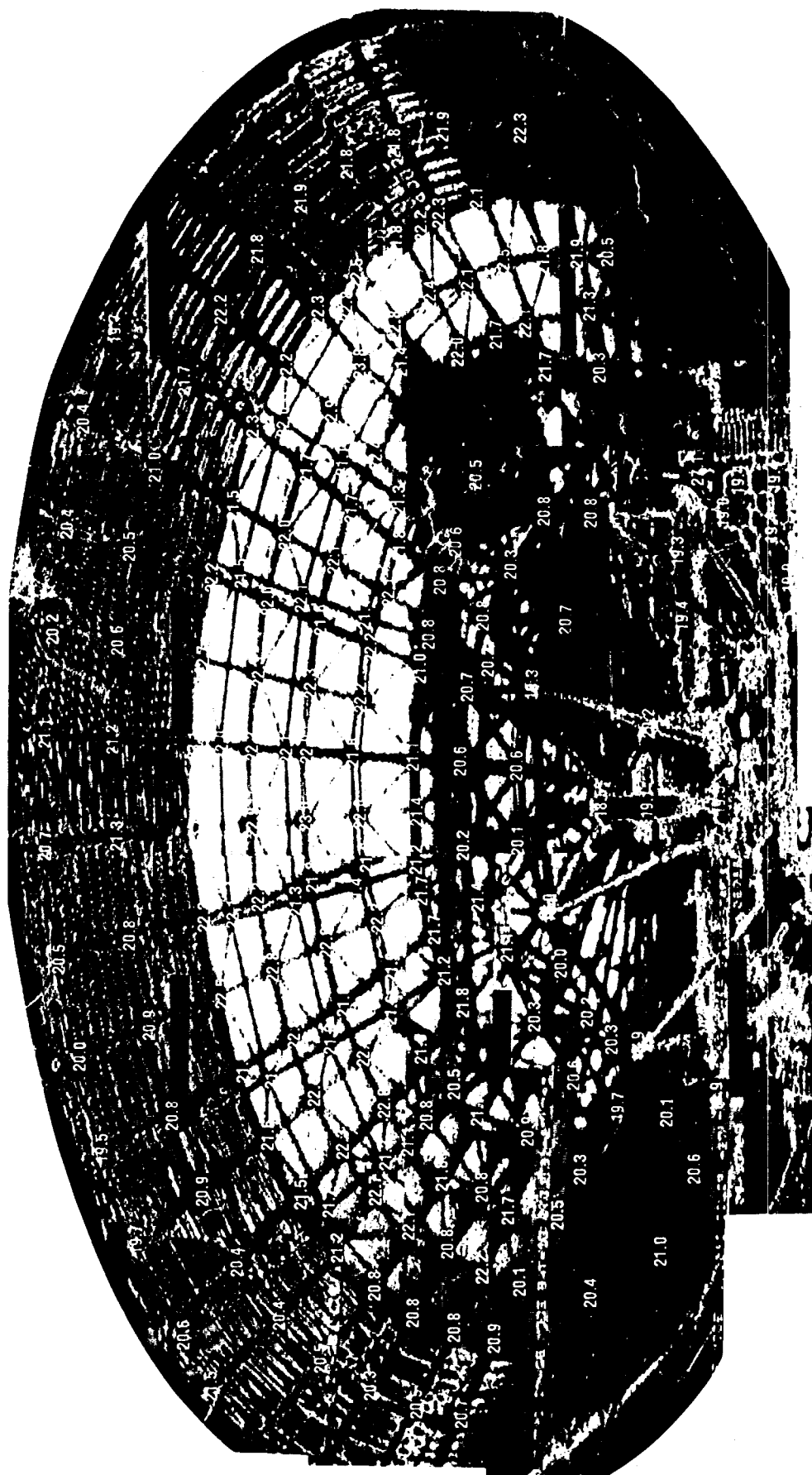


Fig 4-12
Infrared
Camera
Measurements



TABLES

4-1 Elevation Weighting Factors for Solar Missions, Antenna
Latitude = 35.4 degrees

4-2 Total Wind Loading Comparisons, 30-ft-diameter Half Antenna

4-3 Total Wind Loading Comparisons; 132-ft-diameter Half Antenna

TABLE 4-1
ELEVATION WEIGHTING FACTORS FOR SOLAR MISSIONS
ANTENNA LATITUDE = 35.4 DEGREES

<u>Elev</u>	<u>H</u>	<u>Elev</u>	<u>H</u>	<u>Elev</u>	<u>H</u>	<u>Elev.</u>	<u>H</u>
0.0	.00000	2.5	.00000	5.0	.00402	7.5	.04034
10.0	.04065	12.5	.04106	15.0	.04162	17.5	.04237
20.0	.04338	22.5	.04478	25.0	.04686	27.5	.05038
30.0	.05983	32.5	.06156	35.0	.04657	37.5	.04289
40.0	.03850	42.5	.03660	45.0	.03353	47.5	.03217
50.0	.02966	52.5	.02855	55.0	.02633	57.5	.02534
60.0	.02327	62.5	.02235	65.0	.02033	67.5	.01944
70.0	.01738	72.5	.01653	75.0	.01431	77.5	.00942
80.0	.00000	82.5	.00000	85.0	.00000	87.5	.00000
90.0	.00000	92.5	.00000	95.0	.00000	97.5	.00000

TABLE 4-2
TOTAL WIND LOADING COMPARISONS
30 FOOT DIAMETER HALF ANTENNA
A=353 D=30

Elevation	0	60	90	120	180
Speed	60	60	100	60	60
q	9.208	9.208	25.58	9.208	9.208
C_{Normal}	-0.032	-0.078	0.153	0.216	-0.030
C_{Axial}	1.521	1.832	0.0	-0.600	-0.961
C_{Pitch}	0.038	-0.049	0.104	0.124	0.022
C_{Normal} A q	-104	-254	1383	703	-98
Sum of Normal Forces	-50	-217	905	-397	72
C_{Axial} A q	4950	5962	0	-1953	-3127
Sum of Axial Forces	4842	5377	-913	-921	-3351
C_{Pitch} A D q	3170	-4783	28,206	12,106	2148
Sum of Pitch Moments	-1435	-6532	26,022	-11,230	2107

TABLE 4-3
TOTAL WIND LOADING COMPARISONS
132 FOOT DIAMETER HALF ANTENNA
A=6842 D=132

Elevation	0	60	90 60	120	180
Speed	60	60	100	60	60
q	9.208	9.208	25.58	9.208	9.208
C _{Normal}	-0.032	-0.078	0.153	0.216	-0.030
C _{Axial}	1.521	1.832	0.0	-0.600	-0.961
C _{Pitch}	0.038	-0.049	0.104	0.124	0.022
C _{Normal} A q	-1996	-4865	26,509	13,742	-1871
Sum of Normal Forces	-1060	-3699	18,528	-8428	1459
C _{Axial} A q	94,870	114,271	0	-37,425	-59,942
Sum of Axial Forces	94,349	103,063	-17,212	-18,129	-65,091
C _{Pitch} A D q	312,873	-403,441	2,400,117	1,020,954	181,137
Sum of Pitch Moments	-125,781	-461,083	2,216,417	-994,252	175,950

APPENDIX 4A

MATLAB WIND LOADING PROGRAMS

This appendix contains the MATLAB programs WINDTUNL.M, which provides a file of NASTRAN program-type wind loading data records and the file FIGURES.M, which is invoked by WINDTUNL and supplies surface pressure loading coefficients as the basis for interpolation over a user-defined surface. These are the same coefficients as in Figure 4-6, but arranged as a MATLAB file. Additional background is provided in Section 4.2.3.

The surface is defined by the user-supplied matrix, "gridw." The first column of gridw contains the node label, the second column contains an integer flag to define the coordinate system, the third, fourth, and fifth columns contain the X, Y, and Z cartesian coordinates of the node, and the sixth column contains the weighting factor for the node. The flag in the second column is "0" (not blank) when the X, Y, and Z coordinates are supplied in the next three columns. When the flag is "1" a cylindrical coordinate system is implied with the radius in the third column, the angle (positive clockwise from the Y axis) is in the fourth column. Z coordinates in the fifth column can be arbitrary because the program recomputes these from the equation of the parabola.

In addition to gridw, the user is also prompted to supply the focal length, antenna diameter, and another flag to establish whether the model is for a full antenna or a symmetric (right) half. The user also supplies a vector of wind speeds for each antenna attitude, and the name of a file in which the output force data is to be stored. The user also has the option of either traditional English units or SI units and the dimensions and other details for-input and output data in these units are documented within the program.

ED: This Appendix *requires* the files WINDTUNL.M and FIGURES.M

4-4

This is the first part of Appendix ~~A~~ to Chapter 4

```
% August 4,1993 this is WINDTUNL.M
% Set a few defaults
sym=.5,diam=360, f=152.5, system='ENG',speed=60 % default for
debug
disp('supply diameter,diam=, sym=(1 is full or.5 is half),
focus,f=')
disp(' "gridw= ", e.g. gridw=[label flag(0 vs 1) X Y Z
weight] ')
disp(' , system=(blankSI or ENG- in quotes) and "return" ')
ew=exist('nowait')

keyboard
label=gridw(:,1);rad=gridw(:,3);angle=gridw(:,4);wgt=gridw(:,6);
sumw=sum(wgt)
qf=find(gridw(:,2)==0);
%convert 0 flags to cylindrical coords
if(length(qf)>1)
x(qf)=gridw(qf,3); y(qf)=gridw(qf,4); rad(qf)=sqrt(x.^2+y.^2);
angle(qf)=180/pi*atan(x(qf)./y(qf));
%[x y rad angle] % debug
end
qa=find(angle<0);if(qa>0),atemp=angle; ,atemp(qa)=atemp(qa)+360;
end
x=rad.*sine(angle);y=rad.*cosine(angle);z=rad.^2/4/f;
t=sqrt(rad.^2+4*f^2*ones(size(rad)));
gx=x./t;gy=y./t;gz=2*t.^(-1)*f;
aproj=pi/4*diam*diam*sym;

if(system=='ENG')
anetft=aproj/144
afact=anetft/sumw % tributary area per unit of "wgt"

adens=.002378 % slugs/cu-ft =# sec*sec/ft /ft/ft/ft
qfact=0.5*adens*(5280/3600)^2 % =q/(vel*vel)
end

if (system==' S1')
afact=aproj/sumw;
%some conversions: 1lb=4.448n,1
ft.=.3048m,4.448/.3048=14.5932kg/slug
adens=1.2255 % kg/cu. meter =.002378/14.5932/(.3048^3)
qfact=.5*adens
end

gridaw=afact*wgt; % vector of areas associated with each grid
aslope=gridaw./gz;
asurf=sum(aslope)

figures
figset=5:9;
speeds=[60 60 100 60 60];
```

```

ffile= 'forcimag.dat'
disp(' Provide name of file for saving "FORCE" records,"ffile=
" ')
disp(' provide figset=[ vector of FIGURES to use (default=5:9) ]')
disp(' provide speeds=[vector of speeds, to match figset, ] ')
disp(' speeds(default) = [60 60 100 60 60] (mph) , then "return"')

keyboard
for j =1:length(figset)
fid=figset(j)
speed=speeds (j)
clear fig
ss=sprintf( 'FIGURE%g',fid)
fig=eval(ss) ;
qq=sprintf( 'PZERO%g',fid)
PZERO=eval(qq)
flip=fliplr(fig) ;
fig=[fig(:,1) fig flip fig(:,1)];
az=15:30:359; az=[0 az 360];
radii=(.5:-.05:0)';
fig(11,:)=PZERO*ones(1,14) ;
rr=rad/diam;
tic,pres=interp2(az, radii, fig,atemp,rr) ;toc
q=qfact*speed*speed
fmag=-q*pres. *aslope;
disp('      Node      Radius      Angle      Coeff.      Force
Slope-A')
sumry=[label      rad      rr      angle      pres      fmag      aslope]
fx=fmag. *gx;fy=fmag. *gy; fz=fmag.*gz;
sumx=sum(fx) ; sumy=sum(fy) ; sumz=sum(fz) ;
xmoment=sum(fy. *z-fz .*y) ;
fprintf(' Results For Force ID %g.\n',fid)
disp(' The sums of the forces are')
sumf=[sumx sumy sumz], fprintf(' Pitch moment(about X axis)
%g.\n',xmoment)
lf=length(fmag) ;
FORCE=[fid*ones(lf,1) label fmag gx gy gz pres aslope];
filid=fopen(ffile, 'a+')
fprintf(filid, 'FORCE
%8.0f%8. 0f%8.1f%8.4f%8 .4f%8.4f\r\n', FORCE(:,1:6));
disp('to continue "return"')
ew=exist( 'nowait')
if(ew==0) ,keyboard,end %if "nowait" not given a value,wait
end
fclose(filid)
disp(' Card images saved on ASCII file'),ffile

```

.4-

This is part of Appendix A to Chapter 4

```
% July 29 this is FIGURES.M, made from UNIVAC RIL. (or RIL-ABS.)
%           ANTENA MODEL WIND PRESSURE COEFFICIENT DATA FROM
%           WIND TUNNEL STUDIES. FROM 'JPL CP-4'.
%           REVISED 27 OCT '81 TO PROPERLY ORIENT BACK-WINDED
STRUCTURES
```

```
%C
  FIGURE5=[ . . . %           O DEG PITCH ANGLE
%THETA=>
% 15           45           75           105           135           165

1.00,         1.05,         1.05,         1.05,         1.05,         1.30,
1.39,         1.42,         1.42,         1.45,         1.50,         1.59,
1.48,         1.49,         1.52,         1.51,         1.62,         1.65,
1.51,         1.51,         1.55,         1.59,         1.64,         1.66,
1.53,         1.53,         1.56,         1.60,         1.64,         1.66,
1.53,         1.53,         1.57,         1.60,         1.64,         1.65,
1.54,         1.55,         1.58,         1.61,         1.64,         1.64,
1.55,         1.57,         1.58,         1.61,         1.63,         1.63,
1.56,         1.58,         1.59,         1.61,         1.62,         1.62,
1.58,         1.59,         1.60,         1.61,         1.61,         1.61,]
PZERO5=1.60, %                               $END
```

```
%E 6           60 DEG PITCH ANGLE
% 15           45           75           105           135           165

FIGURE6=[ . . .
.68,          .8,          2.6,          4.3,          3.15,          2.5,
1.0,          1.09,         2.3,          3.3,          1.8,          1.42,
1.19,         1.27,         1.95,         2.36,         1.43,         1.19,
1.29,         1.36,         1.75,         1.8,          1.39,         1.17,
1.38,         1.43,         1.66,         1.6,          1.37,         1.14,
1.47,         1.47,         1.63,         1.53,         1.39,         1.11,
1.53,         1.5,          1.62,         1.51,         1.41,         1.09,
1.56,         1.52,         1.58,         1.51,         1.45,         1.12,
1.57,         1.53,         1.58,         1.50,         1.47,         1.24,
1.56,         1.53,         1.55,         1.52,         1.50,         1.41,];
PZERO6=1.52 %                               $END
```

```
FIGURE7=[. . . %           90 DEG PITCH ANGLE (STOW)
%15           45           75           105           135           165

.30,          -.03,         .01,          -.23,         -.63,         -1.20,
.57,          .29,          .02,          -.10,         -.53,         -.90,
.50,          .30,          .04,          -.08,         -.45,         -.75,
.47,          .20,          .05,          -.06,         -.37,         -.64,
.26,          .09,          .07,          -.06,         -.30,         -.54,
.17,          .05,          .08,          -.05,         -.22,         -.53,
.12,          .03,          .06,          -.03,         -.15,         -.32,
.09,          .02,          .05,          -.02,         -.09,         -.20,
.07,          .02,          .04,          -.01,         -.04,         -.12,
.04,          .02,          .03,          0.00,         -.01,         -.05,];
```

PZER07=.01 %

\$END

FIGURE8 =[... % 120 DEG PITCH ANGLE

%15 45 75 105 135 165

-1.24,	-.72,	-.22,	-.05,	-.10,	-.08,
-1.28,	-.86,	-.27,	.02,	.07,	.05,
-1.25,	-.89,	-.31,	.07,	.16,	.10,
-1.18,	-.84,	-.30,	.10,	.21,	.13,
-1.10,	-.76,	-.28,	.12,	.24,	.17,
-1.03,	-.66,	-.23,	.12,	.25,	.20,
-.93,	-.54,	-.18,	.11,	.24,	.24,
-.78,	-.40,	-.13,	.09,	.21,	.25,
-.55,	-.24,	-.08,	.07,	.16,	.22,
-.22,	-.10,	-.03,	.04,	.10,	.14,];

PZER08=.00 %

\$END

FIGURE9=[. . . % 180 DEG PITCH ANGLE

%15 45 75 105 135 165

-.45,	-.37,	-.47,	-.49,	-.51,	-.88,
-.68,	-.65,	-.70,	-.73,	-.87,	-1.00,
-.85,	-.85,	-.90,	-.90,	-1.03,	-1.14,
-1.00,	-1.02,	-1.04,	-1.06,	-1.11,	-1.25,
-1.13,	-1.16,	-1.16,	-1.18,	-1.18,	-1.31,
-1.24,	-1.24,	-1.24,	-1.27,	-1.24,	-1.33,
-1.34,	-1.32,	-1.32,	-1.35,	-1.30,	-1.36,
-1.39,	-1.36,	-1.36,	-1.39,	-1.34,	-1.37,
-1.41,	-1.39,	-1.39,	-1.41,	-1.38,	-1.40,
-1.42,	-1.41,	-1.41,	-1.42,	-1.41,	-1.42,];

PZER09=-1.42 %

\$END

APPENDIX 4B

This is a condensed excerpt of tabulated data that appeared in "Compilation Of Wind Tunnel Coefficients for Parabolic Reflectors", JPL Publication 78-16. The uncondensed data was tabulated for increments of 5 degrees in both elevation and azimuth. There are three other tables in this reference for other focal length-to-diameter ratios and surface porosities.

The use of these data is discussed in Section 4.2.6 of the text and was employed in the computations of Tables 4-2 and 4-3.

ED: This appendix requires **tablea4b**

Appendix 4-B

This is "app4-b" (Appendix B to Ch 4)

TABLE ~~4-B~~
WIND TUNNEL FORCE BALANCE COEFFICIENTS
Focal Length To Diameter Ratio =0.313
Solid Surface
(Excerpt From Table A-2, Ref. [4-10])

AZIMUTH ANGLE = 0.0

ELEVATION ANGLE	FORCE NORMAL	COEFFICIENTS AXIAL	COEFFICIENTS SIDE	MOMENT PITCH	COEFFICIENTS ROLL	COEFFICIENTS YAW
0.0	-0.032	1.521	-0.002	0.038	-0.020	-0.003
15.0	-0.039	1.501	0.001	0.032	0.002	-0.002
30.0	-0.058	1.461	0.001	0.020	0.001	-0.001
45.0	-0.110	1.602	-0.003	-0.042	0.002	-0.001
60.0	-0.078	1.832	-0.011	-0.049	0.002	
75.0	0.122	0.981	-0.010	0.069	0.001	0.001
90.0	0.153		-0.007	0.104	0.001	
105.0	0.161	-0.502	-0.004	0.110	0.001	
120.0	0.216	-0.600		0.124		0.001
135.0	0.201	-0.532	0.004	0.112	-0.001	0.001
150.0	0.151	-0.793	0.004	0.050	-0.001	0.002
165.0	0.070	-0.880	0.003	0.028		0.002
180.0	-0.030	-0.961	0.002	0.022	0.001	0.002

AZIMUTH ANGLE = 15.0

ELEVATION ANGLE	FORCE NORMAL	COEFFICIENTS AXIAL	COEFFICIENTS SIDE	MOMENT PITCH	COEFFICIENTS ROLL	COEFFICIENTS YAW
0.0	-0.032	1.525	-0.022	0.068	-0.006	-0.021
15.0	-0.034	1.485	-0.022	0.068	-0.003	-0.021
30.0	-0.047	1.495	-0.027	0.047	0.001	-0.025
45.0	-0.066	1.574	-0.034	-0.042	0.005	-0.020
60.0		1.474	-0.017	0.011	0.007	0.012
75.0	0.108	0.983	0.013	0.113	0.008	0.037
90.0	0.122	0.141	0.034	0.122	0.009	0.047
105.0	0.126	-0.454	0.052	0.120	0.009	0.054
120.0	0.153	-0.767	0.062	0.111	0.010	0.056
135.0	0.150	-0.666	0.070	0.086	0.011	0.057
150.0	0.133	-0.756	0.075	0.047	0.010	0.059
165.0	0.096	-0.871	0.079	0.005	0.009	0.060
180.0	-0.018	-0.942	0.081	-0.038	0.007	0.060

AZIMUTH ANGLE = 30.0

ELEVATION ANGLE	FORCE NORMAL	COEFFICIENTS AXIAL	COEFFICIENTS SIDE	MOMENT PITCH	COEFFICIENTS ROLL	COEFFICIENTS YAW
0.0	-0.025	1.577	-0.044	0.030	-0.013	-0.038
15.0	-0.032	1.447	-0.042	0.058	-0.004	-0.031
30.0	-0.049	1.507	-0.043	0.062		-0.035
45.0	-0.052	1.786	-0.050	-0.034	-0.004	-0.070
60.0	-0.009	1.606	-0.029	0.010	0.002	-0.019
75.0	0.107	0.725	0.052	0.112	0.003	0.042
90.0	0.112	-0.103	0.094	0.120	0.004	0.065
105.0	0.112	-0.636	0.119	0.117	0.004	0.079

120.0	0.123	-0.912	0,136	0.113	0.005	0.089
135.0	0.127	-0.721	0.146	0.076	0,006	0,097
150.0	0.118	-0.584	0.153	0,034	0.006	0.101
165.0	0.085	-0.600	0.157	0.008	0.004	0.102
180.0	-0.016	-0.730	0.158	-0.019	0.002	0.103

AZIMUTH ANGLE = 45.0

ELEVATION ANGLE	FORCE NORMAL	COEFFICIENTS AXIAL	COEFFICIENTS SIDE	MOMENT PITCH	COEFFICIENTS ROLL	COEFFICIENTS YAW
0.0	-0.021	1.519	-0.058	0.035	0.018	-0.044
15.0	-0.018	1.609	-0.064	0.055	0.006	-0.055
30.0	-0.008	1.629	-0.070	0.070	0.001	-0.082
45.0	0.013	1.588	-0.035	0.062	0.004	-0.038
60.0	0.053	1.288	0.039	0.066	0.006	0.029
75.0	0.105	0.526	0.090	0.096		0.060
90.0	0.105	-0.105	0.124	0.097	-0.001	0.080
105.0	0.108	-0.498	0.134	0.096		0.091
120.0	0.116	-0.553	0.140	0.083	0.003	0.099
135.0	0.115	-0.200	0.175	0.072	-0.003	0.109
150.0	0.095	-0.358	0.191	0.035	0.005	0.121
165.0	0.057	-0.512	0.197	0.014	0.005	0.128
180.0	-0.006	-0.600	0.200	-0.008	0.001	0.130

AZIMUTH ANGLE = 60.0

ELEVATION ANGLE	FORCE NORMAL	COEFFICIENTS AXIAL	COEFFICIENTS SIDE	MOMENT PITCH	COEFFICIENTS ROLL	COEFFICIENTS YAW
0.0	0.085	1.581	-0.076	0.130	0.018	-0.075
15.0	0.017	1.671	-0.065	0.089	0.018	-0.050
30.0	-0.008	1.531	-0.030	0.090	0.022	-0.010
45.0	0.020	1.162	0.050	0.071	0.013	0.035
60.0	0.056	0.802	0.120	0.061	0.003	0.070
75.0	0.078	0.397	0.142	0.071	0.001	0.090
90.0	0.084	0.057	0.150	0.065	0.002	0.100
105.0	0.084	-0.269	0.150	0.054	0.002	0.105
120.0	0.077	-0.490	0.155	0.040	0.003	0.102
135.0	0.067	-0.534	0.180	0.025	0.006	0.120
150.0	0.056	-0.121	0.201	0.012	-0.001	0.132
165.0	0.032	-0.150	0.228	0.002	-0.005	0.140
180.0	-0.019	-0.163	0.235	-0.002	-0.005	0.145

AZIMUTH ANGLE = 75.0

ELEVATION ANGLE	FORCE NORMAL	COEFFICIENTS AXIAL	COEFFICIENTS SIDE	MOMENT PITCH	COEFFICIENTS ROLL	COEFFICIENTS YAW
0.0	0.002	0.875	0.136	0.005	0.013	0.064
15.0	0.010	0.845	0.133	0.027	0.012	0.075
30.0	0.017	0.775	0.131	0.080	0.011	0.086
45.0	0.029	0.584	0.144	0.050	0.005	0.094
60.0	0.040	0.404	0.156	0.035	0.001	0.098
75.0	0.042	0.203	0.161	0.033	-0.001	0.100
90.0	0.043	0.122	0.164	0.031	-0.003	0.102
105.0	0.041	-0.257	0.167	0.028	-0.004	0.102
120.0	0.039	-0.436	0.167	0.022	-0.004	0.104
135.0	0.033	-0.400	0.165	0.007	-0.003	0.105
150.0	0.026	-0.482	0.168	-0.024	-0.002	0.106
165.0	0.013	-0.513	0.179	-0.008		0.106
180.0	-0.005	-0.521	0.177	-0.001	0.001	0.105

AZIMUTH ANGLE =90.0

ELEVATION ANGLE	FORCE NORMAL	COEFFICIENTS AXIAL	COEFFICIENTS SIDE	MOMENT PITCH	COEFFICIENTS ROLL	COEFFICIENTS YAW
0.0	0.005	-0.047	0.201	0.015	0.012	0.130
15.0	0.001	-0.019	0.185	0.007	0.012	0.130
30.0	-0.002	-0.003	0.175	0.005	0.012	0.129
45.0	-0.003	0.016	0.170	0.002	0.011	0.129
60.0	-0.004	0.026	0.165	0.001	0.008	0.130
75.0	-0.002	0.021	0.160		0.006	0.129
90.0		0.021	0.162		0.004	0.128
105.0	0.002	0.026	0.165		0.006	0.129
120.0	0.003	0.021	0.170	-0.001	0.008	0.130
135.0	0.002	0.021	0.178	-0.003	0.010	0.130
150.0		0.019	0.186	-0.006	0.012	0.129
165.0	-0.003	-0.010	0.194	-0.010	0.012	0.129
180.0	-0.006	-0.040	0.201	-0.015	0.013	0.131

AZIMUTH ANGLE =105.0

ELEVATION ANGLE	FORCE NORMAL	COEFFICIENTS AXIAL	COEFFICIENTS SIDE	MOMENT PITCH	COEFFICIENTS ROLL	COEFFICIENTS YAW
0.0	0.005	-0.521	0.177	0.001	0.001	0.105
15.0	-0.013	-0.511	0.179	0.008		0.106
30.0	-0.026	-0.481	0.168	0.024	-0.002	0.132
45.0	-0.033	-0.401	0.165	-0.007	-0.003	0.105
60.0	-0.039	-0.432	0.167	-0.022	-0.004	0.104
75.0	-0.041	-0.254	0.167	-0.028	-0.004	0.102
90.0	-0.043	0.126	0.164	-0.031	-0.003	0.102
105.0	-0.042	0.203	0.161	-0.033	-0.001	0.100
120.0	-0.040	0.400	0.156	-0.035	0.001	0.098
135.0	-0.029	0.582	0.144	-0.050	0.005	0.094
150.0	-0.017	0.770	0.131	-0.080	0.011	0.086
165.0	-0.010	0.844	0.133	-0.027	0.012	0.075
180.0	-0.002	0.872	0.136	-0.005	0.013	0.064

AZIMUTH ANGLE =120.0

ELEVATION ANGLE	FORCE NORMAL	COEFFICIENTS AXIAL	COEFFICIENTS SIDE	MOMENT PITCH	COEFFICIENTS ROLL	COEFFICIENTS YAW
0.0	0.019	-0.163	0.235	0.002	-0.005	0.145
15.0	-0.032	-0.152	0.228	-0.002	-0.005	0.140
30.0	-0.056	-0.123	0.201	-0.012	-0.001	0.132
45.0	-0.067	-0.533	0.180	-0.025	0.006	0.120
60.0	-0.077	-0.499	0.155	-0.040	0.003	0.102
75.0	-0.084	-0.262	0.150	-0.054	0.002	0.105
90.0	-0.084	0.053	0.150	-0.065	0.002	0.100
105.0	-0.078	0.390	0.142	-0.071	0.001	0.090
120.0	-0.056	0.800	0.120	-0.061	0.003	0.070
135.0	-0.020	1.160	0.050	-0.071	0.013	0.035
150.0	0.008	1.533	-0.030	-0.090	0.022	-0.010
165.0	-0.017	1.670	-0.065	-0.089	0.018	-0.050
180.0	-0.085	1.581	-0.076	-0.130	0.018	-0.075

AZIMUTH ANGLE =135.0

ELEVATION ANGLE	FORCE NORMAL	COEFFICIENTS AXIAL	COEFFICIENTS SIDE	MOMENT PITCH	COEFFICIENTS ROLL	COEFFICIENTS YAW
0.0	0,006	-0.605	0.200	0.008	0.001	0.130
15.0	-0.057	-0.513	0.197	-0.014	0.005	0.128
30.0	-0.095	-0.352	0.191	-0.035	0.005	0.121
45.0	-0.115	-0.201	0.175	-0.072	-0,003	0.109
60.0	-0,0116	-0.556	0,140	-0.083	0.003	0.099
75.0	-0,108	-0,499	0.134	-0.096		0.091
90.0	-0.105	-0.107	0.124	-0.097	-0.001	0.080
105.0	-0,105	0,528	0,090	-0,096		0,060
120.0	-0.053	1.282	0.039	-0.066	0,006	0.029
135.0	-0.013	1,580	-0.035	-0.062	0.004	-0.038
150.0	0,008	1.625	-0.070	-0.070	0.001	-0.082
165.0	0.018	1.600	-0.064	-0,055	0.006	-0,055
180.0	0.021	1.513	-0.058	-0.035	0.018	-0.055

AZIMUTH ANGLE = 150,0

ELEVATION ANGLE	FORCE NORMAL	COEFFICIENTS AXIAL	COEFFICIENTS SIDE	MOMENT PITCH	COEFFICIENTS ROLL	COEFFICIENTS YAW
0,0	0.016	-0.737	0,158	0.019	0.002	0.103
15.0	-0.085	-0.602	0.157	-0.008	0.004	0.102
30.0	-0.118	-0.581	0,153	-0,034	0.006	0.101
45.0	-0.127	-0.722	0.146	-0.076	0.006	0.097
60.0	-0.123	-0.911	0.136	-0.113	0.005	0.089
75.0	-0,112	-0.636	0.119	-0.117	0.004	0.079
90.0	-0.112	-0.105	0.094	-0.120	0.004	0.065
105.0	-0.107	0.722	0.052	-0.112	0,003	0.042
120.0	0.009	1.600	-0.029	-0.010	0.002	-0.019
135,0	0.052	1.786	-0.050	0.034	-0.004	-0.070
150.0	0.049	1,500	-0.043	-0.062		-0.035
165.0	0.032	1.445	-0.042	-0.058	-0.004	-0.031
180.0	0.025	1.572	-0,044	-0.030	-0.013	-0.038

AZIMUTH ANGLE =165.0

ELEVATION ANGLE	FORCE NORMAL	COEFFICIENTS AXIAL	COEFFICIENTS SIDE	MOMENT PITCH	COEFFICIENTS ROLL	COEFFICIENTS YAW
0.0	0.018	-0.949	0.081	0.038	0.007	0.060
15.0	-0.096	-0.873	0.079	-0,005	0.009	0.060
30,0	-0.133	-0.753	0.075	-0.047	0.010	0.059
45.0	-0.150	-0.661	0.070	-0.086	0.011	0.057
60.0	-0.153	-0.764	0.062	-0.111	0.010	0,056
75.0	-0.126	-0.452	0.052	-0.120	0.009	0.054
90.0	-0.122	0.142	0.034	-0.122	0.009	0.047
105.0	-0.108	0.980	0.013	-0.113	0.008	0.037
120.0		1.473	-0.017	-0.011	0.007	0.012
135.0	0,066	1.575	-0.034	0.042	0.005	-0.020
150.0	0.047	1.495	-0.027	-0.047	0.001	-0.025
165.0	0.034	1.480	-0.022	-0.068	-0.003	-0.021
180.0	0.032	1.523	-0.022	-0.068	-0.006	-0.021

AZIMUTH ANGLE = 180.0

ELEVATION ANGLE	FORCE NORMAL	COEFFICIENTS AXIAL	COEFFICIENTS SIDE	MOMENT PITCH	COEFFICIENTS ROLL	COEFFICIENTS YAW
0.0	0.030	-0.961	0.002	-0.022	0.001	0.002
15.0	-0.070	-0.881	0.003	-0.028		0.002
30.0	-0.151	-0.792	0.004	-0.050	-0.001	0.002
45.0	-0.201	-0.533	0.004	-0.112	-0.001	0.001
60.0	-0.216	-0.605		-0.124		0.001
75.0	-0.161	-0.501	-0.004	-0.110	0.001	
90.0	-0.153		-0.007	-0.104	0.001	
105.0	-0.122	0.983	-0.010	-0.069	0.001	
120.0	0.078	1.831	-0.011	0.049	0.002	
135.0	0.110	10600	-0.003	0.042	0.002	-0.001
150.0	0.058	1.462	0.001	-0.020	0.001	-0.001
165.0	0.039	1.500	0.001	-0.032	0.002	-0.002
180.0	0.032	1.521	-0.002	-0.038	-0.002	-0.003